acta physica slovaca vol. 51 No. 2, 69 – 138 April 2001

LATTICE MODELS STUDIED BY NUMERICAL RENORMALIZATION GROUP APPROACHES: REVIEW OF CRITICAL PROPERTIES [1]

A. Gendiar [2]
Institute of Physics, Slovak Academy of Sciences, Dúbravská cesta 9, SK 842 28 Bratislava, Slovakia
and Institute of Electrical Engineering, Slovak Academy of Sciences, Dúbravská cesta 9, SK 842 39 Bratislava, Slovakia

Received 28 February 2001, in final form 15 March 2001, accepted 19 March 2001

This review concerns with numerical studies of density matrix renormalization group (DMRG) technique applied to various two- and three-dimensional classical spin lattice models. The main goal is to introduce DMRG as a powerful method suitable to treat models at the criticality, i. e., to determine critical points, all critical exponents as well as spatially modulated commensurate and incommensurate phases. In particular, a generalization of the DMRG algorithm is proposed and applied to a complete construction of phase diagrams of two-dimensional antiferromagnetic next-nearest-neighbor Ising (ANNNI) model as well as antiferromagnetic triangular nearest-neighbor Ising (ATNNI) model. Both models exhibit incommensurate modulated structures. The nonexistence of the Lifshitz point in the ATNNI model is conjectured. A proposal how to modify the DMRG method for two-dimensional classical models with periodic boundary conditions is given. It is shown that this approach is much more efficient to reveal critical properties of two-dimensional classical models in connection with a finite-size scaling than that starting from the standard DMRG when the open or fixed boundary conditions were imposed. A criterion for an optimum strip width is found. It enables to obtain the critical points as well as all critical exponents with high accuracy. The two-dimensional Ising and Potts models are studied in detail. A commensurate-disordered (C-D) phase transition in the ATNNI model has not been studied yet. Therefore, the C-D phase transition is studied in detail applying the modified DMRG algorithm with periodic boundary conditions and a finite-size scaling. Critical points (T_c, H_c) as well as all critical exponents are calculated on the C-D transition line. The Tensor Product Variational Approach (TPVA) algorithm is employed to treat the first order phase transition of the three-dimensional q=3 and q=4 Potts models by independent observations of the free energy, internal energy and magnetization for two different boundary conditions.

PACS: 05.50.+q, 64.70.Rh, 05.70.Fh, 02.70.-c

[1] Review article is based on author's Ph.D. thesis.
[2] E-mail address: fyziagen@savba.sk

Contents

1 Introduction

1.1 Preface

In recent years with increasing progress of computational techniques, the analysis of statistical mechanical systems as well as of their quantum mechanical analogs has been focused on the investigation their properties, especially, at the criticality. Since only very few models are exactly solvable, these investigations have become important. Knowledge of their critical properties helps us sort these models to various universality classes.

For a two-dimensional classical statistical system, the transfer matrix plays an important role. Their largest eigenvalues and corresponding eigenvectors are used to extract thermodynamic properties of the system. In order to follow the procedure analytically, it is restricted by the constraint of the integrability satisfying the Yang-Baxter relation [1].

The first paper after Ising who using the transfer matrices was written in 1941 by Kramers and Wannier who dealt with the Ising model on the square lattice [2]. Their idea was based on the variational approximation of the largest eigenvalue of the transfer matrix. With this approach they exceeded the accuracy of mean-field theories as well as of the Bethe approximation. However, consequent considerations how to extend of their method were not performed.

In 1968 Baxter introduced a general formulation of the transfer matrix variational method [3, 4]. He suggested variational trial function in a matrix product form. Moreover, he has shown that not only the transfer matrices were suitable to consider but row-column symmetries might also have been taken into account. He invented a corner transfer matrix and created an iterative method for its solution [5, 6] which could be reformulated by the self-consistent truncated equation of the corner transfer matrix. That is why his iterative method is closely related to the real space renormalization group [7–10].

The numerical real space renormalization group developed by Wilson in 1975 [8] caused considerable interest in its applying to a variety of problems. It was believed that this technique could solve much more models than the only one-dimensional quantum Kondo problem being treated by him in that time. Unfortunately, that approach proved to be rather unreliable in comparison with the developed Monte Carlo method. Therefore, the real space renormalization group has been used only occasionally.

A significant progress in computational condensed-matter physics began in 1992 when White introduced the density matrix renormalization group (DMRG) method [11, 12] based on the real space renormalization group for one-dimensional quantum models. Its remarkable accuracy can be seen, for example, in the spin-1 Heisenberg chain: for a system of hundreds of sites. A relative precision of 10^{-10} for the ground state energy can be achieved.

Since then it has been applied to a great variety of the systems such as Haldane systems [13–15], spin ladders [16], highly correlated electron systems [17], superconducting materials [18], fermionic [19–21] and bosonic [22, 23] systems, analyzing of impurity systems [24], random systems [25, 26], Bethe lattice systems [27], momentum space [28], etc. Nowadays, DMRG has become one of the standard numerical methods for the one-dimensional quantum systems.

DMRG is also applicable to two-dimensional classical systems because the path integral representation [29] of the one-dimensional quantum systems corresponds to two-dimensional classical system. In particular, an one-dimensional quantum system at finite temperature can be mapped to a two-dimensional classical system via the Trotter-Suzuki decomposition [30, 31]. Such modification to the two-dimensional classical system was performed by Nishino [32] in 1995 where he used the transfer matrix formulations.

In spite of great progress in DMRG, let us explain and clarify the reason why DMRG is so efficient. The explanation came from Nishino and Okunishi who have shown a relationship between DMRG and the Baxter's iterative method of the corner transfer matrix. The fourth power of the corner transfer matrix is equivalent to the density matrix used in DMRG. They have shown that both methods had yielded the same results in the thermodynamic limit and constructed a new efficient algorithm – the corner transfer matrix renormalization group (CTMRG) method [33–35].

In 2000, a brand-new algorithm, the tensor product variational approach (TPVA), has been developed for the three-dimensional classical models [36]. Further improvements in obtaining the critical point in the 3D Ising model of the vertex type has also been gained [37] where additional degrees of freedom has been considered.

This review is aimed to elucidate principles of the DMRG for the two- and three-dimensional classical lattice models. It also gives a view on further generalizations and points out the efficiency, precision and speed of DMRG. It is beyond the scope of this review to compare DMRG with various other techniques, such as Monte Carlo simulations, series expansions etc.

Sec. 1 is devoted to a brief introduction to the critical phenomena in statistical mechanics. In Sec. 2, commensurately and incommensurately modulated structures are discussed in this article. In Sec. 3, a short review of theoretical background of the numerical renormalization group approaches is discussed, in particular, the DMRG as well as the CTMRG methods for two-dimensional classical systems are explained and the tensor product variational approach (TPVA) [36] as a self-consistent method for treating three-dimensional classical systems is also briefly presented. The finite-size scaling based on the phenomenological renormalization analysis is presented in Sec. 4. Sec. 5 contains modifications and applications of the above mentioned methods to various two- and three-dimensional lattice models. They represent the main contribution for studies of classical spin lattice systems in the thermal equilibrium and presented results were published by the author last year. In Sec. 6, the results are summarized and discussed.

1.2 Phase transitions and critical points

Statistical mechanics is concerned with systems consisting of a large amount of individual components (usually atoms or molecules) and describes the average properties of a mechanical system, e. g., water in a kettle, atoms in a bar magnet and the like. The observer can obtain information by specifying or measuring the average properties of the system, such as its temperature, density or magnetization. The aim is to predict the relations between the observable macroscopic properties of the system knowing only the microscopic forces between the elements.

Let us suppose we know the interaction forces acting among water molecules. Then,

we should be able to predict the density ρ of water at a given temperature T and pressure p. Moreover, we should predict the dramatical decrease by a factor of about 10^3 of the density ρ as the temperature T is increased from 99°C to 101°C at the pressure p=101.325 kPa when the water changes from liquid to vapor. This behavior is known as a *phase transition.*

As another example, let us consider an iron bar in a strong magnetic field H. The iron bar becomes completely magnetized. The measured magnetization M at a room temperature is +1 (in appropriate units). By decreasing the magnetic field H to zero, the magnetization M is decreased too, but to a nonzero positive value of a *spontaneous magnetization* $M_0 > 0$ [3]. This behavior is not observed above the critical temperature $T_{\rm C}^{\rm Fe} \approx 770.8$°C. The *critical point* $T_{\rm C}$ is also known as the Curie point.

There are two important items in the above-mentioned examples: the *phase transition* and the *critical point.* In both cases, the order parameter can be introduced. The order parameter separates the ordered (nonzero value of the order parameter) and disordered (the order parameter is zero) phases.

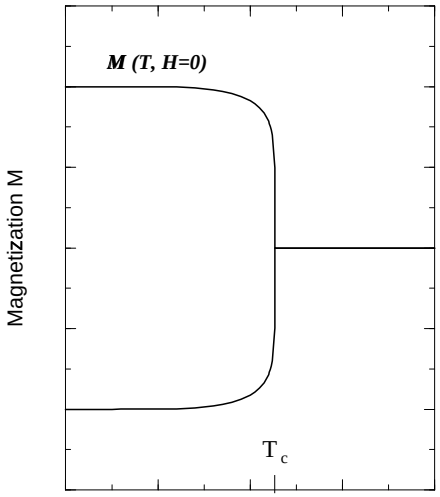

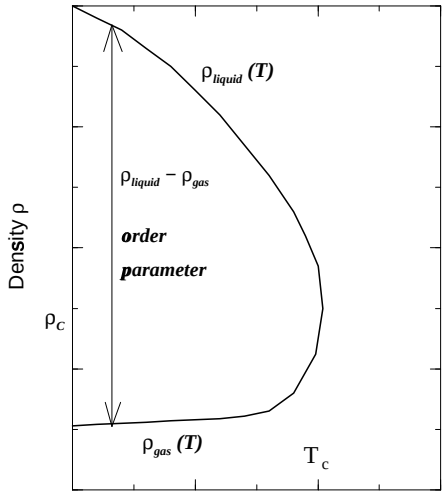

Fig. 1. Magnetization M versus temperature T as the order parameters for the Ising model.
Fig. 2. Density ρ as a function of T for the water (in appropriate units).

In Fig. 1 an example of the magnetization as the order parameter for the Ising model [4] is shown. The liquid phase and the steam phase of water are described by the order parameter defined by the subtraction $(\rho_{\rm liquid}(T) - \rho_{\rm gas}(T))$ as depicted in Fig. 2. In the case of the bar magnet, the ordered ferromagnetic phase ($T < T_{\rm C}$) and the disordered phase

[3] All the review is written using these special units for the case of simplicity

[4] This dependence of the magnetization M on the temperature T for the Ising model comes from data obtained by DMRG.

($T > T_C$) are characterized by the nonzero and zero total spontaneous magnetization M_0, respectively.

1.3 Thermodynamic functions and the Ising model

In 1902 John Willard Gibbs defined the partition function as the function of the temperature T and the external ordering (magnetic) field H,

$$\mathcal{Z}(T,H) = \sum_s \exp\left(-\frac{E(s)}{k_B T}\right), \tag{1}$$

summed over all allowed states s for given Hamiltonian $E(s)$ at temperature T (k_B being the Boltzmann constant). All thermodynamic functions can be derived from the partition function $\mathcal{Z}(T,H)$. The free energy F is proportional to the logarithm of the partition function, in particular,

$$F(T,H) = -k_B T \ln \mathcal{Z}(T,H). \tag{2}$$

For magnetic systems (using the first thermodynamic low) we can write an infinitesimal change of the internal energy U

$$\mathrm{d}U = T\mathrm{d}S - M\mathrm{d}H. \tag{3}$$

The internal energy U, entropy S, and magnetization M can be derived form the free energy F via the following expressions

$$U = -k_B T^2 \frac{\partial}{\partial T} \ln \mathcal{Z} = -T^2 \frac{\partial}{\partial T}\left(\frac{F}{T}\right), \tag{4}$$

$$S = -\left(\frac{\partial F}{\partial T}\right)_H, \tag{5}$$

$$M = -\left(\frac{\partial F}{\partial H}\right)_T. \tag{6}$$

Calculating the second derivatives of the free energy F one can obtain specific heats C and isothermal susceptibility χ

$$C_H = \left(\frac{\partial U}{\partial T}\right)_H, \tag{7}$$

$$C_{H,M} = T\left(\frac{\partial S}{\partial T}\right)_{H,M}, \tag{8}$$

$$\chi = \left(\frac{\partial M}{\partial H}\right)_T. \tag{9}$$

The probability $P(s)$ of the system in a state s is given as

$$P(s) = \frac{\exp\left(-\frac{E(s)}{k_B T}\right)}{\sum\limits_s \exp\left(-\frac{E(s)}{k_B T}\right)}. \tag{10}$$

Thus, any observable property X of the system, such as the total energy or the total magnetization, having a value $X(s)$ in a state s is observed as the average thermodynamic value through the probability $P(s)$ in Eq. (10) as

$$\langle X \rangle = \frac{\sum\limits_{s} X(s) \exp\left(-\frac{E(s)}{k_B T}\right)}{\sum\limits_{s} \exp\left(-\frac{E(s)}{k_B T}\right)}. \tag{11}$$

The basic problem of equilibrium statistical mechanics is to calculate the partition function $\mathcal{Z}$ as the sum over all states in Eq. (1) (for continuous systems this sum becomes an integral and a trace for quantum mechanical ones). This gives the partition function $\mathcal{Z}$ and the free energy F as functions of temperature T and of any other variables that may occur in the Hamiltonian $E(s)$, such as a magnetic field H.

Unfortunately, for any realistic interacting system of macroscopic size, the evaluation of the partition function becomes hopelessly difficult. In order to overcome the difficulty, we are forced to choose one or both of the following:

(1) To replace the real system by some simple idealization, i. e., by a *model*. In the mathematical language, it requires the specification of the states s and the Hamiltonian function $E(s)$. This approach leads to exactly solvable models and only few models have been analytically solved so far.

(2) To propose numerical or analytical approximation schemes in order to evaluate the partition function $\mathcal{Z}$. Let us briefly discuss several kinds of such schemes.
- Cell or cluster approximations. Behavior of the whole system is extrapolated from that of very few components inside some 'cell' (approximation being made for the interaction of the cell with the rest of the system. The examples involve the mean-field [39, 40], quasi-chemical [41] and the Kikuchi [42] approximations. They are fairly simple to solve and predict the correct qualitative behavior and yield reasonably accurate results except near the critical point.
- Approximate integral equations for the correlation functions for the hyper-netted chain [43] and the Percus-Yevick [44, 45] equations. These give fairly good numerical values for the thermodynamic properties of simple fluids.
- Computer calculations on systems large on a microscopic scale (but not yet of macroscopic size), such as Monte Carlo simulations. These evaluate the partition function $\mathcal{Z}$ by statistically sampling the terms on the right hand side of the Eq. (1).
- Series expansions in powers of some approximate variable, such as the inverse temperature or the density. For the three-dimensional Ising model the expansions have been obtained up to 40 terms [46, 47].
- Renormalization group approach based on the ideas of Kadanoff [7] and Willson [48]. In this method, the sum over states in Eq. (1) is evaluated in successive stages, a renormalized Hamiltonian function $E(s)$ being defined at each stage. This defines a mapping in Hamiltonian space. The thermodynamic functions have branch-point singularities such as the magnetization at T_{C} and that the exponents of the singularities should normally be universal [49, 50].

• Kramers-Wannier approximation [2] uses the transfer matrix technique for the two-dimensional Ising model and is of mean-field-like behavior.
• Cluster transfer matrix method [51] was proposed as an iterative algorithm using overlapped transfer matrix clusters to treat two- and three- dimensional models with short range interactions.
• Baxter's transfer matrix variational method [33–35] as well as another Baxter's iterative method for the corner transfer matrices [5, 6].
• The density matrix renormalization group (DMRG) analysis [10, 11, 12] for one-dimensional quantum chains which is very accurate and fast. The density matrix renormalization is introduced to describe the ground state (as well as several excited states) of the system. The application to the two-dimensional classical models was proposed by Nishino [32] and modification for the corner transfer matrices led to the corner transfer matrix renormalization group (CTMRG) [33]-[35].
• Other modifications based on DMRG are still in progress. Let us mention the most appropriate candidates: the tensor product variational method (TPVA) for treating three-dimensional classical models [36, 37, 52], the puncture renormalization group [53] for 1D, 2D, and 3D quantum one-body problems. The vertical density matrix algorithm for 2D quantum transverse field Ising model as 3D classical Ising model has been recently proposed [54] or the 2D vertex model studied by nonsymmetric CTMRG [55]

The **Ising model** [38] is the simplest idealization of the system which is exactly solvable in one and two dimensions (in 2D only for the case of H=0). This basic lattice model can be thought of as a model of a magnet. Let us regard the magnet made up of molecules which are constrained to lie on the sites of a regular lattice. Suppose there are N such sites labelled $i=1,2,\ldots,N$.

Now let us consider each molecule as a microscopic magnet, which either points along some preferred axis, or in exactly opposite direction. Thus each molecule i has two possible configurations, which can be labelled by a spin variable σ_i with values $+1$ (parallel to axis) or -1 (antiparallel to axis). The spin is said to be *up* when σ_i has value $+1$ or *down* when it has value -1. Often these values are written more briefly as $+$ and $-$. Let $\sigma=\{\sigma_1,\sigma_2,\ldots,\sigma_N\}$ denote the set of of N spins. Then there are 2^N values of σ, and each such value specifies a state of the system [5].

In general, the Hamiltonian is a function $E(\sigma_1,\sigma_2,\ldots,\sigma_N)$ of N spins and is made up of two parts

$$E(\sigma)=E_0(\sigma)+E_1(\sigma), \tag{12}$$

where $E_0(\sigma)$ is the contribution of the intermolecular forces inside the magnet and $E_1(\sigma)$ is the contribution from the interactions between the spins and an external magnetic field H.

In a physical system, the interactions are expected to be invariant under time reversal which means that the Hamiltonian $E(\sigma)$ is unchanged by reversing all fields and magne-

[5] For other models, such as the q-state Potts models, the σ is q-state variable and, consequently, the system contains q^N values.

tizations, i. e., by negating H and $\sigma_1, \sigma_2, \ldots, \sigma_N$. From that it follows that $E_0(\sigma)$ must be an even function of σ, in particular

$$E_0(\sigma_1, \sigma_2, \cdots, \sigma_N) = E_0(-\sigma_1, -\sigma_2, \cdots, -\sigma_N). \tag{13}$$

These results define quite general Ising model, special cases of which have already been solved. From a physicist's point of view, it is highly simplified, the obvious objection is that the magnetic moment of a molecule is a vector pointing to any direction, not just up or down. One can consider this property and obtain the classical Heisenberg model [56] but this model has not been solved yet even in two dimensions.

However, there are crystals with highly anisotropic interactions such that the molecular magnets effectively point up or down, notably $FeCl_2$ [57] and $FeCO_3$ [58]. The three-dimensional Ising should give a good description of these, in fact the universality implies that it should give exactly the correct values of critical exponents which will be discussed later.

The first term $E_0(\sigma)$ in Eq. (12) has (in this case) the form of the Ising model

$$E_0(\sigma) = -J \sum_{(i,j)} \sigma_i \sigma_j, \tag{14}$$

where we sum only the nearest pairs of sites on the lattice. The parameter J represents the interaction energy between the nearest neighbors which remains constant in the Ising model. The ferromagnetic and antiferromagnetic models are then defined by $J<0$ and $J>0$, respectively [6].

The next term $E_1(\sigma)$ describes the interaction of the external field H with all spins as follows

$$E_1(\sigma) = -H \sum_i \sigma_i. \tag{15}$$

The partition function $\mathcal{Z}$ of the Ising model on N lattice sites is given by

$$\mathcal{Z}_N = \sum_\sigma \exp\left[\frac{J}{k_B T} \sum_{(i,j)} \sigma_i \sigma_j + \frac{H}{k_B T} \sum_i \sigma_i\right]. \tag{16}$$

Physically, we expect the free energy of a large system to be proportional to the size of the system, i. e., we expect that the thermodynamic limit

$$f(H,T) = -k_B T \lim_{N\to\infty} \frac{1}{N} \ln \mathcal{Z}_N(H,T) \tag{17}$$

exists, In such a case f is the free energy per site.

[6] The ferromagnetic model is characteristic by all spins pointing to the same direction for the model in the ground state (at low temperatures) and the antiferromagnetic ones by alternating spins.

1.4 Magnetization and correlation functions

Magnetization M is the average of the magnetic moment per site, i. e., using Eq. (11),

$$M(H,T) = \frac{1}{N} < \sigma_1 + \cdots + \sigma_N > \tag{18}$$

$$= \frac{1}{N}\frac{1}{\mathcal{Z}_N}\sum_{\sigma}(\sigma_1 + \cdots + \sigma_N) \quad \exp\left[-\tfrac{1}{k_BT}\left(-J\sum_{(i,j)}\sigma_i\sigma_j - H\sum_i \sigma_i\right)\right]. \tag{19}$$

Differentiating the partition function in Eq. (16) with respect to H and using Eq. (17) one obtains that in the thermodynamic limit ($N \to \infty$)

$$M(H,T) = -\frac{\partial}{\partial H} f(H,T). \tag{20}$$

Since the summand in Eq. (16) is unchanged by negating H and σ, the partition function $\mathcal{Z}_N$ as well as the free energy f are even functions of H, so M is an odd function, i. e.,

$$M(-H,T) = -M(H,T). \tag{21}$$

Normalization introduced in Eq. (18) defines magnetization which is in the interval

$$-1 \le M(H,T) \le +1. \tag{22}$$

Differentiation Eq. (19) with respect to H again and using Eq. (11) yields the susceptibility which is defined as

$$\chi = \frac{\partial M}{\partial H} = \frac{1}{Nk_BT}\{\langle \mathcal{M}^2\rangle - \langle \mathcal{M}\rangle^2\}, \tag{23}$$

where

$$\mathcal{M} = \sum_i \sigma_i. \tag{24}$$

Using the fact that the average of a constant is the same constant, Eq. (23) can be written

$$\chi = \frac{1}{Nk_BT}\langle(\mathcal{M} - \langle \mathcal{M}\rangle^2)^2\rangle. \tag{25}$$

Thus χ is the average of a nonnegative quantity, in particular

$$\chi = \frac{\partial M}{\partial H} \ge 0. \tag{26}$$

The correlation between spins σ_i and σ_j is

$$g_{ij} = < \sigma_i\sigma_j > - < \sigma_i >< \sigma_j > . \tag{27}$$

Assuming that $E_0(\sigma)$ is translationally invariant, the average $< \sigma_i >$ is the same for all sites i and therefore

$$< \sigma_i > = < \sigma_j > = M(H,T). \tag{28}$$

Moreover, the correlation function g_{ij} depends only on the vector distance $\vec{r}_{ij}$ between the sites i and j, i. e.,

$$g_{ij} = g(\vec{r}_{ij}). \tag{29}$$

where $g(\vec{r})$ is the correlation function. Away from the T_{C}, the correlation function $g(\vec{r})$ is expected to decay exponentially to zero as $\vec{r}$ becomes large. More precisely speaking, if $\vec{k}$ is some fixed unit vector, we expect that

$$g(x\vec{k}) \sim x^{-\tau} \exp\left(-\frac{x}{\xi}\right) \qquad \text{as } x \to \infty, \tag{30}$$

where τ is some number and ξ is the correlation length in the direction $\vec{k}$. The correlation length is a function of H and T, and is expected to become infinite at T_{C}, i. e.,

$$\xi(H, T_C) \to \infty. \tag{31}$$

1.5 Critical exponents and universality

Critical exponents play an important role in the theory of phase transitions as they describe the divergence or singular behavior of some thermodynamic functions in the very close vicinity of the critical point [59]. When considering the critical behavior it is convenient to replace T by

$$t = \frac{T - T_{\mathrm{C}}}{T_{\mathrm{C}}}. \tag{32}$$

In general, critical exponent λ associated with thermodynamic function $Y(t)$ is written as

$$\lambda = \lim_{t \to 0} \frac{\ln |Y(t)|}{\ln |t|} \tag{33}$$

or more frequently used in the form

$$Y(t) \sim |t|^{\lambda}. \tag{34}$$

Let us briefly introduce definitions of all critical exponents.

- Exponent α: the specific heat C_H at $H = 0$ diverges for $T \to T_{\mathrm{C}}$ as

$$C_H \sim |t|^{-\alpha}. \tag{35}$$

- Exponent β: for infinitesimally small external magnetic field H, magnetization M (the order parameter) decays for $0 \leq T \leq T_{\mathrm{C}}$ (see Fig. 1). At T very close to T_{C} the magnetization behaves as

$$M \sim (-t)^{\beta}. \tag{36}$$

- Exponent γ: the magnetic (isothermal) susceptibility $\chi = \left(\frac{\partial M}{\partial H}\right)_T$ at zero external magnetic field diverges as a function of temperature according to

$$\chi \sim |t|^{-\gamma}. \tag{37}$$

- Exponent δ: at criticality, magnetization M as a function depending on the external magnetic field H is not a smooth function of H and it reads

$$M \sim H^{1/\delta}, \qquad \text{or} \qquad H \sim |M|^{\delta}\text{sign}(M). \tag{38}$$

- Exponent ν: the correlation function ξ (for $H=0$) diverges at $T = T_{\rm C}$

$$\xi \sim |t|^{-\nu}. \tag{39}$$

- Exponent η: the correlation function $g(\vec{r})$ still exists at the critical point $T_{\rm C}$ but instead of decaying exponentially it decays according to the power low

$$g(\vec{r}) \sim \frac{1}{r^{d-2-\eta}}\ , \tag{40}$$

  where the dimension d has been introduced.

- Exponent μ: as T approaches $T_{\rm C}$ ($T < T_{\rm C}$) the interfacial tension s goes to zero and it is expected that

$$s(T) \sim (-t)^{\mu}. \tag{41}$$

Whereas the critical point $T_{\rm C}$ is sensitive for details of intermolecular interactions, the critical exponents remains universal as they depend only on fundamental parameters. For models with short-range interactions, these parameters are of the dimension d of the system and symmetry of the order parameter. Therefore, it is better to study the simple Ising model than any complicated Hamiltonian of fluid. Sometimes the scaling is known as the 'two exponent' scaling, since if two independent exponents (such as β and ν) are given, all other exponents can be obtained from the following scaling equations

$$\alpha + 2\beta + \gamma = 2 \tag{42}$$
$$\gamma = \beta(\delta - 1) \tag{43}$$
$$(2 - \eta)\nu = \gamma \tag{44}$$
$$\mu + \nu = 2 - \alpha \tag{45}$$
$$d\nu = 2 - \alpha. \tag{46}$$

1.6 Mean-field theory for the Ising model

The mean-field model describes a statistical mechanical system in which each component interacts with the average over all components (on the contrary to the standard Ising model studied in Sec. 1.6) and with the external magnetic field H. Thus the mean-field Hamiltonian is

$$E(\sigma) = -\frac{qJ}{N-1}\sum_{(i,j)}\sigma_i\sigma_j - H\sum_{i=1}^{N}\sigma_i, \tag{47}$$

where the first sum is taken over all $\frac{N(N-1)}{2}$ distinct pairs (i,j) and q denotes the number of neighboring sites. There is no dimension in the mean-field model, in particular, there is no difference between the 3D Ising mean-field model on the cubic lattice and the 2D Ising mean-field model on the triangular lattice as they both share the same value $q=6$. The mean-field model is therefore considered to be an infinite dimensional model since each spin interacts equally with every other [7]. Thus it also has the unphysical property that the interaction coupling depends on the number of particles. Nevertheless, it does give moderately sensible thermodynamic properties.

Solving the mean-field model [1] one obtains the formula

$$H = -qJM + k_BT\,\mathrm{artanh}(M), \tag{48}$$

being defined for the magnetization $M \in (-1,+1)$ and the magnetic field $H \in (-\infty,\infty)$ as is shown in Fig. 3. The mean-field model yields a nonzero critical point $T_C > 0$. Let

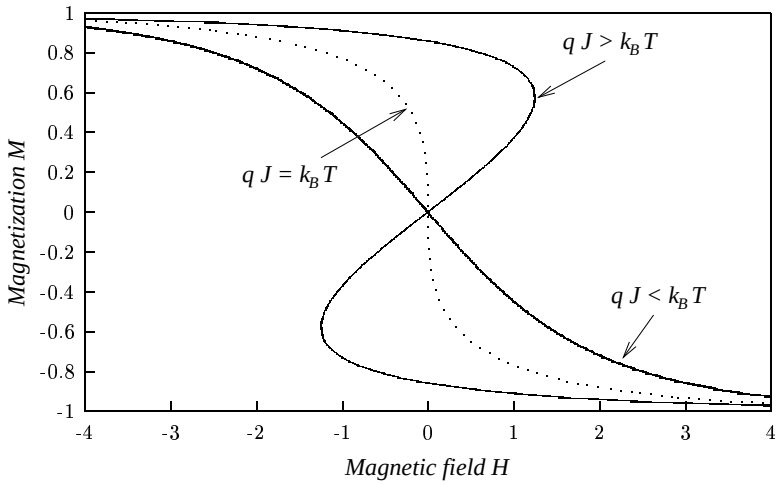

Fig. 3. Graphical representation of the equation $H = -qJM + k_BT\,\mathrm{arctanh}(M)$ for a reversed problem, i. e., M as a function of H.

us discuss below three different conditions:

[7] Most of the numerical algorithms is based on the mean-field approximations that come from the factorization of the Hamiltonian into small blocks (clusters) and each cluster itself carries information on the neighboring clusters.

1. For $qJ < k_BT$ the resulting graph describes the high-temperature phase with no spontaneous magnetization., i. e., the spontaneous magnetization $M = 0$ for the zero magnetic field H.

2. For $qJ > k_BT$ the $M(H)$ curve in Fig. 3 intersects the vertical axis $H = 0$ three times. However, this result is unphysical and the spurious solution must be rejected and replaced by the curve with the discontinuity of the second order at $H = 0$ so that the the following limits are satisfied

$$\lim_{H \to 0^+} M(H) = +M_0, \tag{49}$$

$$\lim_{H \to 0^-} M(H) = -M_0. \tag{50}$$

   To be more precise, the part of the $M(H)$ curve lying in the interval $\langle -M_0, M_0 \rangle$ must be replaced by a straight line (along the vertical axis $H = 0$) connecting the magnetizations $-M_0$ and $+M_0$.

3. For $qJ = k_BT$ which is equivalent to $T_C = \frac{qJ}{k_B}$, the mean-field model exhibits a phase transition between the ordered and the disordered phases. The ordered phase at the magnetic field $H = 0$ and temperature $T = 0$ consists of spins all pointing either up ($M = +1$) or down ($M = -1$) whereas the disordered one at $H = 0$ and temperature $T > T_C$ yields zero magnetization, i. e., the spins are arbitrarily pointing up and down and the average magnetization tends to zero for $N \to \infty$. The spontaneous magnetization M in the ordered phase approaches zero as $T \to T_C$ at $H = 0$, see Fig. 1. In the presence of a small nonzero field H, the total magnetization M is nonzero even in the disordered phase.

Critical exponents of the mean-field model [1] are

$$\alpha = 0, \qquad \beta = \frac{1}{2}, \qquad \gamma = 1, \qquad \delta = 3. \tag{51}$$

Since each spin interacts equally with every other, correlations are not distance-dependent, nor can the model have two physically separated coexisting phases. Thus the exponents ν, η, and μ are not defined within this model.

2 Incommensurability

2.1 Introduction

Periodically modulated structures are well-known in condensed-matter physics and may be observed from the basic (substrate) lattice as another lattice with modulation, a periodic lattice distortion, a helical or sinusoidal magnetic structure, or as a charge density wave in one, two, or three dimensions. Periods of modulated structures can be commensurate or incommensurate with the basic lattice as is shown in Fig. 4. Here, the

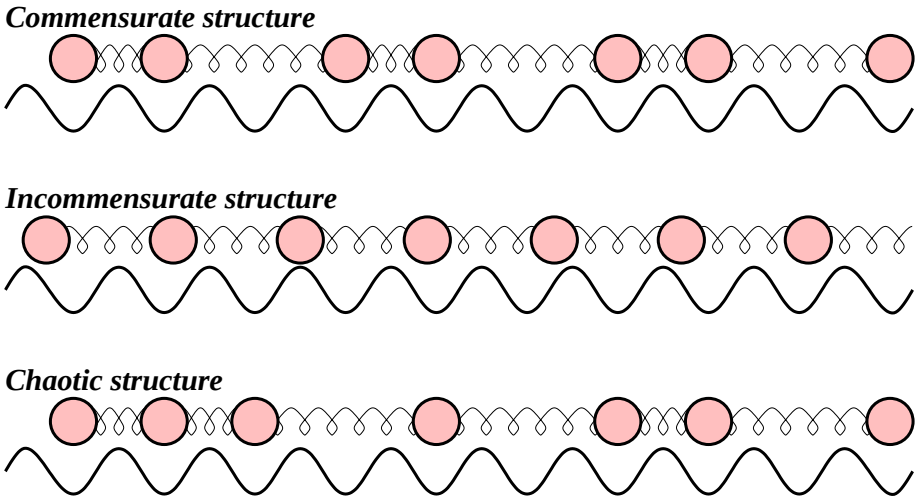

Fig. 4. The commensurate, incommensurate, and chaotic structures on an one-dimensional model. The springs represent elastic interaction between atoms of gas that are adsorbed on a lattice substrate depicted by the periodic potential as the wavy line.

commensurate structure is a simple rational fraction with the period $\frac{3}{2}a$ (a being the period of the periodic potential of a lattice) whereas the period of the incommensurate one cannot be expressed by a rational number. Yet another structure may appear, a chaotic structure where the atoms are randomly positioned.

Physically, the atoms are usually the rare-gas atoms adsorbed on a substrate so that at given temperature, pressure etc., the atoms tend to move towards the periodic potential minima in order to reach the most appropriate energy. The chaotic state (phase) is the most probable when the potential is very strong compared with the elastic forces among atoms. The commensurate phase locks the atoms in the potential minima yielding a periodic structure. So in general, the periodic potential will tend to lock the system into a commensurate configuration. On the other hand, the incommensurate phase will not be locked and the substrate lattice can be shifted without climbing a potential barrier. So if the atoms were charged, the commensurate phase would be insulating and the incommensurate phase would be conducting phase [61, 62].

The nature of the structure of the incommensurate phase is quite different in two and three dimensions. In 3D the incommensurate phase seems to consist of an infinity

of high-order locked commensurate phases, which may or may not be separated by an infinity of truly incommensurate phases. In 2D the incommensurate phase (at nonzero temperature) is known as a floating phase without complete long-range order and does not lock-in at high-order commensurate phases.

In Sections 5.1 and 5.2, the commensurate and incommensurate phases are studied for two-dimensional lattice models. A spin magnetization per site will be observed therein as the modulated structures mentioned above. The magnetization profiles will be clearly shown.

2.2 The ANNNI model

There is a very simple magnetic model which exhibits phase diagrams with commensurate, incommensurate, floating, and chaotic phases: the anisotropic next-nearest-neighbor Ising (ANNNI) model. There are competing the nearest- and next-nearest-neighbor interactions. Although the model is too simple to mimic real magnetic systems, it does reproduce most of the features encountered in experiments [63]. The Hamiltonian of the ANNNI model [8] defined on the square lattice is given by

$$\mathcal{H} = \sum_{i,j} J_1 \left(\sigma_{i,j}\sigma_{i+1,j} + \sigma_{i,j}\sigma_{i,j+1}\right) + \sum_{i,j} J_2 \sigma_{i,j}\sigma_{i+2,j} \tag{52}$$

where the two-state spins $\sigma_{i,j} = \pm 1$ sitting at the lattice positions (i, j) interact through a ferromagnetic nearest-neighbor interaction J_1 and an antiferromagnetic next-nearest-neighbor interaction J_2 only in one particular direction. In 3D there is the J_1 interaction acting on all three directions whereas the J_2 interaction acts on one fixed direction only.

The competition between J_1 and J_2 stabilizes the various periodic phases. The presence of the modulated structure can be observed by, e. g., magnetization per site. The resulting graphs exhibiting the incommensurate phase will be presented later. [9] Domain walls (or *solitons*, in the language of the sine-Gordon equation) observed in these periodic magnetization structures are characterized by changes of the magnetizations from their maximal to minimal values and vice versa.

2.3 The commensurate-incommensurate transition

The possibility of floating phases in 2D was pointed out by Wegner [64] for XY magnets and by Jancovici [65] for harmonic crystals. The correlation functions $\langle\sigma(0)\sigma(r)\rangle$ as the *order parameter* take the following forms in various commensurate and incommensurate phases (q being the wave vector of the phase) at long distances

$$\text{incommensurate}: \quad \langle\sigma(0)\sigma(r)\rangle \sim \cos(q\cdot r + \varphi), \tag{53}$$

$$\text{floating incommensurate}: \quad \langle\sigma(0)\sigma(r)\rangle \sim r^{-\eta}\cos(q\cdot r + \varphi), \tag{54}$$

$$\text{commensurate}: \quad \langle\sigma(0)\sigma(r)\rangle \sim \cos(q_0\cdot r), \tag{55}$$

[8] The 2D ANNNI model in the triangular lattice is also defined in Sec. 5.1.

[9] The incommensurate phases of spin lattice models are depicted in Figs. 21, 22, and 24 for different interaction constants J_1, J_2, and temperature T.

q_0 being the commensurate (locked) phase wave vector. The floating phase (with incommensurate or accidently unlocked commensurate wave vector and corresponding power law decay) is believed to exist only in two dimensions. The other phases may exists also in three dimensions. The commensurate-incommensurate transition is subjected to an instability with respect to the presence of domain walls. Pokrovsky and Talapov [66] found the power law correlation function characteristic for the floating phase. In an experiment on Xe absorbed on Cu(110), Jaubert et al. [67] found the critical exponent $\beta = \frac{1}{2}$ which is in agreement with the Pokrovsky-Talapov theory. The critical exponent β corresponds to a soliton density $\bar{q}$ (or also equivalently, the domain wall density). Inside the incommensurate phase, near the commensurate phase, the soliton density is found to be low.

The two-dimensional generalization of the Frank and Van der Merwe theory [68] leads to the Pokrovsky-Talapov Hamiltonian

$$\mathcal{H} = \int \mathrm{d}x\mathrm{d}y \left[\frac{1}{2}\gamma \left(\frac{\partial \varphi}{\partial y} \right)^2 + \frac{1}{2} \left(\frac{\partial \varphi}{\partial x} - \delta \right)^2 + V \cos(p\varphi) \right] \tag{56}$$

where the phase φ is a shift of atoms relative to the potential minima, $\delta = (2\pi/b)(a-b)$ is the relative *natural misfit* between the two lattices with lattice spacings a and b. The periodic potential is denoted as V and $p > 1$ describes a transition to a commensurate phase of order p.

Using the transfer matrix method it can be shown that the calculation of the free energy of the two-dimensional model amounts to the calculation of the ground-state energy of the 1D quantum Hamiltonian $\hat{H}$ [63]. Performing the first linearized term of the free energy near $\delta = \delta_\mathrm{c}$, we can obtain the domain wall density critical exponent β

$$\bar{q} \sim (\delta_\mathrm{c} - \delta)^\beta \qquad \beta = \frac{1}{2} \tag{57}$$

which will be in agreement with the results reported in Sec. 5.1.4.

3 Numerical renormalization group analysis

3.1 DMRG method for 2D classical models

The DMRG method has been developed and applied to various one-dimensional quantum systems. It is also possible to treat two-dimensional classical systems since d-dimensional quantum systems are closely related to the classical ones in $d+1$ dimensions through the Suzuki-Trotter decomposition [30–32].

In 1995 Nishino has shown, as the first one, how to formulate DMRG for the two-dimensional spin models using transfer matrix formulations for the Ising models. Then, the 2D classical lattice models are numerically solvable by DMRG when introducing a transfer matrix T.

As it is well-known, the partition function $\mathcal{Z}$ of a particular model can be evaluated by multiplication of the transfer matrices summed over all spin sites. In order to obtain thermodynamic properties of an infinitely large two-dimensional lattice, the partition function is expressed

$$\mathcal{Z} = \lim_{M,N\to\infty} \text{Trace } T_N^M(\sigma_1 \cdots \sigma_N | \sigma'_1 \cdots \sigma'_N) \tag{58}$$

where the power M denotes the number of lattice rows and N is the number of sites in each lattice row.

Let us assume that there is a gap between the largest and the second largest eigenvalue of the transfer matrix T_N^M. Then the free energy per site of the infinite system is given as $f = -k_B T \ln \lambda_{\max}$, where $\lambda_{\max}$ is the largest eigenvalue of the transfer matrix T. Therefore, if we were able to calculate the largest eigenvalue of the transfer matrix, we could solve the particular model. Unfortunately, this is not possible for many models. For example, some of those that are analytically solvable are shown in [1].

At present, the computational technique is in great progress, but it is still very difficult to calculate (if at all) the the largest eigenvalue from the transfer matrix of the 2D Ising model for $N > 30$. The computational time is enormous. The DMRG method can be of use for such problems. DMRG is based on the Wilson renormalization group analysis [8] which is employed to approximate transfer matrices of large sizes so that the highly excited states are integrated out (thrown away) while the transfer matrix dimension remains fixed. The largest eigenvalues of the obtained renormalized transfer matrices can be easily evaluated (even several successive excited states). However, the approximation decreases with increasing of the size N of the studied model.

Knowledge of two largest eigenvalues and corresponding eigenvectors of approximated transfer matrices enables to obtain all thermodynamic functions, such as the free energy, magnetization, internal energy, correlation length etc. Moreover, the critical points as well as all critical exponents can be obtained from a particular model.

Let us consider a q-state Potts model of an interaction round a face (IRF) type [10] [1]. We shall construct transfer matrices from the single blocks (small transfer matrices) called the Boltzmann weights W_B. The Boltzmann weight of the IRF type consists of four q-state spin variables $\sigma := 0, 1, \ldots, q-1$ at each corner as depicted in Fig. 5.

[10] One can alternatively consider the vertex type, too.

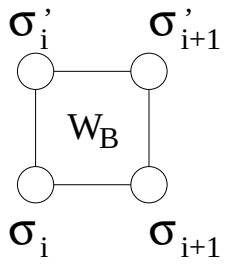

Fig. 5. The IRF Boltzmann weight constructed from the four q-state variables σ.

Thus, the transfer matrix $T^{(2N)}$ defined on two adjacent rows (each contains $2N$ sites) for open boundary conditions is then given by the product of the local Boltzmann weights W_B

$$T^{(2N)}(\sigma_1 \cdots \sigma_{2N}|\sigma'_1 \cdots \sigma'_{2N}) = \prod_{i=1}^{2N-1} W_B(\sigma_i\sigma_{i+1}|\sigma'_i\sigma'_{i+1}) \tag{59}$$

where W_B defined for the 2D classical q-state Potts model reads

$$W_B(\sigma_i\sigma_{i+1}|\sigma'_i\sigma'_{i+1}) = \exp\left\{-\frac{J}{k_BT}\left(\delta_{\sigma_i\sigma_{i+1}} + \delta_{\sigma'_i\sigma'_{i+1}} + \delta_{\sigma_i\sigma'_i} + \delta_{\sigma_{i+1}\sigma'_{i+1}}\right)\right\} \tag{60}$$

J, k_B and T being the interaction constant, the Boltzmann constant and temperature, respectively, and $\delta_{\sigma\sigma'}$ denotes the Kronecker function.

Let us write down a renormalized transfer matrix $\tilde{T}^{(2N)}$ in a product form of a left transfer matrix $\tilde{T}_L^{(N)}$, the Boltzmann weight W_B, and a right transfer matrix $\tilde{T}_R^{(N)}$ as

$$\begin{aligned}\tilde{T}^{(2N)}(\xi_L\sigma_L\sigma_R\xi_R|\xi'_L\sigma'_L\sigma'_R\xi'_R) &= \tilde{T}_L^{(N)}(\xi_L\sigma_L|\xi'_L\sigma'_L) \\ &\times W_B(\sigma_L\sigma_R|\sigma'_L\sigma'_R)\tilde{T}_R^{(N)}(\sigma_R\xi_R|\sigma'_R\xi'_R),\end{aligned} \tag{61}$$

where ξ is the multi-spin variable coming from a renormalization process which will be discussed in detail later within this section. The multi-spin variables ξ_L and ξ_R correspond to q-state grouped spins $\{\sigma_1 \cdots \sigma_{N-1}\}$ and $\{\sigma_{N+2} \cdots \sigma_{2N}\}$, respectively.

The DMRG renormalization process is developed to describe ground state properties of various models. Although the grouped spins $\{\sigma_1 \cdots \sigma_N\}$ characterize the q^N state variable, the renormalization process enables us to keep the size of the multi-spin variable ξ fixed while N increases. Then, ξ contains m values for arbitrary N. The renormalization is designed to enlarge the transfer matrix size by two q-state sites at each row within one step of the renormalization process. A mapping from $\tilde{T}^{(2N)}$ to $\tilde{T}^{(2N+2)}$ for large N keeps m fixed while the condition $m \ll q^N$ remains satisfied.

The renormalization process [11] starts with $N=2$ and $n=q$ in order to construct $T^{(4)}$ properly according to Eq. (61) as

$$T^{(4)} = W_BW_BW_B = T_L^{(2)}W_BT_R^{(2)}. \tag{62}$$

[11] In each renormalization step we perform $n \leftarrow n(q+1)$ while $n < m$, otherwise we keep fixed $n=m$ for successively increasing N.

The successive renormalization mapping

$$T^{(4)} = \tilde{T}^{(4)} \to \tilde{T}^{(6)} \to \cdots \to \tilde{T}^{(2N-2)} \to \tilde{T}^{(2N)} \tag{63}$$

allows us in high precision to approximate the ground state properties of the transfer matrix $\tilde{T}^{(2N)}$, such as the free energy, the spin magnetization, the spin-spin correlation function, etc.

At each renormalization step, the block-spin transformations $\{\xi_L\sigma_1\} \to \xi_L^{\rm new}$ and $\{\sigma_2\xi_R\} \to \xi_R^{\rm new}$ in the $\tilde{T}_L$ and $\tilde{T}_R$, respectively, are required to be carried out, as shown in Fig. 6.

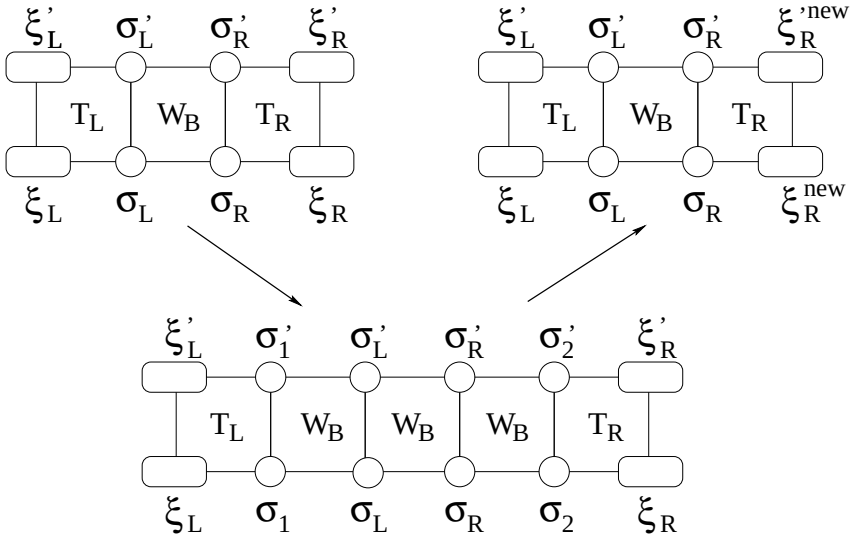

Fig. 6. The DMRG renormalization process $\tilde{T}^{(2N)} \to \tilde{T}^{(2N+2)}$.

Now, let us explain the details of the renormalization process for the left transfer matrix $\tilde{T}_L$, only. The same procedure is required for the $\tilde{T}_R$. If the transfer matrix of the model is symmetric, then $\tilde{T}_L$ and $\tilde{T}_R$ are mirror symmetric.

Firstly, we have to solve the eigenvalue problem

$$\sum_{\xi'_L\sigma'_L\sigma'_R\xi'_R} \tilde{T}^{(2N)}(\xi_L\sigma_L\sigma_R\xi_R|\xi'_L\sigma'_L\sigma'_R\xi'_R)\Psi(\xi'_L\sigma'_L\sigma'_R\xi'_R) = \lambda_{\max}\Psi(\xi_L\sigma_L\sigma_R\xi_R), \tag{64}$$

where $\lambda_{\max}$ is the largest eigenvalue and Ψ is its corresponding right eigenvector. In the same way we obtain the left [12] eigenvector Φ satisfying $\sum \Phi\tilde{T}^{(2N)} = \Phi\lambda_{\max}$. A partial product of Ψ and Φ characterizes the density matrix. The left and right density matrices obey the relations

$$\rho_L(\xi_L\sigma_L|\xi'_L\sigma'_L) = \sum_{\sigma''_R\xi''_R} \Phi(\xi_L\sigma_L\sigma''_R\xi''_R)\Psi(\xi'_L\sigma'_L\sigma''_R\xi''_R) \tag{65}$$

[12] For the symmetric transfer matrix $\tilde{T}^{(2N)}$, both eigenvectors, Ψ and Φ, are identical.

$$\rho_R(\sigma_R\xi_R|\sigma'_R\xi'_R) = \sum_{\xi''_L\sigma''_L} \Phi(\xi''_L\sigma''_L\sigma_R\xi_R)\Psi(\xi''_L\sigma''_L\sigma'_R\xi'_R) \tag{66}$$

By the complete diagonalization of the density matrix, we obtain the projection operators O and Q. In particular, for the ρ_L we get

$$\sum_{\xi_L\sigma_L\xi'_L\sigma'_L} O(i|\xi_L\sigma_L)\rho_L(\xi_L\sigma_L|\xi'_L\sigma'_L)Q(\xi'_L\sigma'_L|j) = \omega_i\delta_{ij}, \tag{67}$$

with O and Q being the complete sets of the left and the right eigenvectors [13] which correspond to the diagonal matrix ω_i consisting of all eigenvalues ordered decreasingly ($\omega_1 \geq \omega_2 \geq \cdots \geq \omega_{qm}$). The indices i and j run from 1 up to qm. Discarding the lowest eigenvalues ω_i and corresponding left and right eigenvectors in O and Q, respectively, we obtain an m by qm rectangular matrix O as well as a qm by m rectangular matrix Q, called projection operators because they are responsible for the renormalization (block-spin) transformation $\{\xi_L\sigma_1\} \to \xi_L^{\rm new}$. The projection operators enter the linear transformation of the left transfer matrix $\tilde{T}_L^{(N)}$ to a new $\tilde{T}_L^{(N+1)}$

$$\begin{aligned}\tilde{T}_L^{(N+1)}(\xi_L^{\rm new}\sigma_L|\xi_L'^{\rm new}\sigma'_L) = & \sum_{\xi_L\sigma_1\xi'_L\sigma'_1} O(\xi_L^{\rm new}|\xi_L\sigma_1)\tilde{T}_L^{(N)}(\xi_L\sigma_1|\xi'_L\sigma'_1) \\ & \times \quad W_B(\sigma_1\sigma_L|\sigma'_1\sigma'_L)Q(\xi'_L\sigma'_1|\xi_L'^{\rm new}).\end{aligned} \tag{68}$$

Analogously, the mapping $\tilde{T}_R^{(N)} \to \tilde{T}_R^{(N+1)}$ has to be carried out. By the construction of the product of $\tilde{T}_L^{(N+1)}W_B\tilde{T}_R^{(N+1)}$, the transfer matrix $\tilde{T}^{(2N+2)}$ is defined and the renormalization process given by the Eq. (63) is then completed.

DMRG is a very accurate numerical algorithm used to calculate not only the ground state properties. For instance, in one-dimensional case, we can extract the lowest energy (the ground state) of the Hamiltonian as well as several excited energies (states). The same approach can be applied to the two-dimensional classical system at finite temperatures[14] [12].

DMRG enables easily to observe almost all properties of statistical systems even at the criticality at which we frequently search information in order to extract the critical exponents. Although DMRG yields the mean-field-like behavior for small m, it is possible to obtain the correct critical exponents by increasing m in a vicinity of the criticality or by introducing a finite-size scaling to the system described by approximated transfer matrices [69, 70].

In order to obtain a spin magnetization per site $\langle\sigma\rangle$ at the center of the system, the following calculation is of use

$$\langle\sigma_L\rangle = \sum_{\xi_L\sigma_L\sigma_R\xi_R} \Phi(\xi_L\sigma_L\sigma_R\xi_R)\sigma_L\Psi(\xi_L\sigma_L\sigma_R\xi_R). \tag{69}$$

[13] For the DMRG technique it is very important to satisfy the condition $OQ = 1$.

[14] These considerations are, however, discussed for one-dimensional quantum models only and point out the reader how to treat the density matrices. Generalization to the two-dimensional classical models is straightforward.

The nearest-neighbor spin-spin correlation function is given by

$$\langle \sigma_L \sigma_R \rangle = \sum_{\xi_L \sigma_L \sigma_R \xi_R} \Phi(\xi_L \sigma_L \sigma_R \xi_R) \sigma_L \sigma_R \Psi(\xi_L \sigma_L \sigma_R \xi_R). \tag{70}$$

3.2 CTMRG method for 2D classical models

After Nishino formulated DMRG for two-dimensional classical models [32], the Corner Transfer Matrix Renormalization Group (CTMRG) method was proposed by Nishino and Okunishi [34, 35]. When applied to two-dimensional classical models, CTMRG is much faster than the DMRG method. The CTMRG is based on a unified scheme of the Baxter corner transfer matrix method [5, 6] and the White DMRG method [11, 12]. The key point is that a product of four the Baxter corner transfer matrices coincides with the DMRG density matrix [1, 3, 4]. Moreover, the DMRG as well as Baxter's variational methods on CTM have many common aspects, in particular, both of them are of a natural extension of the Kramers-Wannier approximation [2].

We will proceed similarly as in the previous section on DMRG method. Let us consider the q-state Potts model of the IRF type. The row-to-row transfer matrix is also expressed by Eq. (59). In order to simplify discussion, we assume the Boltzmann weight to be symmetric and isotropic, i. e.,

$$\begin{aligned} W_B(\sigma_i \sigma_{i+1} | \sigma'_i \sigma'_{i+1}) &= W_B(\sigma_{i+1} \sigma_i | \sigma'_{i+1} \sigma'_i) \\ &= W_B(\sigma'_i \sigma_i | \sigma'_{i+1} \sigma_{i+1}) \\ &= W_B(\sigma'_{i+1} \sigma'_i | \sigma_{i+1} \sigma_i). \end{aligned} \tag{71}$$

The renormalization of the transfer matrix can be expressed in the DMRG method as

$$T(\sigma_1 \sigma_2 \cdots \sigma_N | \sigma'_1 \sigma'_2 \cdots \sigma'_N) = \tilde{P}_L(\xi_L \sigma_i | \xi'_L \sigma'_i) \tilde{P}_R(\sigma_i \xi_R | \sigma'_i \xi'_R) \tag{72}$$

σ and ξ being the q-state and m-state multi-spin variables, respectively. The renormalized transfer matrix $\tilde{T}$ for the lattice with two additional columns has to be constructed as a scalar product of two Boltzmann weights W_B and two half row transfer matrices $\tilde{P}$, in particular, $\tilde{T} = \tilde{P}_L \cdot W_B \cdot W_B \cdot \tilde{P}_R$. The eigenvalue equation for $\tilde{T}$ is then

$$\begin{aligned} \sum_{\xi_L \sigma_1 \sigma_2 \sigma_3 \xi_R} & \tilde{P}_L(\xi_L \sigma_1 | \xi'_L \sigma'_1) W_B(\sigma_1 \sigma_2 | \sigma'_1 \sigma'_2) W_B(\sigma_2 \sigma_3 | \sigma'_2 \sigma'_3) \tilde{P}_R(\sigma_3 \xi_R | \sigma'_3 \xi'_R) \\ & \times V(\xi_L \sigma_1 \sigma_2 \sigma_3 \xi_R) = \lambda_{\max} V(\xi'_L \sigma'_1 \sigma'_2 \sigma'_3 \xi'_R) \end{aligned} \tag{73}$$

where $\lambda_{\max}$ is the largest non-degenerate eigenvalue of $\tilde{T}$ and V is the corresponding eigenvector. The density matrix ρ is defined as a partial product of the two eigenvectors

$$\rho(\xi_L \sigma_1 | \xi'_L \sigma'_1) = \sum_{\sigma_2 \sigma_3 \xi_R} V(\xi_L \sigma_1 \sigma_2 \sigma_3 \xi_R) V(\xi'_L \sigma'_1 \sigma_2 \sigma_3 \xi_R). \tag{74}$$

We have used the fact that V is real. The assumption that the model is symmetric and isotropic leads to $\tilde{P}_L = \tilde{P}_R$ and that the right and left eigenvectors are equivalent, too. The DMRG method is a systematic iterative procedure to obtain $\tilde{P}$ by using the information coming from the density matrix ρ.

Nishino and Okunishi gave their physical view on the density matrix ρ [33]. Since $\lambda_{\max}$ in Eq. (73) is the largest eigenvalue, the corresponding eigenvector V is given by the large L limit of the $(\tilde{T})^L X$, X being the vector that is not orthogonal to V. The vector $V(\xi_L\sigma_1\sigma_2\sigma_3\xi_R)$, therefore, represents the large Boltzmann weight for the lower (or upper) half-infinite two-dimensional lattice with the spin configuration $\{\xi_L\sigma_1\sigma_2\sigma_3\xi_R\}$ on the horizontal boundary. The density matrix equation (74) shows that ρ is created by a partial connection of the two halves of the lattice as shown in Fig. 7. Therefore, the density matrix ρ represents the entire system with a cut.

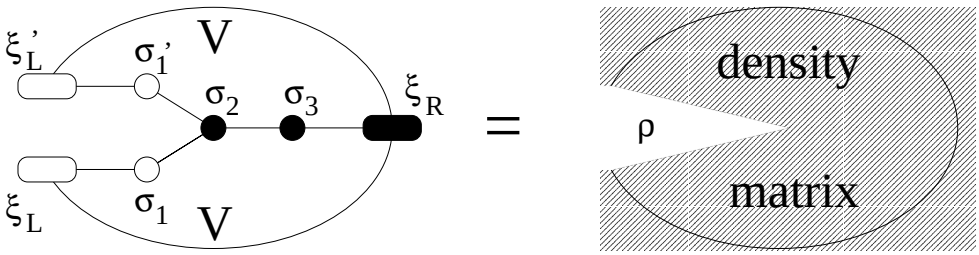

Fig. 7. The graphical representation of the density matrix ρ.

The physical background of the density matrix enables us to avoid the eigenvalue problem described by Eq. (73). *What is really necessary in the construction of the density matrix ρ, is the large Boltzmann weight that stands for the upper (or the lower) half-infinite lattice, and not the eigenvector V of the transfer matrix $\tilde{T}$.* How can we get ρ then? We have to introduce the Baxter corner transfer matrix (CTM) [1, 3, 4]. His expression for the half-infinite lattice V is given by the product of two CTMs denoted by $\tilde{C}'$

$$V(\xi_L\sigma_1\sigma_2\sigma_3\xi_R) \approx \sum_{\eta_M\sigma_4} \tilde{C}'(\sigma_2\sigma_1\xi_L|\sigma_2\sigma_4\eta_M)\tilde{C}'(\sigma_2\sigma_4\eta_M|\sigma_2\sigma_3\xi_R), \tag{75}$$

where $\tilde{C}'$ is the CTM representing the large Boltzmann weight for a quadrant (a corner) of the two-dimensional lattice. The graphical interpretation is shown in Fig. 8. The CTM element $\tilde{C}'(\sigma_1\sigma_2\xi|\sigma_1'\sigma_2'\xi')$ is zero if $\sigma_1 \neq \sigma_1'$. The notation '$\approx$' denotes that the right hand side of Eq. (75) is not the same as the eigenvector in Eq. (73), but is approximately exact. Further we decompose V into a product form $V \approx (\tilde{P}\cdot W_B \cdot W_B \cdot \tilde{P})(\tilde{C}\cdot\tilde{P}\cdot\tilde{P}\cdot\tilde{C})$, as is shown also in Fig. 8. The relation between $\tilde{C}$ and $\tilde{C}'$ is

$$\begin{aligned}\tilde{C}'(\sigma_2\sigma_1\xi_L|\sigma_2\sigma_5\eta_M) = \sum_{\zeta_L\sigma_4\eta_L} & W_B(\sigma_4\sigma_5|\sigma_1\sigma_2)\tilde{P}(\sigma_4\zeta_L|\sigma_1\xi_L) \\ & \times\tilde{P}(\sigma_4\eta_L|\sigma_5\eta_M)\tilde{C}(\sigma_4\zeta_L|\sigma_4\eta_L),\end{aligned} \tag{76}$$

where the symmetry of the Boltzmann weight W_B was used. The factor $W_B\cdot\tilde{P}\cdot\tilde{P}$ in Eq. (76) is a kind of the transfer matrix acting on $\tilde{C}$ and it increases the size of the corner. Substituting Eq. (75) into Eq. (74), we obtain new expression for the density matrix ρ

$$\rho(\xi_L\sigma_1|\xi_L'\sigma_1') = \sum_{\{\eta_M\eta_N\eta_R\sigma_2\sigma_3\sigma_4\sigma_5\}} \tilde{C}'(\sigma_2\sigma_1\xi_L|\sigma_2\sigma_4\eta_M)\tilde{C}'(\sigma_2\sigma_4\eta_M|\sigma_2\sigma_3\eta_R)$$

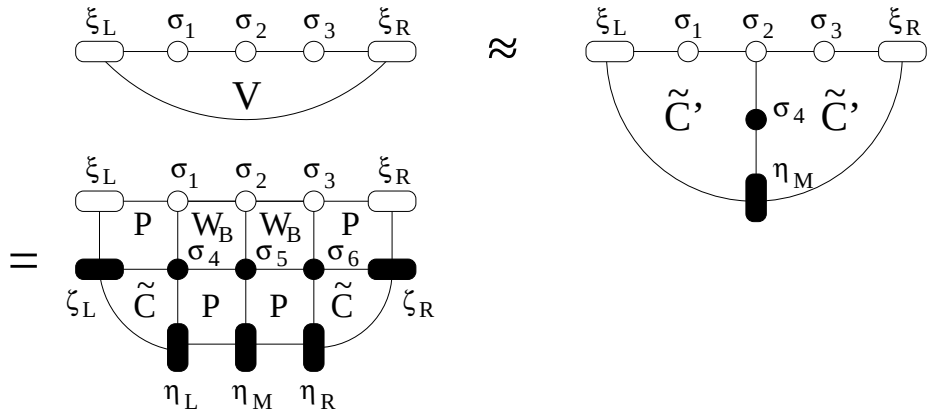

Fig. 8. The eigenvector V can be approximately expressed as the product of two corner transfer matrices, either by $\tilde{C}'$s according to Eq. (75) or by C's according to Eq. (76).

$$\times \tilde{C}'(\sigma_2\sigma_3\eta_R|\sigma_2\sigma_5\eta_N)\tilde{C}'(\sigma_2\sigma_5\eta_N|\sigma_2\sigma_1'\sigma_L'). \tag{77}$$

Thus, the density matrix is a product of four CTMs. The relation between ρ and $\tilde{C}'$ in Eq. (77) unifies the Baxter CTM method and the White DMRG one.

Now, we explain the key point of the new numerical method, which is hidden in a self-consistent relation between $\tilde{C}$ and $\tilde{C}'$. The relation consists of the mapping from $\tilde{C}$ to $\tilde{C}'$ as seen in Eq. (76) and the renormalization process from $\tilde{C}'$ to $\tilde{C}$ for all four CTMs (well-known in DMRG)

$$\sum_{\xi_L\eta_M\sigma_1\sigma_4} O^T(\zeta|\sigma_1\xi_L)\tilde{C}'(\sigma_2\sigma_1\xi_L|\sigma_2\sigma_4\eta_M)O(\sigma_4\eta_M|\zeta') \to \tilde{C}(\sigma_2\zeta|\sigma_2\zeta') \tag{78}$$

together with the renormalization process of $\tilde{P}$

$$\begin{aligned}\sum_{\xi_L\xi_L'\sigma_1\sigma_1'} & O^T(\eta_L|\sigma_1\xi_L)W_B(\sigma_2\sigma_1|\sigma_2'\sigma_1') \\ & \times P(\sigma_1\xi_L|\sigma_1'\xi_L')O(\sigma_1'\xi_L'|\eta_L') \to \tilde{P}(\sigma_2\eta_L|\sigma_2'\eta_L').\end{aligned} \tag{79}$$

The orthogonal matrix O represents the projection operator acting on the spin transformation and is obtained from the diagonalization of the density matrix ρ

$$\sum_{\xi_L\sigma_1\xi_L'\sigma_1'} O^T(\eta|\xi_L\sigma_1)\rho(\xi_L\sigma_1|\xi_L'\sigma_1')O(\xi_L'\sigma_1'|\zeta) = \delta_{\eta\zeta}\omega_\eta, \tag{80}$$

where O^T is the matrix transpose of the O and ω is the diagonal matrix containing m eigenvalues of the ρ after a truncation.

Both methods, DMRG and CTMRG yield the same results in the thermodynamic limit, however, the CTMRG method is much faster than DMRG. It is because the CTMRG creates ρ by using Eq. (77) which consists of the n^2m-dimensional matrix multiplication whereas the DMRG method requires to solve the n^2m^2-dimensional eigenvalue problem [32].

3.3 TPVA method for 3D classical models

The use of DMRG method has become very popular, especially for one-dimensional quantum and for two-dimensional classical systems. Nowadays, we observe first attempts to extend its numerical algorithm to higher dimensions, in particular, to two-dimensional quantum and to three-dimensional classical systems. In work of Liang and Pang [71], only the finite system algorithm for the two-dimensional quantum model was efficiently treated. So far, we do not know the answer how to solve two dimensional quantum models by infinite DMRG algorithm at zero temperature.

In 1999, Nishino and Okunishi proposed a way of extending DMRG to three-dimensional classical systems, the corner transfer tensor renormalization group (CTTRG) [72] as a three-dimensional generalization of the transfer matrix DMRG [10, 32] and the CTMRG [33] for the two-dimensional classical systems. There were two significant problems that occurred in the CTTRG algorithm: *i)* the calculated transition temperature $T_{\rm C}$ was much higher than the most reliable $T_{\rm C}$ obtained by the Monte Carlo simulations [73, 74]; *ii)* a very slow decay of the density-matrix eigenvalues [22] which was responsible for the low efficiency of the spin renormalization transformation.

It seems to be important to investigate the variational structure of DMRG when we attempt to focus on the generalization of DMRG to higher dimensions where the variational state of the transfer matrix or the Hamiltonian is written in a product of orthogonal matrices [75, 76].

Let us demonstrate the Tensor Product Variational Approach (TPVA) algorithm on the three-dimensional q-state Potts model of the IRF type. The variational energy and the variational partition function for a two-dimensional tensor product state V are given by the Reyleigh ratios

$$\lambda = \frac{\langle V|\mathcal{H}|V\rangle}{\langle V|V\rangle} \quad \text{and} \quad \frac{\langle V|T|V\rangle}{\langle V|V\rangle}, \tag{81}$$

$\mathcal{H}$ and T being the Hamiltonian for a two-dimensional quantum system and the transfer matrix for a three-dimensional classical system, respectively. Let us call such a variational estimate the Tensor Product Variational Approximation (TPVA) in the following. The key point in the TPVA is to find a good variational state V. Recently, Okunishi and Nishino [77] assumed a specific form [15] of V, which contains two variational parameters and tried to find the best V.

Let us consider a simple cubic lattice of the size $2N \times 2N \times \infty$ in x, y, and z directions, respectively, where free or fixed boundary conditions are imposed to both x and y directions. As we are interested in the bulk properties of the model, we suppose that the system size $2N$ is sufficiently large. We assume ferromagnetic interactions between the nearest neighbors. The transfer matrix is defined between two spin layers $[\sigma]$ and $[\bar{\sigma}]$

[15] The authors assumed V in the form of the Kramers-Wannier approximation and applied it to the 3D Ising model. However, they were not able to extend this approach to treat wider class of models, e. g., this problem is still open for the 3D Potts model.

each of the $2N \times 2N$ size. One spin layer $[\sigma]$ is given by a set of $4N^2$ spins

$$[\sigma] = \begin{bmatrix} \sigma_{1,1} & \cdots & \sigma_{1,N} & \cdots & \sigma_{1,2N} \\ \vdots & \ddots & \vdots & \ddots & \vdots \\ \sigma_{N,1} & \cdots & \sigma_{N,N} & \cdots & \sigma_{N,2N} \\ \vdots & \ddots & \vdots & \ddots & \vdots \\ \sigma_{2N,1} & \cdots & \sigma_{2N,N} & \cdots & \sigma_{2N,2N} \end{bmatrix}. \tag{82}$$

The layer-to-layer transfer matrix is expressed as a product of the Boltzmann weights

$$T[\sigma|\bar{\sigma}] \prod_{i=1}^{2N-1} \prod_{j=1}^{2N-1} X_{ij} = \prod_{\{ij\}} X_{ij} \equiv \prod_{\{ij\}} X\{\sigma_{ij}|\bar{\sigma}_{ij}\}, \tag{83}$$

X_{ij} being a local cube as seen in Fig. 9.

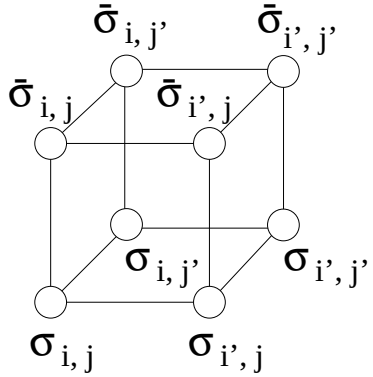

Fig. 9. Distribution of the spin variables in the Boltzmann weight X_{ij}. For further simplification, we introduce the notation $\{\mu_{ij}\}=\{\sigma_{ij}|\bar{\sigma}_{ij}\}$ as well as $i'=i+1$ and $j'=j+1$.

Let us focus on the simplest construction of the tensor product state of V, i. e.,

$$V[\sigma] = \prod_{\{ij\}} W_{ij} = \prod_{\{ij\}} W \begin{pmatrix} \sigma_{i,\ j} & \sigma_{i,\ j'} \\ \sigma_{i',\ j} & \sigma_{i',\ j'} \end{pmatrix} \equiv \prod_{\{ij\}} W\{\sigma_{ij}\}, \tag{84}$$

where the local tensor W_{ij} has q^4 parameters for the case of the q-state Potts model [16] and in the simplest formulation, W_{ij} is position independent and it represents a plaquette of four neighboring spins in a layer. Using $T[\sigma|\bar{\sigma}]$ and $V[\sigma]$, the variational partition function per layer according to Eq. (81) is expressed as

$$\lambda \quad = \quad \frac{\sum\limits_{[\sigma][\bar{\sigma}]} V[\sigma]T[\sigma|\bar{\sigma}]V[\bar{\sigma}]}{\sum\limits_{[\sigma]} \left(V[\sigma]\right)^2} = \frac{\sum\limits_{[\sigma][\bar{\sigma}]} \prod\limits_{\{ij\}} W\{\sigma_{ij}\}X\{\sigma_{ij}|\bar{\sigma}_{ij}\}W\{\bar{\sigma}_{ij}\}}{\sum\limits_{[\sigma]} \prod\limits_{\{ij\}} \left(W\{\sigma_{ij}\}\right)^2}$$

[16] Let us recall that the case $q=2$ is equivalent to 3D Ising model.

$$= \frac{\sum_{[\sigma][\bar{\sigma}]} \prod_{\{ij\}} G_1\{\sigma_{ij}|\bar{\sigma}_{ij}\}}{\sum_{[\sigma]} \prod_{\{ij\}} G_0\{\sigma_{ij}\}} \equiv \frac{Z_1}{Z_0}, \tag{85}$$

where we introduced G_0 and G_1 as

$$G_0\{\sigma_{ij}\} = (W\{\sigma_{ij}\})^2, \tag{86}$$

$$G_1\{\sigma_{ij}|\bar{\sigma}_{ij}\} = W\{\sigma_{ij}\}X\{\sigma_{ij}|\bar{\sigma}_{ij}\}W\{\bar{\sigma}_{ij}\}. \tag{87}$$

Above, Z_0 is the partition function of an IRF type on the $2N \times 2N$ square and Z_1 is that of the two-layer lattice model of the same size.

Let us explain the self-consistent equation for the variational state $V[\sigma]$. Eq. (85) is satisfied when λ is maximized. Therefore, we consider a variation of λ with respect to variations of local tensors, in particular,

$$\frac{\delta\ \lambda}{\delta\ V} \equiv \sum_{\{ij\}} \frac{\delta\ \lambda}{\delta\ W_{ij}} \tag{88}$$

under the condition that the system is large enough and the effect of boundaries is negligible. Then most of the terms on the right-hand-side of Eq. (88) are almost identical and it is sufficient to consider the variation of λ with respect to the local change $W_{NN} \to W_{NN} + \delta W_{NN}$ at the center of the system, where W_{NN} represents the central local tensor.[17]

Therefore, the variation $\delta\ \lambda/\delta\ W_{NN}$ can be explicitly written down by two matrices $A\{\sigma_{NN}\}$ and $B\{\sigma_{NN}|\bar{\sigma}_{NN}\}$. The first one is the diagonal matrix

$$A\{\sigma_{NN}\} = \sum_{[\sigma]'} \prod_{(ij)\neq(NN)} G_0\{\sigma_{ij}\} \tag{89}$$

where $\sum_{[\sigma]'}$ denotes the spin configuration sum for all the spins in the layer $[\sigma]$ except for the central spin plaquette $\{\sigma_{NN}\}$. [18] From definition (85)

$$Z_0 = \sum_{\{\sigma_{NN}\}} G_0\{\sigma_{NN}\}A\{\sigma_{NN}\}. \tag{90}$$

The second matrix is

$$B\{\sigma_{NN}|\bar{\sigma}_{NN}\} = X\{\sigma_{NN}|\bar{\sigma}_{NN}\} \sum_{[\sigma]'[\bar{\sigma}]'} \prod_{(ij)\neq(NN)} G_1\{\sigma_{ij}|\bar{\sigma}_{ij}\}, \tag{91}$$

which is related to Z_1 as

$$Z_1 = \sum_{\{\sigma_{NN}\}\{\bar{\sigma}_{NN}\}} W\{\sigma_{NN}\}B\{\sigma_{NN}|\bar{\sigma}_{NN}\}W\{\bar{\sigma}_{NN}\}. \tag{92}$$

[17] compare Eqs. (82) and (84).

[18] We interpret $A\{\sigma_{NN}\}$ as a 16-dimensional matrix $M\{\sigma_{NN}|\bar{\sigma}_{NN}\}$ where $M\{\sigma_{NN}|\sigma_{NN}\} = A\{\sigma_{NN}\}$ and is zero when $\{\sigma_{NN}\} \neq \{\bar{\sigma}_{NN}\}$.

With these definitions of $A\{\sigma_{NN}\}$ and $B\{\sigma_{NN}|\bar{\sigma}_{NN}\}$ we can calculate λ via

$$\lambda = \frac{Z_1}{Z_0} = \frac{\sum\limits_{\{\sigma_{NN}\}\{\bar{\sigma}_{NN}\}} W\{\sigma_{NN}\}B\{\sigma_{NN}|\bar{\sigma}_{NN}\}W\{\bar{\sigma}_{NN}\}}{\sum\limits_{\{\sigma_{NN}\}} W\{\sigma_{NN}\}A\{\sigma_{NN}\}W\{\sigma_{NN}\}}. \tag{93}$$

The condition $\delta\ \lambda/\delta\ W_{NN} = 0$ leads to the eigenvalue problem

$$\sum_{\{\bar{\sigma}\}} \frac{1}{A\{\sigma\}} B\{\sigma|\bar{\sigma}\}W\{\bar{\sigma}\} = \lambda W\{\sigma\}. \tag{94}$$

We have dropped the subscript from σ_{NN} and $\bar{\sigma}_{NN}$. We consider $W\{\sigma\}$ as a 16-dimensional vector. The Eq. (94) is the self-consistent equation that an optimized tensor product state $V[\sigma]$ should satisfy.

In order to apply the self-consistent relation (94), we have to obtain $A\{\sigma\}$ and $B\{\sigma|\bar{\sigma}\}$ for very large N. Although it is impossible to obtain them exactly, we use the CTMRG [33] which enables us to calculate them numerically with high precision for large N. We introduce the notation

$$\mu_{ij} \equiv (\sigma_{ij}\ ,\ \bar{\sigma}_{ij}) \tag{95}$$

that groups a pair of adjacent spins σ_{ij} and $\bar{\sigma}_{ij}$. Knowing μ_{ij} we can rewrite the stack of two plaquette spins $\{\sigma_{ij}|\bar{\sigma}_{ij}\}$ in the form

$$\{\mu_{ij}\} = \begin{pmatrix} \mu_{i,\ j} & \mu_{i,\ j'} \\ \mu_{i',\ j} & \mu_{i',\ j'} \end{pmatrix}, \tag{96}$$

$X\{\sigma_{ij}|\bar{\sigma}_{ij}\}$ to $X\{\mu_{ij}\}$, and $G_1\{\sigma_{ij}|\bar{\sigma}_{ij}\}$ to $G_1\{\mu_{ij}\}$. Analogously, we drop the subscript from $\{\mu_{ij}\}$ to write it as $\{\mu\}$ in the following when its position is apparent.

The matrices $A\{\sigma\}$ and $B\{\mu\}$ can be expressed as a combination of the corner transfer matrices (CTMs) and the half-row transfer matrices (HRTMs) which appear when we apply CTMRG to both the numerator as well as the denominator in Eq. (85) in order to obtain Z_1 and Z_0 [77], respectively.

Let us write the CTM used for the calculation of Z_1 and Z_0 as $C_1(\zeta\mu\zeta')$ and $C_0(\xi\sigma\xi')$, respectively, where ξ, ξ', ζ, and ζ' are m-state multi-spin variables and μ is a q^2-state variable. Similarly, let us write HRTM as $P_1(\zeta\mu\mu'\zeta')$ and $P_0(\xi\sigma\sigma'\xi')$ in the same manner. Note that $G_0\{\sigma\}$ is necessary for the creation of $C_0(\xi\sigma\xi')$ and $P_0(\xi\sigma\sigma'\xi')$ and $G_1\{\mu\}$ for $C_1(\zeta\mu\zeta')$ and $P_1(\zeta\mu\mu'\zeta')$. In particular, $A\{\sigma\}$ and $B\{\mu\}$ are constructed as

$$\begin{aligned} A\{\sigma\} = \sum_{\xi_1\xi_2\cdots\xi_8} & P_0(\xi_1\sigma_a\sigma_b\xi_2)C_0(\xi_2\sigma_b\xi_3)P_0(\xi_3\sigma_b\sigma_c\xi_4)C_0(\xi_4\sigma_c\xi_5) \\ & P_0(\xi_5\sigma_c\sigma_d\xi_6)C_0(\xi_6\sigma_d\xi_7)P_0(\xi_7\sigma_d\sigma_a\xi_8)C_0(\xi_8\sigma_a\xi_1) \end{aligned} \tag{97}$$

$$\begin{aligned} B\{\mu\} = X\{\mu\} \sum_{\zeta_1\zeta_2\cdots\zeta_8} & P_0(\zeta_1\mu_a\mu_b\zeta_2)C_0(\zeta_2\mu_b\zeta_3)P_0(\zeta_3\mu_b\mu_c\zeta_4)C_0(\zeta_4\mu_c\zeta_5) \\ & P_0(\zeta_5\mu_c\mu_d\zeta_6)C_0(\zeta_6\mu_d\zeta_7)P_0(\zeta_7\mu_d\mu_a\zeta_8)C_0(\zeta_8\mu_a\zeta_1) \end{aligned} \tag{98}$$

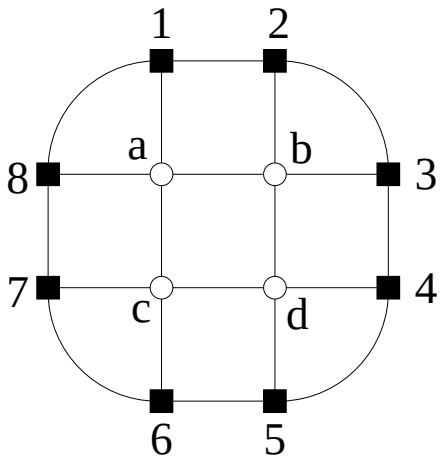

Fig. 10. The four white circles denote q and q^2-state variables of the plaquette spins $\{\sigma\}$ and $\{\mu\}$, respectively, and the black squares are the summed m-state multi-spin variables ξ and ζ used in the CTMRG technique.

where the positions of the spin variables are shown in Fig. 10.

Thus constructed $A\{\sigma\}$ and $B\{\mu\}$ enter the self-consistent Eq. (94) and by an iterative procedure [36], the $W\{\sigma\}$ is improved. The extension of the system size is performed by CTMRG. After $W\{\sigma\}$ reaches its fixed point we can measure thermodynamic bulk properties such as the three-dimensional magnetization per one site (the order parameter)

$$M = \frac{q\langle\delta_{0,a}\rangle - 1}{q-1}, \tag{99}$$

where

$$\delta_{0,a} = \frac{\sum\limits_{\mu_a\zeta_1\zeta_2\zeta_3\zeta_4} \delta_{0,a} C_1(\zeta_1\mu_a\zeta_2)C_1(\zeta_2\mu_a\zeta_3)C_1(\zeta_3\mu_a\zeta_4)C_1(\zeta_4\mu_a\zeta_1)}{\sum\limits_{\mu\zeta_1\zeta_2\zeta_3\zeta_4} C_1(\zeta_1\mu_a\zeta_2)C_1(\zeta_2\mu_a\zeta_3)C_1(\zeta_3\mu_a\zeta_4)C_1(\zeta_4\mu_a\zeta_1)}, \tag{100}$$

the internal energy [77] per site

$$E^{\rm int} = -\langle\delta_{\sigma_{i,j},\sigma_{i',j}}\rangle - \langle\delta_{\sigma_{i,j},\sigma_{i,j'}}\rangle - \langle\delta_{\sigma_{i,j},\bar{\sigma}_{i,j}}\rangle, \tag{101}$$

or the free energy [77] per site

$$F = -\frac{1}{8}k_BT \lim_{N\to\infty} \ln\left(\frac{Z_1^{[N+4]}Z_0^{[N+2]}Z_0^{[N+2]}Z_1^{[N]}}{Z_0^{[N+4]}Z_1^{[N+2]}Z_1^{[N+2]}Z_0^{[N]}}\right), \tag{102}$$

where $Z_0^{[N]}$ denotes the system size of $N \times N$.

4 Finite-size scaling

4.1 Phenomenological renormalization

The DMRG algorithm can be used in two ways. The first one is the infinite system method (ISM), which enlarges the system size to an arbitrary size. Then, the spontaneous symmetry-breaking occurs if the system is below the critical temperature. Thus we can obtain properties of the system in the thermodynamic limit.

In the second way, the finite system method (FSM), it is used when we are interested in properties of the finite-sized system. Results obtained by this way can enter, e. g., the finite-size scaling. These ideas come from the Nightingale's phenomenological renormalization [95] (or by other words, the finite-size scaling). The combination of finite-size scaling with the transfer matrix technique yields a powerful tool for investigation of the critical behavior. In particular, it has been widely used to study two-dimensional statistical mechanical systems and one-dimensional quantum mechanical ones.

Although, finite systems themselves do not display any critical behavior, they enable to detect critical points as well as critical exponents. For this purpose, let us consider the Ising model on a simple square lattice where spins are coupled among nearest neighbors only. For the lattice size of $n \times \infty$, the eigenvalues of the transfer matrix

$$\lambda_0^{(n)} > \lambda_1^{(n)} > \cdots > \lambda_{2^n}^{(n)} \tag{103}$$

yield the free energy per site

$$f_n = -\frac{1}{n} k_B T \ln \lambda_0^{(n)} \tag{104}$$

and the inverse correlation length

$$\kappa_n \equiv \xi_n^{-1} = \ln \left(\frac{\lambda_0^{(n)}}{\lambda_1^{(n)}} \right). \tag{105}$$

A system approaching its critical point is characterized by a temperature-like field (i. e., non-ordering field) and an ordering field, denoted by ε and h, respectively. Assume $\varepsilon = h = 0$ to be the critical point. For the finite-sized systems a third condition implies: $n^{-1} \to 0$.

Kadanoff's well-known scaling relations [7] for a d-dimensional system can be generalized for the free energy and the inverse correlation length to include $1/n$ as

$$L^d f(\varepsilon, h, \frac{1}{n}) = L^d g_L(\varepsilon, h) + f(\varepsilon_L, h_L, \frac{L}{n}), \tag{106}$$

$$L\kappa(\varepsilon, h, \frac{1}{n}) = \kappa(\varepsilon_L, h_L, \frac{L}{n}). \tag{107}$$

where L is the arbitrary linear dimension of the Kadanoff blocks; g_L is their internal free energy per site and is related to the regular part of the free energy. The ε_L and h_L are the renormalized temperature and ordering (magnetic) field. Under scaling the system

size n reduces to n/L, implying that $1/n$ is a scaling field with exponent equal to 1. Close to the critical point we can write

$$\varepsilon_L(\varepsilon, 0) = \varepsilon L^{y_\mathrm{T}} + \mathcal{O}(\varepsilon^2), \tag{108}$$

$$h_L(0, h) = hL^{y_\mathrm{h}} + \mathcal{O}(h^2). \tag{109}$$

4.2 Critical exponents

All critical exponents can be expressed in terms of two fundamental thermal and magnetic exponents y_T and y_h, respectively. From Eqs. (106) through (109) we can derive how the specific heat c_n, susceptibility χ_n, and the inverse correlation length κ_n, its derivatives with respect to temperature T and field h squared κ_n^T and κ_n^h behave as a function of system size [19] at $\epsilon = h = 0$:

$$c_n \sim n^{2y_\mathrm{T}-d} \tag{110}$$

$$\chi_n \sim n^{2y_\mathrm{h}-d} \tag{111}$$

$$\kappa_n \sim n^{-1} \tag{112}$$

$$\kappa_n^\mathrm{T} \sim n^{y_\mathrm{T}-1} \tag{113}$$

$$\kappa_n^\mathrm{h} \sim n^{y_\mathrm{h}-1} \tag{114}$$

Once the free energy, inverse correlation length, and their derivatives have been calculated for finite systems, the relations (110) through (114) may be employed to obtain critical properties.

In order to obtain the critical point of a particular model, we use Eq. (112) for several different lattice sizes n. The larger n we take, the more accurate K_c^* we obtain, see Fig. 11. The K^* is the point, where two curves $n\kappa_\mathrm{n}$ as functions of temperature T (or the inverse temperature K) for two different lattice sizes n and m intersect each other, we call K^*. In DMRG treatment we usually take $m = n+2$, as the system size is enlarged by 2 sites at each iteration step.

Analogously, we can calculate critical exponents. Thus, e. g., the thermal critical exponent y_T can be extracted from Eq. (113) as it can be read off from the slopes of the curves κ_n and κ_{n+2} at their intersection point as

$$y_\mathrm{T} = \ln\left(\frac{n\kappa_n^\mathrm{T}}{(n+2)\kappa_{n+2}^\mathrm{T}}\right) / \ln\left(\frac{n}{n+2}\right) \tag{115}$$

or the magnetic exponent y_h can be derived from Eq. (111) as

$$y_\mathrm{h} = \ln\left(\frac{n^d\chi_n}{(n+2)^d\chi_{n+2}}\right) / 2\ln\left(\frac{n}{n+2}\right), \tag{116}$$

where we will use the dimension $d = 2$ and χ_n comes out from Eq. (111). All critical exponents can be derived from y_T and y_h [107], i. e.,

$$\alpha = 2 - \frac{2}{y_\mathrm{T}}, \tag{117}$$

[19] assuming a vanishing first-order derivative with respect to h in the view of $h \to -h$ symmetry.

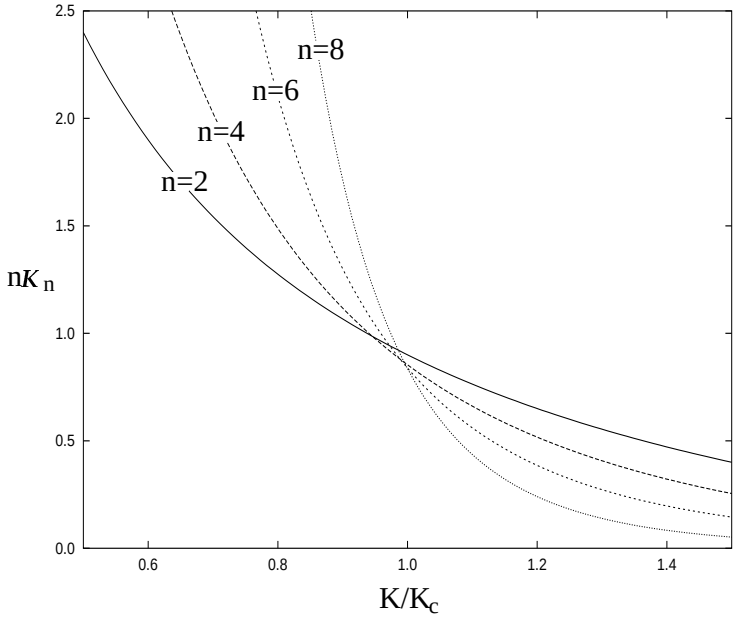

Fig. 11. Typical plots of the phenomenological renormalization for the inverse correlation length κ_n multiplied by n as a function of inverse temperature K

$$\beta = \frac{2 - y_{\rm h}}{y_{\rm T}}, \tag{118}$$

$$\gamma = y_{\rm h} - \beta, \tag{119}$$

$$\delta = \gamma/\beta + 1, \tag{120}$$

$$\eta = 2 - \gamma y_{\rm T}, \tag{121}$$

$$\nu = y_{\rm T}^{-1}. \tag{122}$$

Since DMRG method enables to obtain the two largest eigenvalues of a large approximated transfer matrix of size n, the finite-size scaling analysis becomes a very useful tool to investigate critical properties of various kinds of two-dimensional models.

5 Applications to 2D and 3D classical models

5.1 Phase diagrams of ANNNI and ATNNI models

We will investigate two classical spin lattice models that exhibit incommensurate (IC) phases, namely the Anisotropic Next-Nearest-Neighbor Ising (ANNNI) model [78] and the Antiferromagnetic Triangular Nearest-Neighbor Ising (ATNNI) model [80]. The incommensurate phases were studied by many various theoretical approaches. The free fermion approximation revealed IC phase in 2D classical ANNNI model [81] (also in ATNNI model [80]) and in 2D incommensurate crystals [82]. Incommensurate structures have been discussed in various topics: 2D C-IC phase transition [83], 2D quantum ANNNI model [84], ANNNI model in $d > 2$ dimensions [85], and by analyzing 1D sine-Gordon model [86], where the authors found no Lifshitz point.

We develop modified DMRG method which can be applied to more complicated systems, namely to the ANNNI and ATNNI models. Both models are characterized by non-symmetric transfer matrices. The way how to use the DMRG in that case will be described in this Section. We show the modification of the DMRG for treating non-symmetric transfer matrix in the ATNNI model and discuss it in light of other approaches to the non-symmetric transfer matrices or non-hermitian quantum Hamiltonians [82–88]. In particular, the existence or non-existence of the Lifshitz point in the ATNNI model will be studied and its phase diagrams will be constructed.

5.1.1 The DMRG technique for 2D spin systems

For special values of interaction constants, both the ATNNI and ANNNI models can be reduced to the Ising one. In this case we can compare our approximate DMRG calculations with the exact results for infinite 2D models.

Exact results can be relatively easily obtained for 1D models, e.g. strips of finite width. They provide also a good opportunity for testing our methods.

The DMRG technique, as a numerical real-space method, is in fact always applied to finite systems. However, in dependence on the size of the system, it can yield approximate descriptions of 1D or 2D infinite systems.

An 1D model at non-zero temperature does not display any phase transitions. Nevertheless, the value of the critical temperature for the corresponding 2D model can be found from considerations of the phenomenological renormalization [95] which we here call the finite-size scaling (FSS). This approach represents the **first** of *two methods* we shall use for determination of the critical temperature. For the Ising model, derived from comparing two rescaled semi-infinite strips of width L=12 and 14 with periodic boundary conditions, [20] the critical temperatures are the following:

i) $T_c = 2.26987$ from exact eigenvalues of the transfer matrices of sizes 2^{12} and 2^{14} which correspond to the transfer matrix dimensions $N = 4096$ and $N = 16384$, respectively,

[20] Details of periodic boundary conditions applied to DMRG for two-dimensional classical lattice models are discussed in Sec. 5.2.

ii) $T_c = 2.27008$ from eigenvalues of the DMRG superblock transfer matrices with the dimension of only $N = 1024$
comparing to the exact critical temperature of 2D Ising model $T_c = 2.26918\ldots$ [1].

The **second** method for determination of the critical temperature is provided by DMRG calculations on 2D systems, large in both directions. Here, below the critical temperature a spontaneous symmetry breaking occurs, i.e. the order parameter acquires non-zero values and tends to zero at the critical point. The DMRG method behaves in a mean-field-like manner. Now the critical temperature T_c can be determined directly and therefore no finite-size scaling is necessary. Its accuracy improves with the size $N = 2^L$ (or multi-spin variable m discussed in Sec. 3.1) of the superblock transfer matrix:

$T_c = 2.275$ m=16 N=1024
$T_c = 2.272$ m=30 N=3600
$T_c = 2.2692$ m=70 N=19600

For lower orders of approximation, the accuracy of the **second** method is worse than of the **first** one, but it converges faster to the exact value. For the ATNNI and ANNNI models in the phases with broken symmetry, the method explicitly gives the structure of a commensurate as well as an of incommensurate phase. In contrast to the FSS method, it is also applicable to the high magnetic field region in the ATNNI model and we were able to investigate nearly the whole phase diagram of the model.

5.1.2 The ATNNI and ANNNI models

We consider the two-dimensional classical Ising model with antiferromagnetic interactions between nearest neighbors on a triangular lattice (the ATNNI model). Its Hamiltonian is

$$\mathcal{H} = \sum_i J \left(\sum_{\hat{\delta}=\hat{1},\hat{2}} \sigma_i \sigma_{i+\hat{\delta}} + \alpha \sigma_i \sigma_{i+\hat{3}} \right) - H \sum_i \sigma_i \tag{123}$$

with $J > 0$, $0 < \alpha < 1$, and the directions $\hat{1}$, $\hat{2}$, $\hat{3}$ where $\sigma_i = \pm 1$ as depicted in Fig. 12(a).

The partition function $\mathcal{Z} = \sum_{\{\sigma\}} e^{-\beta\mathcal{H}}$, where $\beta = (k_B T)^{-1}$, can be written as a product of two types of Boltzmann weights. Each Boltzmann weight $W_B(\sigma_1\sigma_2|\sigma_1'\sigma_2')$ is composed of four spins which interact among themselves as seen in Fig. 13.

The model is exactly solvable for external magnetic field $H = 0$. At nonzero temperature ($T_c \approx 1.55$ for $\alpha = 0.4$ [80]), it exhibits a second order phase transition. Throughout this Section all numerical calculations are performed at the fixed $\alpha = 0.4$, $J = 1$. The dimensionless temperature T/J and dimensionless ratio H/T are used in order to compare our results with those obtained in [80].

The numerical calculations are based on a diagonalization of two transfer matrices (in next Section, we will offer a more detailed description of their construction). For this purpose we used a rectangular lattice depicted in Fig. 12(b) which is related to the initial triangular lattice of the ATNNI model as seen in Fig. 12(a). We identify direction $\hat{3}$ with the interaction αJ (Figs. 12(a) and 12(b)). Along this direction, the incommensurate modulation should appear. We will use the row-to-row transfer matrices [80].

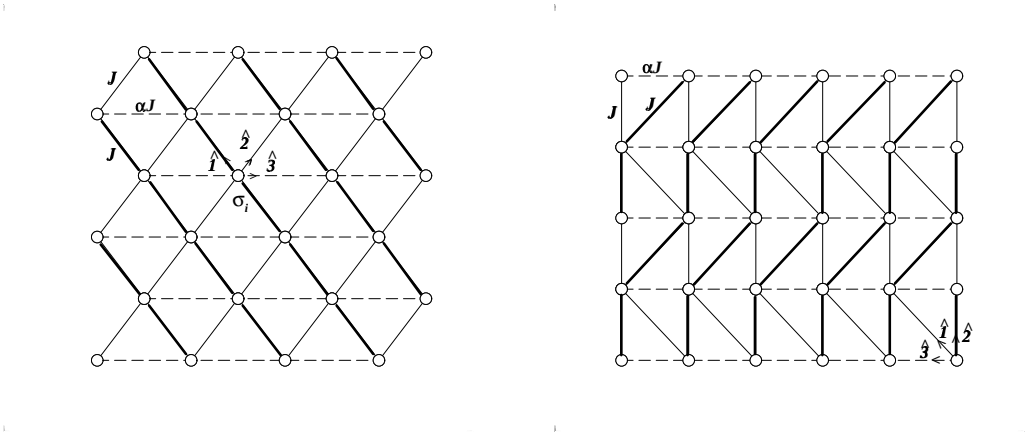

(a) (b)

Fig. 12. (a) the triangular lattice of the ATNNI model. The incommensurate structure appears along the direction $\hat{3}$ (dashed lines). (b) for more convenient calculation, the triangular lattice was transformed to a rectangular one. The transfer matrices are of the row-to-row type. Now, directions $\hat{1}$, $\hat{2}$ in (a) correspond to thick and thin lines in (b), respectively.

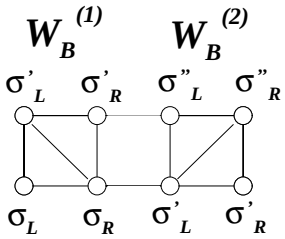

Fig. 13. Two kinds of the Boltzmann weights differing by orientation of diagonal interactions.

The ANNNI model is defined on the 2D triangular lattice (Fig. 14). The model is characterized by the nearest-neighbor ferromagnetic interactions $J_1 < 0$ for all three directions and a next-nearest-neighbor antiferromagnetic interaction $J_2 > 0$ in one of three directions only. Its Hamiltonian can be written as

$$\mathcal{H} = \sum_i \left(\sum_{\hat{\delta}=\hat{1},\hat{2},\hat{3}} J_1 \sigma_i \sigma_{i+\hat{\delta}} + J_2 \sigma_i \sigma_{i+\hat{4}} \right) . \tag{124}$$

The ANNNI model is usually defined on the square lattice where the next-nearest-neighbor interactions are, in fact, equal to zero and the third-nearest-neighbor ones are non-zero and antiferromagnetic. Thus, the ANNNI model on triangular lattice is the genuine Anisotropic Next-Nearest-Neighbor Interaction model with non-zero next-nearest-neighbor interactions and vanishing the third-nearest-neighbor ones. A frustration of

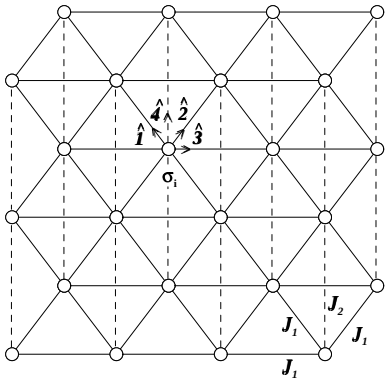

Fig. 14. The 2D ANNNI model on the triangular lattice. Directions $\hat{1}$, $\hat{2}$, and $\hat{3}$ characterize the ferromagnetic interaction J_1. The next-nearest-neighbor antiferromagnetic interaction J_2 (dashed line) acts in the direction $\hat{4}$ in which the incommensurate phase appears.

the ANNNI model appears due to the competing interactions. The ANNNI model was mostly studied on the square lattice [96, 97] but it was shown by [78] that the properties of the ANNNI model on the triangular lattices remain essentially unchanged. The Boltzmann weight is composed of six spins $W_B(\sigma_1\sigma_2\sigma_3|\sigma_1'\sigma_2'\sigma_3')$ an it is graphically shown in Fig. 15.

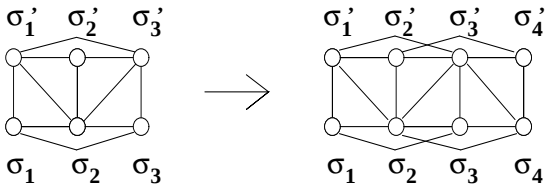

Fig. 15. The six-spin Boltzmann weights of the ANNNI model differing from each other by orientation of the diagonal interactions. In the DMRG calculation the Boltzmann weight defined on the eight-spin cluster was used. It is composed of two overlapping six-spin Boltzmann weights.

The phase diagram of the ANNNI model (will be discussed in Sec. 2.1.4) consists of four regions: a ferromagnetic phase with non-zero total magnetization, a commensurate phase $\langle 2\rangle$ with periodically alternating spin signs $(\cdots++--++--\cdots)$, a paramagnetic phase, and an incommensurate phase located between the commensurate and paramagnetic phases.

5.1.3 Modification of the DMRG algorithm

The DMRG algorithm for quantum models introduced by White [11, 12] was modified and applied for 2D classical lattice models by Nishino [32]. Since the ATNNI and ANNNI models on the triangular lattice lead to non-symmetric transfer matrices and incommensurate phases, the Nishino's approach has to be modified further. We shall pursue the second approach discussed in Section 2 – the DMRG method applied to very wide strips where the spontaneous symmetry breaking occurs.

The DMRG method replaces the exact row-to-row transfer matrix of a strip, which is a product of plaquette Boltzmann weights by a set of much smaller superblock transfer matrices for every plaquette. The superblock transfer matrix consists of the Boltzmann weight ${}^iW_B$ of the plaquette i multiplied by left and right transfer matrices (blocks) ${}^iT_L$, ${}^iT_R$ which replace all the remaining plaquette Boltzmann weights of the exact transfer matrix to the left and right from the plaquette. The left and right transfer matrices are indexed by left and right spins $\sigma_{L,R} = \pm 1$ of the plaquette, respectively, and by block-spin variables $\xi = 1, \ldots, m$. The number of spin components m determines the order of the approximation. For a modulated phase, ${}^iT_L$ and ${}^iT_R$ differ for each plaquette. In the Finite System Method (FSM), they are calculated self-consistently from the transfer matrices corresponding to the neighboring plaquettes. The left block ${}^{i+1}T_L$ is obtained from ${}^iT_L\,{}^iW_B$ after a reduction of its matrix size to the original value in a proper way. The right block ${}^{i-1}T_R$ is similarly calculated from ${}^iW_B\,{}^iT_R$. A calculation of the left and right transfer matrices is performed iteratively in the course of a number of sweeps across the strip.

The reduction of the size of the transfer matrices is based on density matrices that are constructed from the left and right eigenvectors (see also Figs. 12(b) and 16) of the superblock matrix [12].

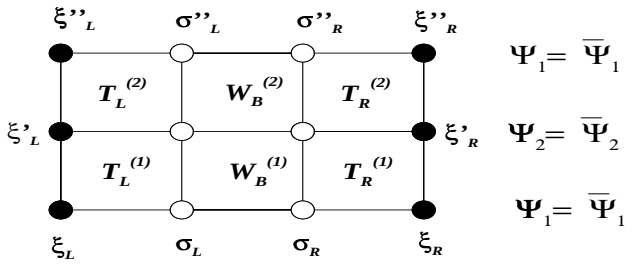

Fig. 16. Ψ_1, $\overline{\Psi}_1$ are the right and left eigenvectors that correspond to the largest eigenvalue of the superblock transfer matrices ${}^iT^{(1)} = {}^iT_L^{(1)}\,{}^iW_B^{(1)}\,{}^iT_R^{(1)}$ and ${}^iT^{(2)} = {}^iT_L^{(2)}\,{}^iW_B^{(2)}\,{}^iT_R^{(2)}$, respectively. Vectors Ψ_2 and $\overline{\Psi}_2$ are used for the calculation of the density matrix in each DMRG iteration.

The procedure described above for homogeneous phases and symmetric transfer matrices is explained in the Section 1.1 in detail. For the ATNNI and ANNNI models the method should be slightly modified because the transfer matrices are not symmetric and the structure is modulated in both directions (in one of the directions, it is modulated incommensurately). It is convenient to choose the strip perpendicularly to the direction

of the incommensurate modulation with commensurate structure along the strip, i.e. the strip is orientated in the vertical direction of the lattice shown in Fig. 12(b). It is seen that there are two different row-to-row non-symmetric transfer matrices in the strip. One transfer matrix is constructed from the Boltzmann weight $W_B^{(1)}$ and the other one from the $W_B^{(2)}$ (Figs. 12(b) and 16).

The number of superblock transfer matrices should be equal to 2 (at least), since there are the 2 different Boltzmann weights in the model. For the DMRG with spontaneous symmetry breaking and spatially modulated structures, they may be different for each plaquette of the lattice. The density matrices can be constructed either from the eigenvectors of the superblock transfer matrices or from functions obtained by an iterative procedure $\Psi_j = \prod_{k=1}^{j} T^{(k)} \Psi_{init}$ starting from Ψ_{init} given by suitable boundary conditions. For a homogeneous structure and large j the function Ψ_j is identical to the eigenvector of the superblock T.

All the commensurate structures have the period 2 for the ATNNI model in the direction of the strip. Therefore, we use two superblock transfer matrices $T^{(1)} = T_L^{(1)} W_B^{(1)} T_R^{(1)}$ and $T^{(2)} = T_L^{(2)} W_B^{(2)} T_R^{(2)}$ shown in Fig. 16. They are dependent on the position of the plaquette in the horizontal direction (perpendicular to the strip). Similarly, as a result of the iteration procedure we obtain two different functions Ψ_j for sufficiently large j. Let us denote Ψ_1 to be the eigenvector of the matrix $T^{(2)}T^{(1)}$ for even j and Ψ_2 to be another eigenvector of the matrix product $T^{(1)}T^{(2)}$ for odd j. Both these combined matrices are already symmetric and their right and left eigenvectors Ψ and $\overline{\Psi}$, respectively, are identical.

Writing spin variables explicitly, the right eigenvectors are given by

$$\sum_{\xi_L \sigma_L \sigma_R \xi_R} T(\xi_L'' \sigma_L'' \sigma_R'' \xi_R'' | \xi_L \sigma_L \sigma_R \xi_R) \Psi_1(\xi_L \sigma_L \sigma_R \xi_R) = \lambda \Psi_1(\xi_L'' \sigma_L'' \sigma_R'' \xi_R''), \tag{125}$$

where

$$T(\xi_L'' \sigma_L'' \sigma_R'' \xi_R'' | \xi_L \sigma_L \sigma_R \xi_R)$$

$$= \sum_{\xi_L' \sigma_L' \sigma_R' \xi_R'} T^{(2)}(\xi_L'' \sigma_L'' \sigma_R'' \xi_R'' | \xi_L' \sigma_L' \sigma_R' \xi_R') T^{(1)}(\xi_L' \sigma_L' \sigma_R' \xi_R' | \xi_L \sigma_L \sigma_R \xi_R). \tag{126}$$

The eigenvectors at odd rows Ψ_2 follow directly from Ψ_1

$$\Psi_2 = T^{(1)} \Psi_1. \tag{127}$$

The optimum size reduction of the matrix ${}^iT_L \, {}^iW_B$ is performed by its multiplying at both sides by rectangular matrices consisting of several eigenvectors of a density matrix that corresponds to its largest eigenvalues [12, 32]. The density matrix at a row j is constructed from the left and right eigenvectors $\Psi_j, \overline{\Psi}_j$ [79] of transfer matrices with their left and right spins, respectively, within the lattice row. For modulated commensurate structures of a period p, the successive functions Ψ_j are not the eigenvectors of one transfer matrix but of a product of p transfer matrices. As for ATNNI model we have two different kinds of rows and different left and right transfer matrices in superblocks,

we need four different density matrices. The left density matrices have the following forms:

$$\rho_L^{(1)}(\xi_L^a\sigma_L^a|\xi_L^b\sigma_L^b) = \sum_{\sigma_R^c\xi_R^c} \Psi_1(\xi_L^a\sigma_L^a\sigma_R^c\xi_R^c)\overline{\Psi}_1(\xi_L^b\sigma_L^b\sigma_R^c\xi_R^c) \tag{128}$$

$$\rho_L^{(2)}(\xi_L'^a\sigma_L'^a|\xi_L'^b\sigma_L'^b) = \sum_{\sigma_R'^c\xi_R'^c} \Psi_2(\xi_L'^a\sigma_L'^a\sigma_R'^c\xi_R'^c)\overline{\Psi}_2(\xi_L'^b\sigma_L'^b\sigma_R'^c\xi_R'^c) \tag{129}$$

In the expressions for the right ones, the summation is performed over the left spins. The functions Ψ_j and $\overline{\Psi}_j$ are identical. That is why the density matrices in Eqs. (128) and (129) are symmetric. Here we should emphasize that the right blocks T_R are not mirror reflections of the left blocks T_L as they were in the standard approach [11, 12].

The choice of the density matrices according to Eqs. (128) and (129) corresponds to the requirement of the best approximation of density matrices at each row in further calculations. In this case the density matrices might be generally non-symmetric. In 1D calculations with non-symmetric Hamiltonian [82–88] the density matrices were also chosen as symmetric but different for each side of the Hamiltonian or the same, but taken as an average of the left and right ones. This choice is closer to the original White's approach where the goal is to find the best possible approximation for the left and right eigenvectors of the Hamiltonian (transfer matrix). For two-dimensional models with non-zero temperature the calculation is aimed to thermal averages of physical quanties, for which good values of density matrix are decisive. Thus, our approach with potentially non-symmetric transfer matrices we reckon as the best one.

By diagonalization of the left symmetric density matrix one obtains a matrix of orthonormal eigenvectors O_L:

$$Q_L(k|\xi\sigma)\rho_L^{(1)}(\xi\sigma|\xi'\sigma')O_L(\xi'\sigma'|\ell) = \omega_k\delta_{k\ell}, \tag{130}$$

where Q_L is transposed O_L and the eigenvalues ω_k satisfy the relation

$$\sum_k \omega_k = 1. \tag{131}$$

Analogously, we repeat this procedure for the density matrices $\rho_L^{(2)}$ and $\rho_R^{(2)}$ in order to obtain matrices Q'_L, O'_L, Q'_R, and O'_R. Discarding half eigenvectors in the matrices Q and O that correspond to the smallest eigenvalues ω_k, the matrices O and Q can be used as the reduction matrices in calculation of ${}^{i+1}T_L^{(1)new}$ via

$$\begin{aligned} {}^{i+1}T_L^{(1)new}({\xi'_L}^{new}{\sigma'_L}^{new}|\xi_L^{new}\sigma_L^{new}) = \sum_{\xi_L\xi'_L\sigma_L\sigma'_L} {}^iQ'_L({\xi'_L}^{new}|\xi'_L\sigma'_L) \\ \times {}^iT_L^{(1)}(\xi'_L\sigma'_L|\xi_L\sigma_L){}^iW_B^{(1)}(\sigma'_L{\sigma'_L}^{new}|\sigma_L\sigma_L^{new}){}^iO_L(\xi_L\sigma_L|\xi_L^{new}) \end{aligned} \tag{132}$$

Generalization for the right block is straightforward. The graphical representation of Eq. (132) is in Fig. 17.

Notice that at this step (Fig. 17) the reduction matrix O_L is obtained by diagonalization of the density matrix $\rho_L^{(1)}$ whereas the matrix Q'_L results from the diagonalization of

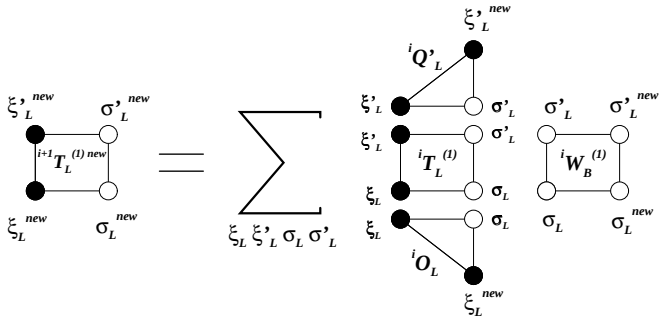

Fig. 17. Schematically written equation (132) which is used for computing the new left renormalized transfer matrix $T_L^{(1)new}$ from the old one $T_L^{(1)}$.

the density matrix $\rho_L^{(2)}$. Various physical quantities can be found knowing the functions Ψ_1, Ψ_2, $\overline{\Psi}_1$, and $\overline{\Psi}_2$, e. g. site magnetization used in further calculations

$$< \sigma_L >= \sum_{\xi_L \sigma_L \sigma_R \xi_R} \Psi_1(\xi_L \sigma_L \sigma_R \xi_R) \sigma_L \overline{\Psi}_1(\xi_L \sigma_L \sigma_R \xi_R). \tag{133}$$

The superblock transfer matrix needs to be slightly changed for the ANNNI model. The left and the right block transfer matrices have two spins more. The Boltzmann weight is defined on a plaquette of six spins. We have constructed the superblock transfer matrix T from the two block transfer matrices and the two overlapped Boltzmann weight (Fig. 15)

$$\begin{aligned} T(\xi_L \sigma_1 \sigma_2 \sigma_3 \sigma_4 \xi_R | \xi'_L \sigma'_1 \sigma'_2 \sigma'_3 \sigma'_4 \xi'_R) &= T_L(\xi_L \sigma_1 \sigma_2 | \xi'_L \sigma'_1 \sigma'_2) \\ &\times W_B^{(1)}(\sigma_1 \sigma_2 \sigma_3 | \sigma'_1 \sigma'_2 \sigma'_3) W_B^{(2)}(\sigma_2 \sigma_3 \sigma_4 | \sigma'_2 \sigma'_3 \sigma'_4) T_R(\sigma_3 \sigma_4 \xi_R | \sigma'_3 \sigma'_4 \xi'_R) \end{aligned} \tag{134}$$

5.1.4 Results

Properties of the ANNNI model on the triangular lattice were calculated recently [78] using the cluster transfer matrix method [51]. The results were consistent with numerous calculations of the ANNNI model on the square lattice. To compare performance of the DMRG method for incommensurate (IC) structures with other methods we calculated the phase diagram of the ANNNI model shown in Fig. 18. The resulting diagram is in accord with previous calculations [78] (Fig. 19). We have thus confirmed general opinion that there is no Lifshitz point on the ferro-para phase transition line.

The region of the IC structure comes out from the DMRG to be rather wide, however, we have used a low-order approximation ($N = 400$). The IC–phase region becomes narrower for higher-order approximations.

Not only the critical temperature and the free energy were calculated, also the critical exponents of Ising and ANNNI model. As expected, DMRG as an effective-field approximation yields classical values for all the critical exponents of the Ising model. Nevertheless, the critical exponent β of the domain wall density at C-IC phase transition

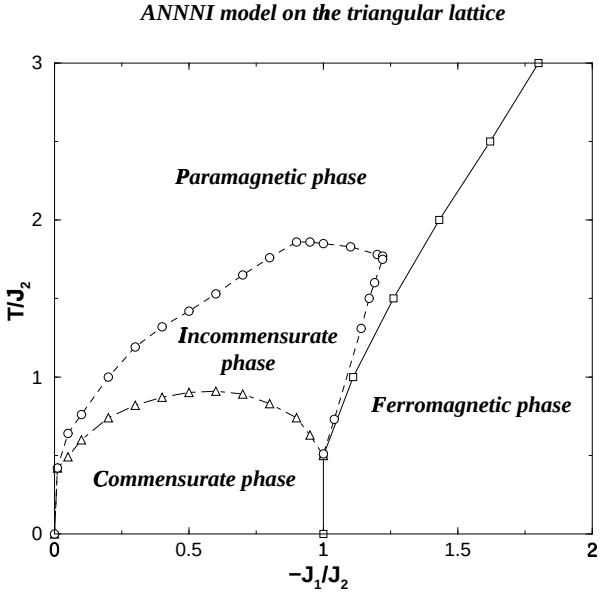

Fig. 18. The schematic phase diagram of the ANNNI model obtained by the DMRG method for relatively small superblock transfer-matrix size ($N = 400$). After the superblock transfer-matrix size is increased, the IC region becomes narrower and the para-IC phase transition line is shifted to lower temperatures.

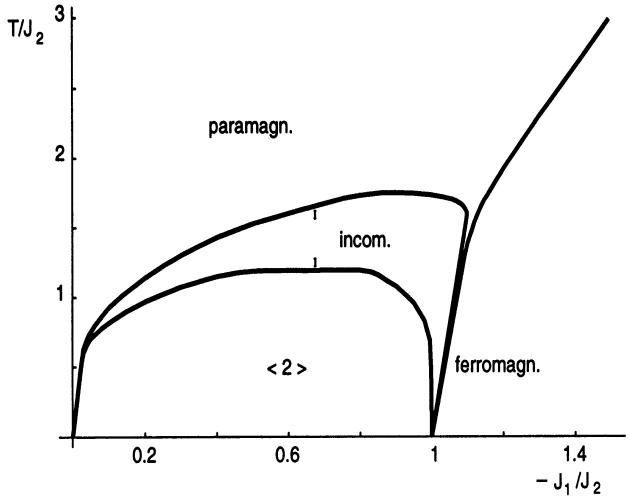

Fig. 19. The ANNNI phase diagram obtained from the cluster transfer matrix method.

obtained from our DMRG approach has a non-classical value $\beta = 0.502 \pm 0.003$ close to the Pokrovsky-Talapov value 1/2 [98], which is assumed to be exact (also see Sec. 2.3).

Standard mean-field approximations give a logarithmic singularity at the critical line [63]. We explain this by correct treatment of narrow-domain-wall meandering near the phase transition line by our large clusters. The resulting mean domain walls are straight, but due to the summation over all spin values of the clusters the wall meandering is involved in the calculation. The DMRG method reproduces well the results of the domain wall theory, though no domain walls are explicitly introduced within it.

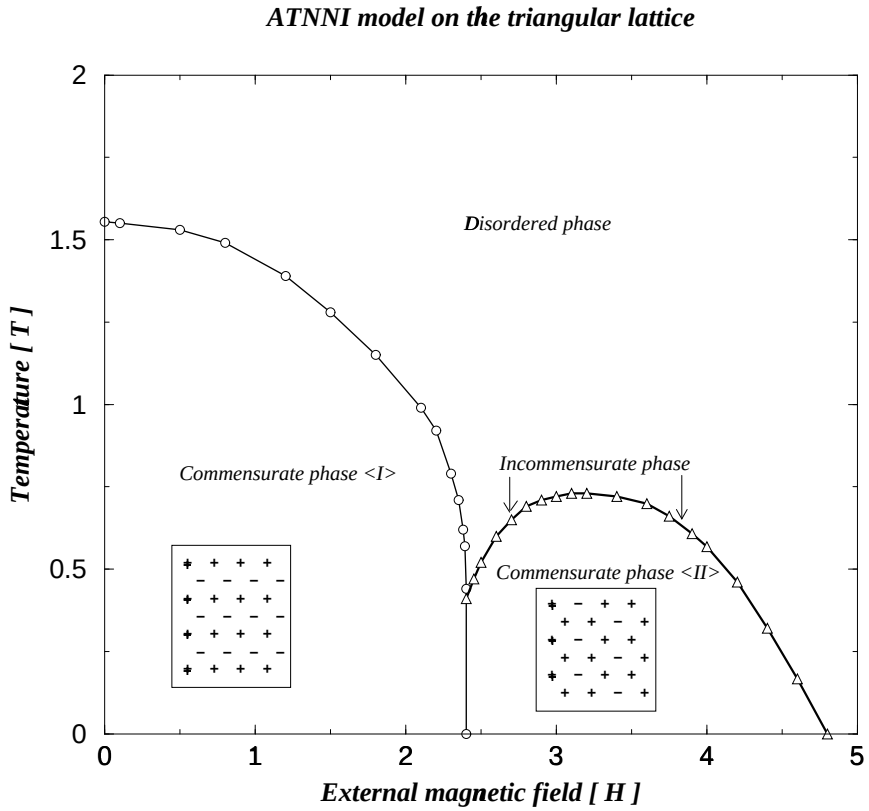

Fig. 20. The entire phase diagram of the ATNNI model is constructed by the DMRG technique. The incommensurate phase appears in narrow region (so narrow that it is depicted as a line only in the scale used) located between the disordered phase and the commensurate phase $\langle II\rangle$ for $2.4 < H < 4.8$. The ATNNI model is highly degenerated for $H = 2.4$.

The phase diagram of the ATNNI model (Fig. 20) consists of four regions (two different commensurate phases, the incommensurate and the disordered phases). Characteristic spin structures of both commensurate phases $\langle I\rangle$ and $\langle II\rangle$ of the triangular lattice (Fig. 12(a)) are shown in the insets of the same phase diagram.

The phases $\langle I\rangle$ and $\langle II\rangle$ consist of two and three different sublattices with constant magnetization, respectively. In the IC phase, the magnetization of each sublattice is periodically modulated and the sublattices become equivalent to each other. That is

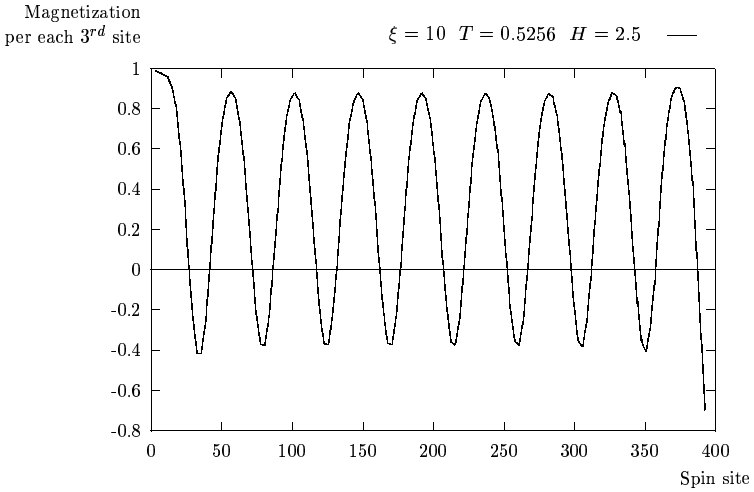

Fig. 21. Magnetization measured per each third spin site using Eq. (133) inside the incommensurate phase as a function of the spin position on the lattice for $H = 2.5$ and $T = 0.5256$.

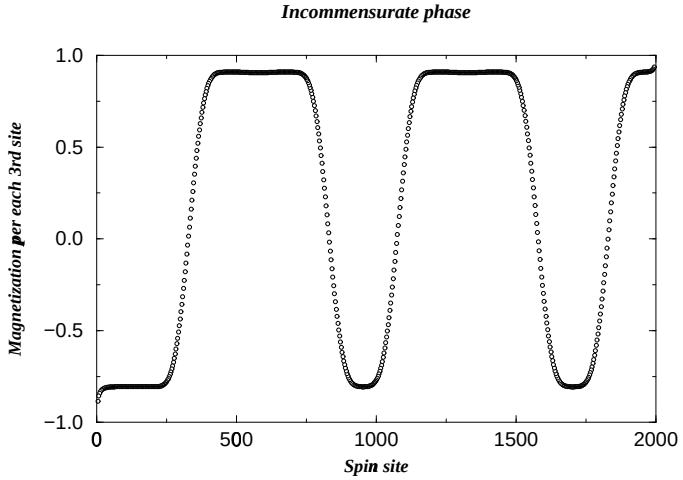

Fig. 22. Magnetization vs. position measured on the lattice inside the IC phase on each third site for $H = 3.02$ and $T = 0.73$.

why we plot only the magnetization of one of the sublattices (in Figs. 21 and 22).

The phase diagram was obtained from our calculation of magnetization. The DMRG method with spontaneous symmetry breaking yields directly the space modulation of magnetization, which enables us to identify the phase unambiguously. In practical calculations, it is enough to observe the behavior of the largest eigenvalues of the superblock

matrix. The period of their spatial modulation is the same as the period of the structure.

The incommensurate structure is floating, i.e. it is not fixed to the underlying lattice. In our calculation with spontaneous symmetry breaking, one of the infinitely many positions of the incommensurate wave is chosen at the beginning of the calculation and it remains fixed during whole further calculation.

We have found the incommensurate structure practically along whole border between the commensurate $\langle II \rangle$ phase and the disordered phase. However, in two regions the calculations were inconclusive:

(i) The high degeneracy of the ground state at $H = 2.4$ and $T < 0.4$ [80] has also caused highly degenerate largest eigenvalues of the superblock transfer matrix, and our method did not converge to any periodic structure for magnetic fields between 2.40 and 2.41 at low temperatures.

(ii) Another region is located at the high-magnetic-field end $H \approx 4.8$ and $T < 0.1$ of the phase diagram. Here, the incommensurate phase is extremely narrow as seen in Fig. 23.

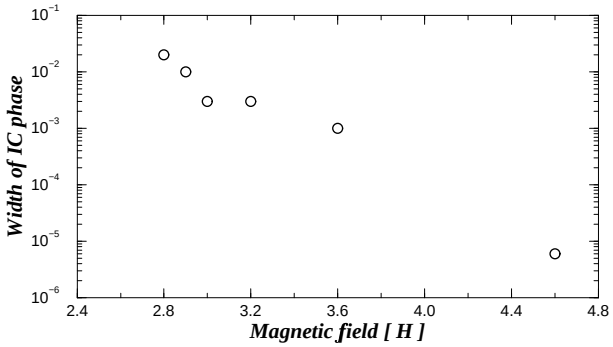

Fig. 23. The width of the incommensurate phase measured in units of temperature vs. external magnetic field H. With increasing field H the distance between the disordered and commensurate phases $\langle II \rangle$ decreases.

Therefore, the ATNNI model exhibits a very large period shown in Fig. 24. Moreover, due to the proximity of the second-order phase transition line, the convergence is very slow. We have started the calculations with the Infinite System Method (ISM) where the superblock transfer matrix is constructed from left and right transfer matrices of the *previous iteration step*. After a large number of iterations performed, we obtained the final result for commensurate structures including the disordered phase. For the incommensurate structure it is necessary to perform afterwards some sweeps of the FSM in order to improve results that smooth the magnetization profile of the spin wave. The IC structure appears already after the application of the ISM but the correct shape of the magnetization is acquired after the FSM, only.

The shape of period of the IC structure changes with magnetic field H and temperature T. The period of the IC structure increases with the increasing magnetic field and decreasing temperature. At low temperatures (close to the $\langle II \rangle$–IC phase transition line) the structure consists of wide domains of the phase $\langle II \rangle$ separated by narrow domain

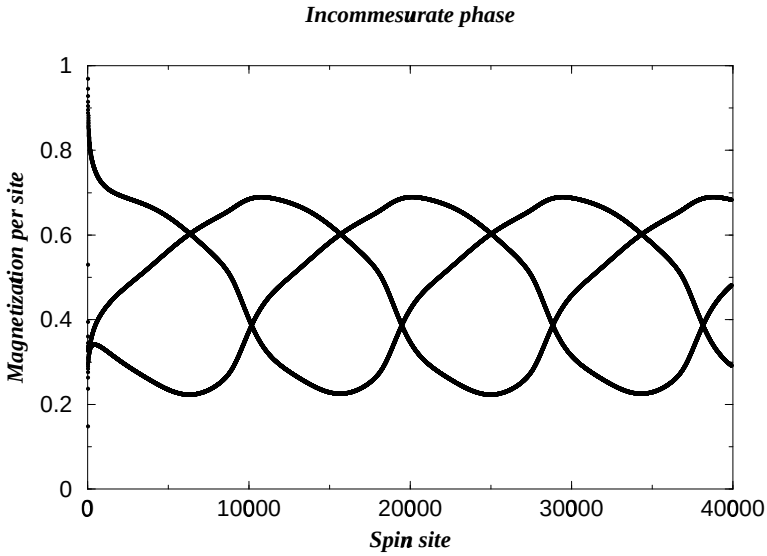

Fig. 24. The IC phase (obtained for a high magnetic field $H = 4.6$) was found within temperatures $0.166158 < T < 0.166162$. The magnetization is measured on each site. All three spin waves are plotted.

walls. At higher temperatures near to disorder–IC transition, the domain walls become wider, the period shorter and the structure acquires a sinusoidal-like shape.

Both phase transitions are continuous. Inverse period of the structure and wave amplitude tend to zero at the $\langle II \rangle$–IC and the disorder–IC phase transition lines, respectively. It should be noted that the notions of low and high temperatures must be understood within an extremely narrow temperature interval where the IC phase exists.

The effect of magnetic field on the IC phase is similar to the temperature effects but of opposite direction. Low magnetic field (near 2.4) enhances the high temperature effects, while the high magnetic field (near 4.8) the low temperature ones.

For the magnetic field H close to the value of 4.8, the period is very long, that is why we were able to perform the ISM only using an incorrect magnetization shape which would need further improvements within the FSM (Fig. 24).

Our calculations converged to the stable periodic solution at the most of the part of the commensurate $\langle II \rangle$-disordered phase borders. Here the IC phase has been found everywhere. This fact leads us to a conjecture (in contrary to [80]) that the Lifshitz point does not exists in the ATNNI model.

We used the DMRG method to investigate incommensurate structures in 2D classical model for the first time. We found that it reproduces well the previous results for the ANNNI model. In the case of the ATNNI model it has shown much better performance in the regions where the previous approaches (the cluster transfer matrix method [51, 99] near $H = 2.4$ and the free-fermion approximation [80] for $H > 3$) failed.

On the basis of scaling properties of Monte Carlo calculations and the exact diag-

onalization of finite strips, the authors [80] concluded that at $H \cong 3$ the IC structure disappears and at higher fields H the direct phase transition between commensurate $\langle II \rangle$ and disordered phases is continuous.

We have observed the IC phase to exists everywhere between the disordered and commensurate $\langle II \rangle$ phases, i.e. we have not found any Lifshitz point, i. e., the point where the three phases, namely the commensurate, the incommensurate and the disordered one meet. Nevertheless, measured widths of the IC phase are extremely small at large H and they exponentially tend to zero at $H = 4.8$. As the width of the IC phase gets narrower for the high-order approximations we cannot completely exclude the scenario of Domany and Schaub [80].

Our belief in correct description of incommensurate phases by the DMRG technique is supported by the reproduction of the ANNNI phase diagram with generally expected features.

5.2 Periodic boundary conditions in 2D models using DMRG

It was shown that the DRMG method yields very accurate estimations of ground state energy of finite quantum chains and free energy of classical strips of finite width with open boundary conditions. We have developed the DMRG method with periodic boundary conditions for strips of classical spins and shown that, similarly as for quantum chains, it yields these quantities with much lower degree of accuracy. Nevertheless, the DMRG method is mostly used for prediction of physical quantities and critical properties of infinite systems in connection with finite size scaling or extrapolation of the results from finite-size systems to infinite ones. The objective is to study the DMRG and exact methods with two different boundary conditions for finite strips of various widths and compare their results with known exact results for infinite 2D system. It is shown that while for the exact diagonalization of finite-strip transfer matrices scaling properties of the system improve, for DMRG approach there exists an optimum width for each degree of approximation. The developed approach is tested on 2D Ising model.

5.2.1 DMRG with open boundary conditions

The transfer matrix approach is a powerful method for exact numerical calculation of thermodynamic properties of lattice spin models defined on finite-width strips. If the width of the strip is too large and the capacity of the computer is exceeded, the DMRG method is found to be useful for an effective reduction of the transfer matrix size. It can be used for calculation of global quantities such as free energy as well as of a spatial dependence across the strip of local quantities, e.g. spin correlation functions.

The properties of an infinite strip of finite width L are given by the solution of 'left' eigenvectors and corresponding eigenvalues of the transfer matrix equation

$$\sum_{\{\sigma\}} \Psi_l\left(\{\sigma\}\right) T\left(\{\sigma\}|\{\sigma'\}\right) = \lambda \Psi_l\left(\{\sigma'\}\right), \tag{135}$$

where $\{\sigma\}$ is a set of L spins $\{\sigma_1, \sigma_2, \ldots, \sigma_L\}$ defined on a row and $\{\sigma'\}$ is a set of L spins on the adjacent row. The transfer matrix is a product of the Boltzmann weights

given by the lattice Hamiltonian. For non-symmetric transfer matrices besides the left eigenvectors Ψ_l^i, the right eigenvectors Ψ_r^i should be also calculated.

Reducing the size of the transfer matrix the standard DMRG technique proceeds in two regimes:

Regime 1. In the process of iterations, the infinite system method (ISM) pushes both ends of the transfer matrix further so that each step of the ISM enlarges the lattice size by two. The transfer matrix (superblock) is constructed from three blocks: left T_l and right T_r transfer matrices (blocks) and the Boltzmann weight W_B

$$T_{[2j+2]} = T_l^{(j)} W_B T_r^{(j)}, \tag{136}$$

where the subscript on the left hand side denotes the number of sites in one row of the whole superblock T at the jth step of iteration. The Boltzmann weight is usually a function of several spins interacting together, e. g. the Boltzmann weight for the Ising model with nearest-neighbor interactions has the form

$$W_B(\sigma_1\sigma_2|\sigma_1'\sigma_2') = \exp\left\{-\frac{J}{k_BT}(\sigma_1\sigma_2 + \sigma_1'\sigma_2' + \sigma_1\sigma_1' + \sigma_2\sigma_2')\right\}. \tag{137}$$

In the first step of the ISM (for details, see [12, 32]) $T_l^{(1)} = T_r^{(1)} = W_B$. The whole procedure is of $L/2 - 1$ steps

$$T_l^{(1)} W_B T_r^{(1)} \to T_l^{(2)} W_B T_r^{(2)} \to \cdots \to T_l^{(L/2-1)} W_B T_r^{(L/2-1)}. \tag{138}$$

and stops when the desired strip width of L sites is reached.

Several first steps of the iteration scheme in Eq. (138) are exact, but if the superblock matrix T becomes too large, a reduction procedure to keep the size of superblock constant should be introduced.

The first step of Eq. (138) introduces open boundary conditions at the strip boundaries. If the temperature of the system is lower than the critical one and the strip width is wide enough, the symmetry of the system is spontaneously broken (order parameter becomes non-zero), and after reaching the fixed point of the iteration procedure, the system does not depend on the boundary conditions any more. The calculations with periodic boundary conditions described in the next Section give the same result in this regime as with the free ones.

Regime 2. The finite system method (FSM) improves numerical accuracy of ISM result by left and right moves (*sweeps*) according to the following prescription:

$$T_l^{(L/2-1)} W_B T_r^{(L/2-1)} \to T_l^{(L/2)} W_B T_r^{(L/2-2)} \to \cdots \to T_l^{(L-3)} W_B T_r^{(1)}, \tag{139}$$

$$T_l^{(L-3)} W_B T_r^{(1)} \to T_l^{(L-2)} W_B T_r^{(2)} \to \cdots \to T_l^{(L/2-1)} W_B T_r^{(L/2-1)}. \tag{140}$$

In the right sweep of Eq. (140) the left blocks T_l are calculated in the previous step of the sweep and the right blocks T_r are taken from the previous left sweep (in the first right sweep from ISM); similarly for the left sweep.

The values of local thermodynamic quantities given by particular superblocks in the final sweep (after the steady state is reached) are spatially dependent. The values given

by the superblock in the middle of the strip $T_l^{(L/2-1)} W_B T_r^{(L/2-1)}$ are the closest to the bulk ones. In this sense, the best transfer matrix eigenvalues as well as eigenvectors are those of the above-mentioned central superblock. The two largest eigenvalues are used for further finite-size scaling or extrapolation treatment.

5.2.2 DMRG with periodic boundary conditions

The translational invariance of the infinite lattice is preserved in finite strips with periodic boundary conditions when strip boundaries are connected with bulk intersite interactions. In this case the strip forms an infinitely long cylinder. If the radius of the cylinder is small enough, the model can be easily solved by exact numerical diagonalization methods.

In DMRG language, imposing periodic boundary conditions means that we have to introduce properly the connection of both ends of the superblock transfer matrix T. Thus, in distinction to the open-boundary case the superblock is constructed from two Boltzmann weights connecting two blocks at both ends (see Fig. 25, the rightmost diagram).

$$T_{[2j+4]}(\sigma_1\xi_l\sigma_{j+4}\sigma_{j+3}\xi_r\sigma_2|\sigma'_1\xi'_l\sigma'_{j+4}\sigma'_{j+3}\xi'_r\sigma'_2) = T_l^{(j)}(\sigma_1\xi_l\sigma_{j+4}|\sigma'_1\xi'_l\sigma'_{j+4}) \times W_B(\sigma_{j+4}\sigma_{j+3}|\sigma'_{j+4}\sigma'_{j+3}) T_r^{(j)}(\sigma_{j+3}\xi_r\sigma_2|\sigma'_{j+3}\xi'_r\sigma'_2) W_B(\sigma_2\sigma_1|\sigma'_2\sigma'_1), \quad (141)$$

where the block spin variable $\xi = \{1, 2, \ldots, m\}$, and the primed variables are denoted by filled circles and ovals, respectively, in Fig. 25.

In the first few steps the lattice is enlarged to the desired size; no degrees-of-freedom reduction is performed and the superblock transfer matrix remains equivalent to the exact one. As depicted in Fig. 25, the ISM starts with $T^{(6)} = T_l^{(1)} W_B T_r^{(1)} W_B$ defined on twelve sites where $T_l^{(1)} = T_r^{(1)} = W_B W_B$. One Boltzmann weight, i.e. four new sites are added in each of further steps.

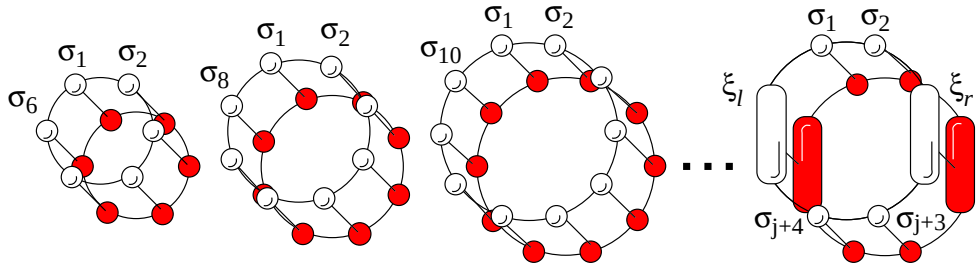

Fig. 25. The first j steps of the ISM for the strip with the periodic boundary conditions.

If $2^j > m$, the number of degrees of freedom should be reduced at each jth step to keep the order of the superblock matrix constant and equal to $2^4 \cdot m^2$.

Summation over the eigenequation of Eq. (135) of the transfer matrix in Eq. (141) can be performed in two steps

$$\Phi(\sigma_1\xi_l\sigma_{j+4}\sigma_{j+3}\sigma'_{j+3}\xi'_r\sigma'_2\sigma'_1) = \sum_{\xi_r\sigma_2} T_r(\sigma_{j+3}\xi_r\sigma_2|\sigma'_{j+3}\xi'_r\sigma'_2) W_B(\sigma_2\sigma_1|\sigma'_2\sigma'_1) \times \Psi(\sigma_1\xi_l\sigma_{j+4}\sigma_{j+3}\xi_r\sigma_2) \quad (142)$$

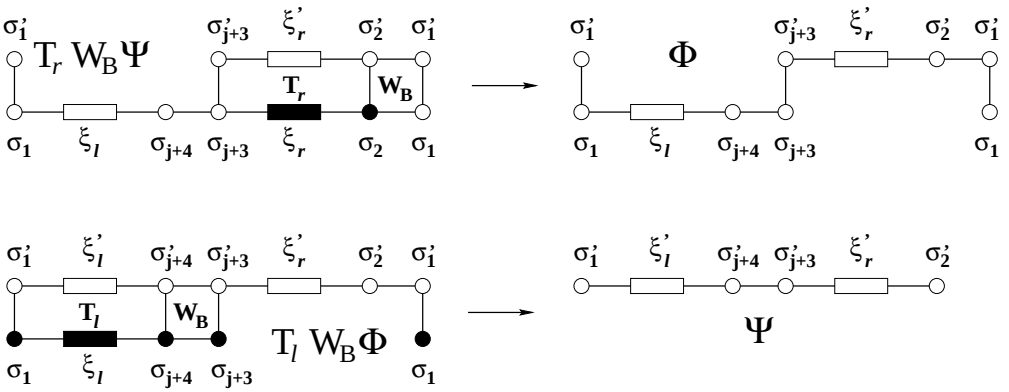

Fig. 26. Graphical representation of Eqs. (142) and (143). The variables represented by filled circles and rectangles are summed over. The spins σ_1 and σ_1' at both ends of the superblock must be identified due to the periodic boundary conditions.

$$\Psi(\sigma_1'\xi_l'\sigma_{j+4}'\sigma_{j+3}'\xi_r'\sigma_2') = \sum_{\substack{\sigma_1\xi_l \\ \sigma_{j+4}\sigma_{j+3}}} T_l(\sigma_1\xi_l\sigma_{j+4}|\sigma_1'\xi_l'\sigma_{j+4}') \times W_B(\sigma_{j+4}\sigma_{j+3}|\sigma_{j+4}'\sigma_{j+3}')\Phi(\sigma_1\xi_l\sigma_{j+4}\sigma_{j+3}\sigma_{j+3}'\xi_r'\sigma_2'\sigma_1'). \quad (143)$$

The steps are also depicted graphically in Fig. 26.

This procedure uses the left and right transfer matrix blocks to calculate properly the left and right eigenvectors Ψ_l and Ψ_r of the whole superblock for the periodic boundary conditions, respectively. Once we have the Ψ_l and Ψ_r, the left and right density matrices can be constructed

$$\rho_l(\xi_l\sigma_{j+4}|\xi_l'\sigma_{j+4}') = \sum_{\sigma_1\sigma_{j+3}\xi_r\sigma_2} \Psi_l(\sigma_1\xi_l\sigma_{j+4}\sigma_{j+3}\xi_r\sigma_2)\Psi_r(\sigma_1\xi_l'\sigma_{j+4}'\sigma_{j+3}\xi_r\sigma_2) \quad (144)$$

$$\rho_r(\sigma_{j+3}\xi_r|\sigma_{j+3}'\xi_r') = \sum_{\sigma_1\xi_l\sigma_{j+4}\sigma_2} \Psi_l(\sigma_1\xi_l\sigma_{j+4}\sigma_{j+3}\xi_r\sigma_2)\Psi_r(\sigma_1\xi_l\sigma_{j+4}\sigma_{j+3}'\xi_r'\sigma_2), \quad (145)$$

and by the complete diagonalization

$$O_l(\xi_l^{new}|\xi_l\sigma_{j+4})\rho_l(\xi_l\sigma_{j+4}|\xi_l'\sigma_{j+4}')Q_l(\xi_l'\sigma_{j+4}'|\xi_l'^{\,new}) = \omega_i\delta_{ij} \quad (146)$$

we obtain the sets of left and right eigenvectors stored in O_l and Q_l matrices, respectively. Analogously, for the ρ_r, we obtain matrices O_r and Q_r. The indices i, j ($i, j = 1, 2, \ldots, 2m$) run over all states of m-state multi-spin variable ξ and two-state variable σ. For the last steps of ISM and all FSM steps, half of the eigenvectors (corresponding to their lowest eigenvalues) is discarded from the matrices O and Q, and the information on the system carried by the density matrix is reduced. However, remaining eigenvectors (if m is large enough) usually describe the system with a sufficient accuracy. The truncation error ε defined as

$$\varepsilon = \sum_{\{\text{discarded}\}} \omega \quad (147)$$

is then very small ($0 \leq \varepsilon \ll 1$). In Eq. (147), $\sum_{\{all\}} \omega = 1$, as the eigenvectors are assumed to be normalized. The matrices O and Q enter the linear transformation as projectors mapping two blocks $T_l W_B$ onto one block T_l through the following procedure

$$T_l^{(j+1)}(\sigma_1 \xi_l^{new} \sigma_{j+5} | \sigma'_1 \xi'^{\,new}_l \sigma'_{j+5}) = \sum_{\substack{\xi'_l \sigma'_{j+4} \\ \xi_l \sigma_{j+4}}} O_l(\xi_l^{new} | \xi_l \sigma_{j+4})$$

$$\times T_l^{(j)}(\sigma_1 \xi_l \sigma_{j+4} | \sigma'_1 \xi'_l \sigma'_{j+4}) W_B(\sigma_{j+4}\sigma_{j+5} | \sigma'_{j+4}\sigma'_{j+5}) Q_l(\xi'_l \sigma'_{j+4} | \xi'^{\,new}_l). \quad (148)$$

Application to the right block T_r is straightforward. As it is seen, we calculate the blocks T_l and T_r separately not using the standard mirror-reflection of T_l to T_r. This procedure is necessary when dealing with anisotropic and/or inhomogeneous systems.

The calculated new blocks $T_l^{(j+1)}$ and $T_r^{(j+1)}$ are used in the next step of the ISM for construction of the new superblock

$$T_{[2j+6]} = T_l^{(j+1)} W_B T_r^{(j+1)} W_B. \quad (149)$$

Within the FSM, e.g., for a sweep to the right only the left blocks are calculated for a sweep to the right and $T_r^{(L/2-k)}$ is taken from the previous left sweep

$$T_{[L]} = T_l^{(L/2-3+k)} W_B T_r^{(L/2-1-k)} W_B. \quad (150)$$

The variable k (indexing the steps within a sweep) runs over the values $(-k_0, -k_0 + 1, \ldots, k_0 - 1, k_0)$, where $2^{k_0} \leq 2^{L/2-2} - m$. In the process of sweeping, one of the Boltzmann weights is fixed (the upper one in Fig. 25) and the second one changes its position within the interval of $2k_0$ lattice sites. The local physical quantities are calculated at the lattice sites of the fixed Boltzmann weight. Due to the rotational invariance of the problem they are valid for all the rows of the periodic lattice.

5.2.3 Results for 2D Ising and q-state Potts models

It is well known that the DMRG algorithm describes better a strip with open boundary conditions than that with the periodic boundary conditions [12]. It is because the precision of the largest eigenvalue of the superblock matrix is proportional to m for open boundary conditions while for periodic boundary conditions it is proportional only as $\sqrt{m}$.

In case of relatively narrow strips, the DMRG calculations are consistent with the exact calculations: they yield zero-order parameter and reproduce well the two largest eigenvalues of the transfer matrix of the system. Comparison of the exact and approximate values for Ising and ATNNI models on a semi-infinite strip of width $L = 16$ with open boundary conditions for various approximations are given in Tables I and II, respectively. Analogously, results of calculations for the Ising and ATNNI models with the periodic boundary conditions are given in Tables III and IV, respectively.

We see that the first two eigenvalues of the superblock transfer matrices in the DMRG method are very close to the exact values despite small sizes of superblock matrices ($N \times N$) that are much less than the size of the exact T-matrix (65536×65536) defined on 16 sites. The dimension of the transfer matrix N depends on the size of the block-spin

variable [32]. The calculations for ATNNI model were performed at a moderate magnetic field $H = 2$. At higher magnetic fields we frequently encountered problems with complex conjugated pairs of two largest transfer matrix eigenvalues in the DMRG calculations.

However, if we are not interested in the largest eigenvalue of a finite-strip transfer matrix but in the estimation of the free energy of the whole 2D lattice (per spin), it is more effective to use a strip with periodic boundary conditions than that with open boundaries, as demonstrated in Table V. The results with $m = 25$ practically exactly reproduce the exact values for $L = 16$. The estimation of the free energy for 2D models performed by DMRG can be improved by increasing the width of the strip. For given m the best results are obtained by ISM for $L \to \infty$, but in this case, for $T = 2.1$ (i.e. below the critical temperature), the symmetry of the system is spontaneously broken. The free energy for both PBC and OBC is the same in the $L \to \infty$ limit, but the value given in Table V was actually calculated for PBC, as it converged to $f_{\mathrm{ISM}}^{\mathrm{DMRG}}$ already for $L = 50$ while OBC needed $L > 10^4$. Exact free energy per site $f_{\mathrm{Onsager}}^{(\mathrm{exact})}$ was taken from [60].

The critical temperature and the properties of the infinite 2D system near the critical temperature should be derived from finite-size scaling ideas (as the finite-width strip is at criticality for $T = 0$ only).

For calculation of the critical temperature, the phenomenological renormalization approach of Nightingale [95] has been used. Here the scaling properties of the correlation length, found as a logarithm of the ratio of two largest eigenvalues of the exact or superblock matrix are exploited. The product of the inverse correlation length K_N and the strip width L should not depend on L at critical temperature $T_{\mathrm{C}}^*(L)$

$$\frac{LK_L}{(L+2)K_{L+2}} = 1. \tag{151}$$

The accuracy of the approximate critical temperature improves with size of the strip in the case of exact diagonalization. For DMRG calculations this statement is no longer valid, as for very large L the symmetry of the system spontaneously breaks, and the

Table I. The largest eigenvalue λ_1 and the second largest eigenvalue λ_2 of the transfer matrices calculated with the DMRG technique for the Ising model with open boundary conditions. The dimension of the transfer matrix N depends on the size of the block-spin variable [32]. The last line of the table contains the eigenvalues of the transfer matrix obtained by the exact diagonalization method. DMRG is much faster than the exact diagonalization method.

Ising model with open boundary conditions					
m	N	Ordered phase $T = 2.1$		Disordered phase $T = 2.4$	
		λ_1	λ_2	λ_1	λ_2
5	400	4.11311663×10^6	3.9310449×10^6	1.2954416770×10^6	1.0620492×10^6
10	1600	4.13211349×10^6	3.9895804×10^6	1.2965251439×10^6	1.0906563×10^6
15	3600	4.13211552×10^6	3.9896518×10^6	1.2965253478×10^6	1.0910038×10^6
20	6400	4.13214516×10^6	3.9898654×10^6	1.2965262430×10^6	1.0913165×10^6
25	10000	4.13214516×10^6	3.9898655×10^6	1.2965262430×10^6	1.0913166×10^6
–	65536	4.13214526×10^6	3.9898681×10^6	1.2965262432×10^6	1.0913187×10^6

Table II. The two largest eigenvalues λ_1 and λ_2 of the transfer matrix for the ATNNI model are calculated with the DMRG technique for open boundary conditions. Data obtained by the exact diagonalization method are shown in the last line.

ATNNI model with open boundary conditions					
m	N	Commensurate phase $T = 0.9,\ H = 2.0$		Disordered phase $T = 1.2,\ H = 2.0$	
		λ_1	λ_2	λ_1	λ_2
5	400	8.50337×10^{11}	2.0014×10^{11}	2.97329×10^{9}	2.0156×10^{9}
10	1600	9.47434×10^{11}	7.6805×10^{11}	3.02362×10^{9}	1.5450×10^{9}
15	3600	9.45896×10^{11}	7.6335×10^{11}	3.02193×10^{9}	1.5078×10^{9}
20	6400	9.44951×10^{11}	7.5767×10^{11}	3.02096×10^{9}	1.4635×10^{9}
25	10000	9.44951×10^{11}	7.5761×10^{11}	3.02096×10^{9}	1.4606×10^{9}
–	65536	9.44948×10^{11}	7.5749×10^{11}	3.02094×10^{9}	1.4531×10^{9}

phenomenological renormalization is not applicable any more. Thus an optimum value of the strip width $L^{\rm opt}$ exists for given order of approximation m. This can be estimated from the following considerations: For exact diagonalization or DMRG calculations with m close to $2^{L/2-2}$, the difference of the approximate critical temperature from the exact critical temperature $T_{\rm C}^{\rm (exact)} = 2\ln^{-1}(1+\sqrt{2})$ [1] scales with the width of the strip as [101]:

$$\frac{T_{\rm C}^{*}(L) - T_{\rm C}^{\rm (exact)}}{T_{\rm C}^{\rm (exact)}} \sim L^{-1/\nu}, \tag{152}$$

i.e. the ratio

$$R \equiv \frac{\frac{\rm d}{{\rm d}L}T_{\rm C}^{*}(L)}{\frac{{\rm d}^2}{{\rm d}L^2}T_{\rm C}^{*}(L)} = \frac{\nu}{\nu+1}L \sim L. \tag{153}$$

The optimum width $L^{\rm opt}$ should be less than $L_{\rm C}$, the value for which the ratio of the derivatives $R(L_{\rm C})$ (153) substantially deviates from the originally linear behavior. In our calculations we have considered the DMRG results to be incorrect for $R = 0$ or ∞. In

Table III. The same as shown in Table 1 but for the case of periodic boundary conditions.

Ising model with periodic boundary conditions					
m	N	Ordered phase $T = 2.1$		Disordered phase $T = 2.4$	
		λ_1	λ_2	λ_1	λ_2
5	400	7.00331679×10^{6}	6.9180364×10^{6}	1.76379494×10^{6}	1.5477034×10^{6}
10	1600	7.03990343×10^{6}	6.9742292×10^{6}	1.76702461×10^{6}	1.5769844×10^{6}
15	3600	7.03991836×10^{6}	6.9742595×10^{6}	1.76704324×10^{6}	1.5771406×10^{6}
20	6400	7.04001144×10^{6}	6.9743133×10^{6}	1.76710592×10^{6}	1.5771736×10^{6}
25	10000	7.04001146×10^{6}	6.9743135×10^{6}	1.76710593×10^{6}	1.5771740×10^{6}
–	65536	7.04001165×10^{6}	6.9743146×10^{6}	1.76710598×10^{6}	1.5771799×10^{6}

Table IV. The same description as shown in Table 2 for the ATNNI model but we imposed periodic boundary conditions.

ATNNI model with periodic boundary conditions					
m	N	Commensurate phase $T = 0.9$, $H = 2.0$		Disordered phase $T = 1.2$, $H = 2.0$	
		λ_1	λ_2	λ_1	λ_2
5	400	3.8724×10^{12}	2.4898×10^{11}	5.8940×10^{9}	1.0267×10^{9}
10	1600	4.0818×10^{12}	3.7378×10^{12}	6.9274×10^{9}	4.5860×10^{9}
15	3600	4.0503×10^{12}	3.7013×10^{12}	6.9235×10^{9}	4.5697×10^{9}
20	6400	4.0560×10^{12}	3.7033×10^{12}	6.9330×10^{9}	4.5120×10^{9}
25	10000	4.0556×10^{12}	3.6996×10^{12}	6.9328×10^{9}	4.4892×10^{9}
–	65536	4.0530×10^{12}	3.6884×10^{12}	6.9312×10^{9}	4.4368×10^{9}

Table V. Free energy per site f_{ISM} for the Ising model calculated with the standard DMRG method only with the ISM is compared with the free energy per site calculated by the modified DMRG algorithm as well as by the exact diagonalization method (EDM). N is the order of either the superblock of DMRG or the exact transfer matrix in EDM.

Free energy per site	**T=2.1**	**T=2.4**	**N**	**m**	**L**
$f_{\mathrm{open}}^{\mathrm{DMRG}}$	1.999502815	2.111279868776	10000	25	16
$f_{\mathrm{open}}^{\mathrm{EDM}}$	1.999502828	2.111279868799	65536	—	16
$f_{\mathrm{periodic}}^{\mathrm{DMRG}}$	2.069434546	2.157728055	10000	25	16
$f_{\mathrm{periodic}}^{\mathrm{EDM}}$	2.069434550	2.157728059	65536	—	16
$f_{\mathrm{ISM}}^{\mathrm{DMRG}}$	2.0688412	2.15660	10000	25	∞
$f_{\mathrm{Onsager}}^{(\mathrm{exact})}$	2.0688415	2.15661	———	—	—

the case of $R = 0$, the precise value of L^{opt} is not much important as the first derivative or change of $T_{\mathrm{C}}^{*}(L)$ is very small. Near $R = \infty$, a sharp drop of the second derivative of $T_{\mathrm{C}}^{*}(L)$ to zero is required; indeed, the change of the distance from the line $\frac{\nu}{\nu+1}L$ by more than one order of magnitude takes place within one step of strip-width enlargement.

In Fig. 27 plots of strip-width-dependent critical temperatures $T_{\mathrm{C}}^{*}(L)$ for two different boundary conditions and various block sizes m are given. The estimates of the exact critical temperature for periodic and open boundary conditions were found as the values of $T_{\mathrm{C}}^{*}(L-2)$ if the first or second derivative of $T_{\mathrm{C}}^{*}(L)$ changed their signs with respect to the value in the previous step. The curves for PBC cross the exact value of $T_{\mathrm{C}}^{(\mathrm{exact})}$. The maximum of the OBC curve is far from $T_{\mathrm{C}}^{(\mathrm{exact})}$ and T_{C}^{*} approaches the exact value very slowly with increasing L.

The accuracy of the results for periodic boundary conditions (Fig. 28) is very high already at small values of m and it exceeds by an order the critical temperature estimation for maximum computer-accessible m when using open boundary conditions. The critical temperature for not extremely large $m = 80$ is given to seven digits. As the width of

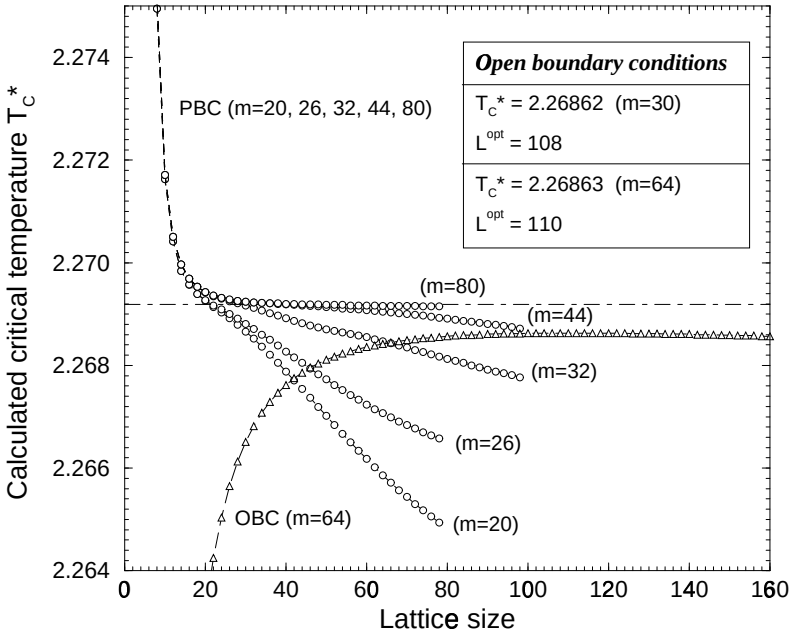

Fig. 27. Critical temperatures $T_{\rm C}^*$ for the Ising model as functions of lattice size L for various sizes of multi-spin variables m from DMRG and finite-size scaling. The results for open boundary conditions (OBC) are plotted as triangles while the results for the periodic boundary conditions (PBC) are plotted as circles. The exact critical temperature is drawn by the dot-dashed line. The OBC plot for $m = 30$ is indistinguishable from the curve for $m = 64$ in this figure.

the strip can be increased only in discrete steps, the accuracy of the critical temperature determination should be taken as large as a single step change of $T_{\rm C}^*(L)$. The accuracy estimates together with deviations of our results from the exact critical temperature are given in Table VI.

It should be noted that only ISM was performed in the calculations of $T_{\rm C}^*(L)$ shown in Figs. 27 and 28. The calculations within the FSM has also been done near the $L^{\rm opt}$, but only slight improvements of critical temperature were obtained. In calculation of the thermal and the magnetic critical exponents [95], a similar accuracy has been reached as that for $T_{\rm C}^*$. The obtained thermal critical exponent $y_{\rm T} = 1.00000088$ and magnetic exponent $y_{\rm H} = 1.8750019$ are in good agreement with the exact values $y_{\rm T} = 1.0$ and

Table VI. Changes of $T_{\rm C}^*(L)$ per one step of strip-width enlargement as well as the differences between our results and the exact critical temperature $T_{\rm C}^{(\rm exact)}$ for various parameters m.

m	**20**	**26**	**32**	**44**	**60**	**80**
$\Delta_{\rm L} T_{\rm C}^*(L) \times 10^7$	560	434	166	46	33	15
$\left(T_{\rm C}^*(L^{\rm opt}) - T_{\rm C}^{(\rm exact)}\right) \times 10^7$	707	121	117	13	7	2

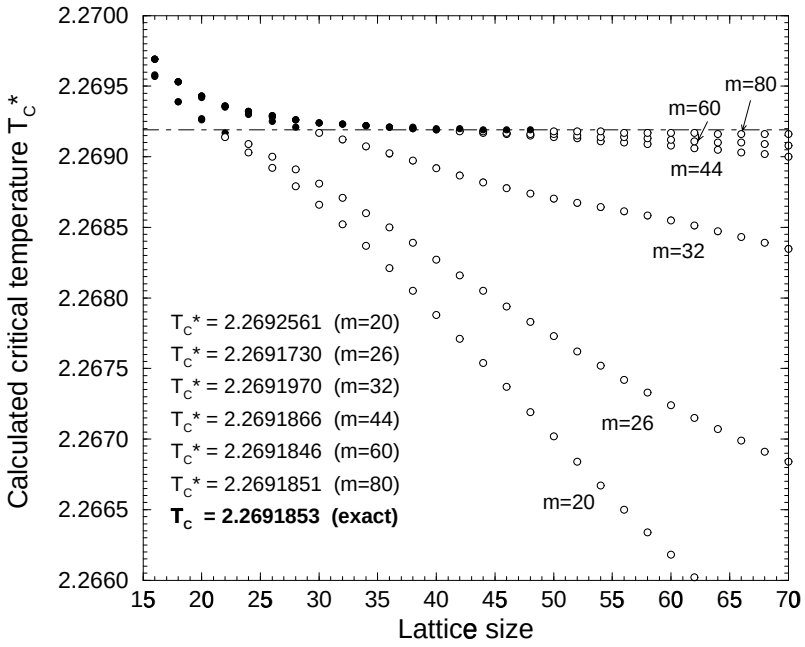

Fig. 28. Critical temperatures $T_{\rm C}^*$ of the Ising model vs. lattice size L for different m when the periodic boundary conditions (PBC) are imposed. Filled circles represent the accepted data whereas the open circles are taken as incorrect due to the violation of the condition (153). The critical temperature estimations in the inset are given by the rightmost filled circles for respective m.

$y_{\rm H} = 1.875$ [1], respectively. Both critical exponents were calculated for $m = 80$. The accuracy of both critical exponents is highly sensitive to precise determination of $T_{\rm C}^*$, and the precise value of critical temperature (reached for $m = 80$) was necessary to get the presented values of the critical exponents.

In order to check the efficiency of our method we have made additional calculations for the q-state Potts model for $q = 2, 3$, and 4. We have calculated thermal as well as magnetic critical exponents, see Table VII.

Because of larger number of spin components in the $q > 2$ Potts model and logarithmic corrections to scaling at $q = 4$, the values of critical exponents are less accurate than those for the Ising model ($q = 2$).

The best reliable results obtained from the DMRG and FSS procedure are listed as $y_{\rm T}$ and $y_{\rm H}$ in Table VII. Another possibility to estimate the critical exponents is to calculate $y_{\rm T}$ and $y_{\rm H}$ for a set of strip widths $L < L^{(\rm opt)}$ and extrapolate them to $L \to \infty$. These results, denoted as $y_{\rm T}^{\rm BST}$ and $y_{\rm H}^{\rm BST}$, (see Table VII) were obtained by BST extrapolation algorithm [102].

In case of the $q = 4$ Potts model, the scaling laws involve logarithmic corrections [98–

Table VII. The thermal and magnetic critical exponents $y_{\rm T}$ and $y_{\rm H}$, respectively for the q-state Potts model obtained via DMRG method with the PBC for $q = 2, 3$, and 4. The symbol † denotes conjectured critical exponents. The values $y_{\rm T}^{\rm (BST)}$ and $y_{\rm H}^{\rm (BST)}$ were obtained by BST extrapolation algorithm for $y_{\rm T}(L)$ and $y_{\rm H}(L)$, $L < L^{\rm opt}$, ε is the truncation error. (Values of multi-spin variables m for the $q = 3$ and 4 Potts models were taken as the maximum values permitted by our computational technique. It is, however, possible to take $m > 200$ for the $q = 4$ Potts model in order to obtain more accurate results.)

q	m	ε	$y_{\rm T}$	$y_{\rm T}^{\rm (exact)}$	$y_{\rm T}^{\rm (BST)}$	$y_{\rm H}$	$y_{\rm H}^{\rm (exact)}$	$y_{\rm H}^{\rm (BST)}$
2	60	10^{-12}	1.000002	1.0	—	1.8757	1.875	1.875003
3	121	10^{-10}	1.1948	$1.2^{\dagger}$	1.2004	1.8684	$1.86666^{\dagger}$	1.86667
4	63	10^{-7}	1.4337	$1.5^{\dagger}$	1.5008	1.8797	$1.875^{\dagger}$	1.8746

100]:

$$y_{\rm T} = \frac{3}{2} - \frac{3}{4}\frac{1}{\log L} + O[(\log L)^{-2}], \qquad y_{\rm H} = \frac{15}{8} - \frac{1}{16}\frac{1}{\log L} + O[(\log L)^{-2}]. \tag{154}$$

To take them into account, we extrapolated $y_{\rm T} + \frac{3}{4}(\log L)^{-1}$ and $y_{\rm H} + \frac{1}{16}(\log L)^{-1}$ instead of usually employed $y_{\rm T}$ and $y_{\rm H}$. In Table VII the calculated results are compared with the exact and conjectured ones [106].

The DMRG method for classical spin lattice strips with periodic boundaries was developed and applied to 2D Ising and Potts models. It was shown that this approach leads to more accurate results for 2D infinite lattice than DMRG with open boundary conditions. It was demonstrated that applying finite size scaling to strips treated by DMRG, an optimal width of the strip depending on the order of approximation existed, and a prescription how to find $T_{\rm C}^{*}(L^{\rm opt})$ was given. For the Ising model it was shown by computations that the value of the critical temperature was for a given m closest to the exact one for these $L^{\rm opt}(m)$. As our approach does not involve any information about the exact critical temperature $T_{\rm C}^{\rm (exact)}$ and the universality class of the model, we believe that it is applicable to many different classes of spin lattice models. This belief is supported by analogous calculation for the Anisotropic Triangular Nearest-Neighbor Ising model (ATNNI), see Section 5.3, with two different antiferromagnetic interactions J_1 and J_2 (the model was discussed in Section 5.1). The transfer matrix is non-symmetric for this model and the phase diagram is quite different from that of the standard Ising model. For the periodic boundary conditions, the plot of critical temperatures is not monotonously decreasing as it was in the case of the Ising model (Fig. 28) but it turns up for large L. Nevertheless, the accuracy of the critical temperature for the exactly solvable case (for external magnetic field $H = 0$) reaches high precision, too.

5.3 C-D phase transition in ATNNI model

Analysis of semi-finite systems of small size in one or more directions has been used as a powerful tool in extracting of critical properties of two-dimensional classical models and corresponding one-dimensional quantum models. Although finite or 1D systems

themselves do not display any critical behavior, it is, however, possible to extract critical parameter values as well as critical exponents. Temperature, ordering magnetic field, and finite-size deviations from criticality are all described by the same set of the critical exponents [95]. These calculations are focused on infinite strips of finite width where the relevant numerical data are obtained from the transfer matrix methods, in particular, the Density Matrix Renormalization Group (DMRG) method.

In Section 5.2, we have proposed a modification of the DMRG method for the 2D classical models, imposing periodic boundary conditions (PBC) on strip boundaries, and found a relation that helped to determine an optimal strip width $L^{\rm opt}$ in order to obtain correct values of critical temperature and exponents, Eq. (153), using the finite-size scaling (FSS). We have obtained results of very high accuracy exceeding that of the DMRG method with standard open boundary conditions. Our method does not require any extrapolation analysis of the data.

The use of DMRG for 2D classical models may follow one of two different approaches:

(i) DMRG method is applied to strips of finite width and from the two largest transfer-matrix eigenvalues or the free energy estimated with high precision, the critical properties of the system are calculated by the FSS analysis (this is the approach we use here).

(ii) The strip width is enlarged until a steady state is reached (in the thermodynamic limit) when the output from the DMRG does not depend on the lattice size. Then, the DMRG yields properties of the 2D infinite system with spontaneously broken symmetry and mean-field-like behavior close to the criticality. This approach was used recently to study the high-field part of the ATNNI-model phase diagram (in Section 5.1, Fig. 20), where approach *(i)* ran into convergence problems. We were able to show that the phase transition between the commensurate phase and the disordered phase proceeds via a narrow strip of an incommensurate phase. This approach gives also accurately the low-field part of the phase diagram, but it is not convenient for determination of the critical properties of the system by FSS. In distinction to the finite-width approach *(i)*, the system described here within this approach explicitly undergoes the phase transition, but its critical behavior is a mean-field-like and the speed of calculation suffers from critical slowing-down at the phase transition line. Therefore, we use here approach *(i)* to find the low-field critical behavior of the ATNNI model.

The FSS approach should give the correct critical properties of the system in the limit of infinite strip width. Nevertheless, it was shown (in Section 5.2) that in approximate DMRG treatment for a given size of the transfer matrix (limited by computer capacity), an enlargement of the strip width to large sizes is not useful because the DMRG results do not satisfy the scaling laws assumed by the FSS. Thus, an optimal width, up to which the results systematically improve, must exist. It was also shown that the estimation of critical properties of the Ising and Potts models by DMRG with the periodic boundary conditions are much better than those with the open ones, despite the latter yields better results for the finite-width strips, see Section 5.2.3.

5.3.1 Posing a problem

Below the optimal strip width $L^{\rm opt}$ the ratio

$$R \equiv \frac{\frac{\partial}{\partial L} T_{\rm C}^*(L)}{\frac{\partial^2}{\partial L^2} T_{\rm C}^*(L)} \tag{155}$$

is almost linear function of L while above it, it is not. (L in Eq. (155) is the width of the strip and $T_{\rm C}^*(L)$ is the critical temperature for given L.)

The deviation of R from linearity above the optimal strip width is very fast and the ratio R becomes zero or infinity within enlargement of the strip by one lattice constant. Thus, if $R = 0$ or $R \to \infty$ (i.e. if the numerator or the denominator tends to zero or changes its sign), we accept that L as the strip width for further calculations and call it the optimal width $L^{\rm opt}$ of the strip. The critical temperature for the optimal width $T_{\rm C}^*(L^{\rm opt})$ is taken as the best approximation of the critical temperature of the 2D system studied, and at this temperature the critical exponents of the system are calculated. The values of the critical exponents are sensitive to $T_{\rm C}^*$ and must be determined with a due care.

In the FSS approach, the critical exponents are derived from the scaling behavior of the correlation length and free energy at critical point, where they depend on strip width L in the following way [95]:

$$\kappa_L^{\rm h} \sim L^{2y_{\rm h}^{(\beta)}} \qquad \kappa_L^{\rm T} \sim L^{y_{\rm T}^{(\nu)}} \qquad c_{\rm L} \sim L^{2y_{\rm T}^{(\alpha)}-d} \tag{156}$$

where $\kappa_L^{\rm T}$ and $\kappa_L^{\rm h}$ are the derivatives of inverse correlation length κ with respect to temperature T and second derivative with respect to ordering (magnetic) field h, respectively, and $c_{\rm L}$ is the specific heat, i.e. the second derivative of the free energy with respect to temperature. The two temperature exponents $y_{\rm T}^{(\alpha)}$ and $y_{\rm T}^{(\nu)}$ should be equal to each other. The exponents $y_{\rm T}$ and $y_{\rm h}$ determine the critical behavior of all statistical quantities characterizing the system. The critical exponents of specific heat, magnetization and correlation length can be calculated from $y_{\rm T}$ and $y_{\rm h}$ as follows: $\alpha = 2 - \frac{2}{y_{\rm T}}$, $\beta = \frac{2-y_{\rm h}}{y_{\rm T}}$, $\nu = y_{\rm T}^{-1}$. Other critical exponents can be obtained from the scaling equations [107] or from Eqs. (117)-(122).

Further, we demonstrate the capabilities of our approach to find the critical properties of 2D spin lattice model on Ising model with different symmetries of the lattice, where critical temperatures and critical indices are known from exact solutions, and ATNNI model where the phase diagram is generally unknown and the critical indices are predicted from symmetry considerations.

The ATNNI model was studied by Domany and Schaub [80] and in [100], and it was shown that its phase diagram, as a plot of temperature T and external magnetic field H (for $a = 0.4$), exhibits four different phases: two commensurate phases $\langle I \rangle$ and $\langle II \rangle$, a disordered phase, and an incommensurate phase, see Fig. 20. Commensurate phase $\langle I \rangle$ occurs at magnetic field $H < 2.4$. This structure satisfies the Lifshitz condition, and it is characterized by a one-dimensional representation of the lattice symmetry group, i.e. its phase transition is predicted to belong to the Ising universality class [108, 109]. Domany and Schaub tried to confirm this prediction by numerical calculation of the exponent $y_{\rm T}$,

but due to the low-order approximation it differed from the expected value by more than 10% and the magnetic exponent was not calculated at all.

We have calculated critical properties of the ATNNI model at the phase transition line between the commensurate $\langle I \rangle$ and disordered (C-D) phase. To illustrate the accuracy of the method, we have calculated critical properties of the exactly solvable models: the ferromagnetic and the antiferromagnetic Ising models on both square and triangular lattices at zero magnetic field. The zero-magnetic-field ATNNI model is also exactly solvable and the critical temperature is given by the equation [1]

$$\sinh^2\left(\frac{2J}{T_{\mathrm{C}}}\right) = \exp\left(-\frac{4aJ}{T_{\mathrm{C}}}\right). \tag{157}$$

We have used the FSS analysis of DMRG results with superblock consisting of 8 Ising spins and 4 multi-spin variable, each acquiring $m = 85$, see Section 5.2. The computational effort at this approximation is less than for the classical transfer matrix method of strip width equal to 17 lattice constants. However, the DMRG enables to treat wider strip (of tens of lattice constants) up to the optimal width further improving the values of the critical parameters.

5.3.2 Calculation of the critical points and exponents

The first, important step of the calculations is determination of the critical temperature T_{C}^*, see Table VIII. The best estimate for given m is $T_{\mathrm{C}}^*(L^{\mathrm{opt}})$ and it is calculated from FSS approach, see Section 5.2.3. At this temperature the values of critical exponents are derived from the scaling laws (see Eq. (156)).

Table VIII. Critical temperatures T_{C}^* obtained from Eq. (155) with DMRG compared to the exact ones $T_{\mathrm{C}}^{(\mathrm{exact})}$. The symbols □ and △ describe square and triangular lattices, respectively.

model	H	T_{C}^*	$T_{\mathrm{C}}^{(\mathrm{exact})}$
□ Ising	0.0	2.2691851	2.2691853
□ AF Ising	0.0	2.2691848	2.2691853
△ Ising	0.0	3.640955	3.640957
△ ATNNI	0.0	1.55352	1.55362
△ ATNNI	0.5	1.52867	unknown
△ ATNNI	1.0	1.45135	unknown
△ ATNNI	1.5	1.31105	unknown
△ ATNNI	2.0	1.07009	unknown

As the quantities appearing in Eq. (156) are the first and the second derivatives of the free energy and of correlation length, the effect of approximation starts to manifest at lower strip width than L^{opt}. The criterion determining strip width at which the value of the critical exponent may be still acceptable, was taken completely analogous to that for critical temperature, Eq. (155). The accepted values of the critical exponents are denoted by filled symbols in Figs. 29 and 29.

The critical exponent y_{T} is determined more precisely from the free energy $y_{\mathrm{T}}^{(\alpha)}$ than from the correlation length $y_{\mathrm{T}}^{(\nu)}$, as for the evaluation of the former one only the largest

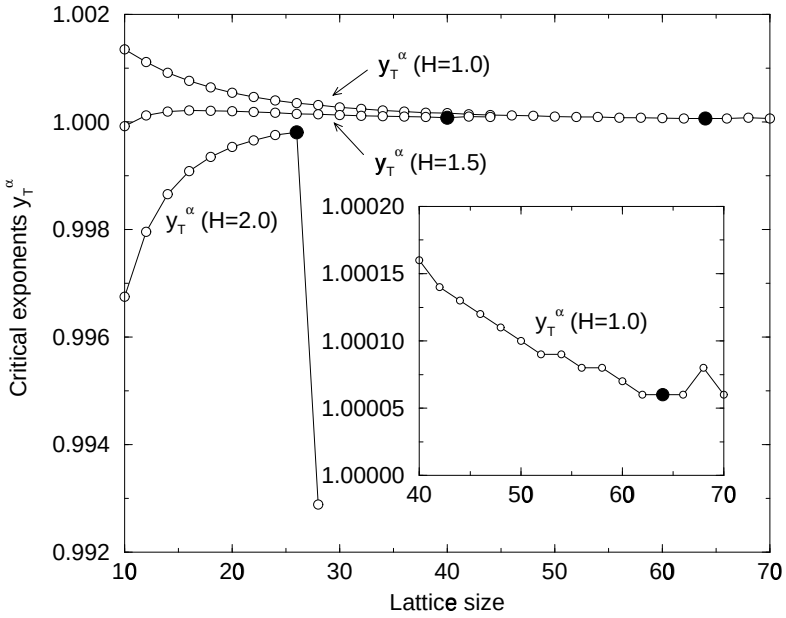

Fig. 29. The plot of thermal critical exponents $y_{\mathrm{T}}^{(\alpha)}$ for different magnetic fields H in the ATNNI model. The filled symbols denote the accepted critical exponents satisfying Eq. (155). The inset shows the detail of the critical exponent $y_{\mathrm{T}}^{(\alpha)}$ at H=1.0.

eigenvalue of the superblock matrix is needed in distinction to the correlation length, to calculation of which the ratio of the largest and the second largest eigenvalues is necessary. This point is irrelevant for the models with a symmetric transfer matrix (Ising models in Table VIII), but significant for the ATNNI model with a non-symmetric transfer matrix [84–88]. The plot of thermal critical exponent $y_{\mathrm{T}}^{(\alpha)}$ vs. strip width is shown in Fig. 29. For increasing lattice size they both tend to the Ising value 1. The convergence also depends on the magnetic field. It gets worse for magnetic field close to the multi-critical point $H = 2.4$. Here the reliability of the DMRG breaks down also at rather small strip width. The accepted values depicted by black symbols are listed in Table IX.

The critical exponent $y_{\mathrm{h}}^{(\beta)}$ describes the decay of the order parameter at the phase transition line from the commensurate phase $\langle I\rangle$ to the disordered phase. The structure $\langle I\rangle$ consists of two ferromagnetically ordered sublattices each with different magnetization. As the external magnetic field H is generally non-zero in ATNNI model, the total magnetization (sum of both sublattice magnetizations) is non-zero, as well. The difference between the two magnetization is taken as the order parameter in this case. The small ordering field h used for calculation of the derivative K_L^h acquires opposite sign at each of the two sublattices. The accuracy of the calculations of the magnetic exponent is smaller than that of the thermal exponent in case of exactly solvable models listed in Table IX. Thus, we can expect a lower accuracy also for ATNNI model. All the exponents depicted in Fig. 30 are below $y_{\mathrm{h}}^{(\beta)}$=1.871. Extrapolations to $L \to \infty$ for H=0.5

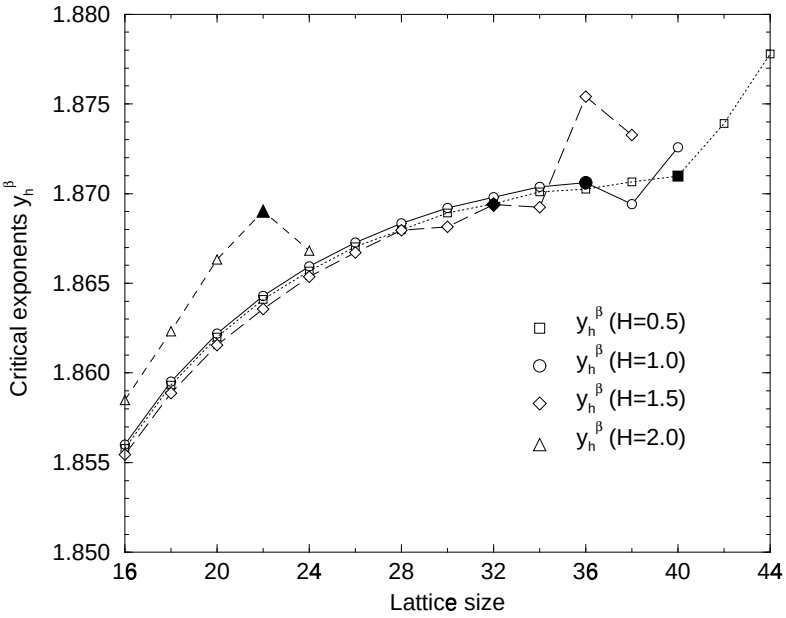

Fig. 30. The plot of magnetic critical exponents $y_{\rm h}^{(\beta)}$. The filled symbols denote the accepted critical exponents satisfying Eq. (155)

Table IX. Critical exponents of various 2D spin models calculated by the DMRG method with PBC and FSS analysis. The exact critical exponents of the Ising models are $y_{\rm T} = 1$ and $y_{\rm h} = 1.875$. Notation of the models is the same as in the preceding Table.

model	H	$y_{\rm T}^{(\alpha)}$	$y_{\rm T}^{(\nu)}$	$y_{\rm h}^{(\beta)}$	α	β^{-1}	ν
□ Ising	0.0	1.0000009	0.99999994	1.875002	0.0000017	8.00012	1.00000006
□ AF Ising	0.0	1.0000009	0.99999994	1.875126	0.0000017	8.00804	1.00000006
△ Ising	0.0	1.0000014	0.99999943	1.875030	0.0000027	8.00192	1.00000057
△ ATNNI	0.0	1.0000022	0.9947	1.87005	0.000004	7.70	1.00527
△ ATNNI	0.5	1.0000280	0.9902	1.87098	0.000056	7.75	1.00993
△ ATNNI	1.0	1.0000580	0.9902	1.87062	0.000116	7.73	1.00993
△ ATNNI	1.5	1.0000767	0.9911	1.86939	0.000153	7.66	1.00893
△ ATNNI	2.0	0.9998366	1.0122	1.86902	0.000327	7.63	0.98795

to 1.5 give values of $y_{\rm h}^{(\beta)}$ about 1.872, i.e. $1/\beta$=7.81, which still differs from the Ising value $y_{\rm h}^{(\beta)} = 1.875$ and corresponding $1/\beta$=8. Note that the value of $y_{\rm h}^{(\beta)}$ is extremely sensitive to the correct determination of the critical temperature. A very small decrease of its value would shift $y_{\rm h}^{(\beta)}$ to the expected Ising value. At modest magnetic field, where our calculations are assumed to be more accurate, the plots of $y_{\rm h}^{(\beta)}$ for different magnetic field lie on the same curve what suggests that not only $y_{\rm h}^{(\beta)}$ is a universal quantity independent of H, but the corrections to it for finite L are universal.

In conclusion, it can be stated that the DMRG method with periodic boundary

conditions reproduces with a high accuracy the critical properties of exactly solvable models and confirms the prediction that the C-D phase transition for magnetic fields H=0 to 2.4 belongs to the universality class of the Ising model.

5.4 3D q=3 and q=4 state Potts models

Throughout this Section we will follow considerations described in Sec. 3.3 for three-dimensional classical models. The self-consistent tensor product variational approach (TPVA) has been developed by Nishino et al. [36] as a numerical variational method for three-dimensional classical lattice models. The variational state is constructed as a product of local tensors and of the corner transfer matrix renormalization group (CTMRG) method was used to improve the variational state. In particular, the CTMRG method is applied twice within the TPVA. Once, when we look for the variational state of 2D plane and twice when we apply CTMRG to a layer-to-layer transfer matrix. These two procedures are tied up by the self-consistent equation (94).

Okunishi and Nishino used the Kramers-Wannier approximation for the three-dimensional Ising model using CTMRG and they obtained the critical point $K_{\rm c} = 0.2184$ [77]. The next tests carried out by Nishino et al. [36] using TPVA yielded the critical point $K_{\rm c} = 0.2188$ of the Ising model of the IRF type which is by about 1.3% less than the Monte Carlo result $K_{\rm c}^{\rm MC} = 0.2216544$ [73, 74].

Further improvements of TPVA continued by additional considerations in Ref. [37]. The authors assumed 3D Ising model of the vertex type and, moreover, the variational 2D state V was constructed from a product of tensors which carried additional degrees of freedom to the model and thus improved the variational state by the self-consitent algorithm. The obtained critical point $K_{\rm c} = 0.2203$ was only about 0.61% less than that of Monte Carlo simulations.

5.4.1 Thermodynamic functions

The free energy F per site is closely related to the largest eigenvalue of the 3D layer-to-layer transfer matrix $\mathcal{T}$. In the thermodynamic limit, it reads

$$\begin{aligned} F(T,H) &= -k_B T \lim_{N\to\infty} \ln\left(\lambda_{\rm max}\right)^{\frac{1}{N}} \\ &= -k_B T \lim_{N\to\infty} \ln\left(\frac{\langle V_N|\mathcal{T}_N|V_N\rangle}{\langle V_N|V_N\rangle}\right)^{\frac{1}{N}}, \end{aligned} \tag{158}$$

where the number of CTMRG iterations as well as the dimension of the system are both described by the term N. The free energy F is normalized in each iteration in order to observe its convergence at finite N. The converged state (fixed point) is equivalent to the thermodynamic limit ($N\to\infty$) because of the fixed precision of numerical calculations.

Let us define the free energy $F_{\rm N}$ of an $N\times N$ square system

$$F_{\rm N} = -k_B T \left[f_2 N^2 + f_1 N + f_0 + \mathcal{O}(N^{-1})\right], \tag{159}$$

where we have taken into account the surface energy and higher corrections. By use of new notations for the corner transfer matrices C_N and D_N that correspond to the

numerator $\langle V_N|\mathcal{T}_N|V_N\rangle$ and denominator $\langle V_N|V_N\rangle$ of the Reyleigh ratio (Eq. (81)), respectively [33, 77], we can derive an accelerated formula for the calculation of the free energy F per site. Inserting Eq. (159) into the numerator,

$$\langle V_N|\mathcal{T}_N|V_N\rangle = \mathrm{Tr}\left\{D^4_{N/2}\right\} = \exp\left\{B_2N^2 + B_1N + B_0 + \mathcal{O}(N^{-1})\right\}, \tag{160}$$

and the denominator,

$$\langle V_N|V_N\rangle = \mathrm{Tr}\left\{C^4_{N/2}\right\} = \exp\left\{A_2N^2 + A_1N + A_0 + \mathcal{O}(N^{-1})\right\}, \tag{161}$$

of the Reyleigh ratio, let us use

$$\frac{\langle V_{N-1}|\mathcal{T}_{(N-1)}|V_{N-1}\rangle\langle V_{N+1}|\mathcal{T}_{(N+1)}|V_{N+1}\rangle}{\langle V_N|\mathcal{T}_N|V_N\rangle\langle V_N|\mathcal{T}_N|V_N\rangle} = \exp\{8B_2\} \equiv \mathcal{B}_N \tag{162}$$

and

$$\frac{\langle V_{N-1}|V_{N-1}\rangle\langle V_{N+1}|V_{N+1}\rangle}{\langle V_N|V_N\rangle\langle V_N|V_N\rangle} = \exp\{8A_2\} \equiv \mathcal{A}_N, \tag{163}$$

as they do not depend on the lattice size N up to the higher-term corrections $\mathcal{O}(N^{-1})$. Hence, the accelerated formula for the numerical calculation of the free energy $F(T,H)$ per site is then given by

$$F(T,H) = -\frac{1}{8}k_BT\lim_{N\to\infty}\ln\left(\frac{\mathcal{B}_N}{\mathcal{A}_N}\right). \tag{164}$$

We have applied the TPVA algorithm for the more precise determination of the q=3 and q=4 state Potts models, and in particular, we kept the parameter $m = 20$ in TPVA for both the models. The internal energy per site is defined as

$$E^{\mathrm{int}} = -\frac{\partial\ln\mathcal{Z}}{\partial\beta} = -T^2\frac{\partial}{\partial T}\left(\frac{F}{T}\right), \tag{165}$$

$\mathcal{Z}$ and F are the partition function and the free energy, respectively. In the TPVA language the internal energy per site can be expressed as

$$E^{\mathrm{int}} = -\langle\delta_{\sigma_{i,j}\sigma_{i',j}}\rangle - \langle\delta_{\sigma_{i,j}\sigma_{i,j'}}\rangle - \langle\delta_{\sigma_{i,j}\bar{\sigma}_{i,j}}\rangle, \tag{166}$$

which is in agreement with Eq. (165) and the notation corresponds to that shown in Fig. 9.

5.4.2 Results

The self-consistent equation (94) must be slightly modified, otherwise the algorithm becomes rather unstable. Therefore, the calculation of W proceeds in several steps and

the small parameter ε is introduced in order to improve W in smaller smooth steps. [21]

$$(1) \quad W_1 = \frac{B}{A} W_{\rm old}, \tag{167}$$

$$(2) \quad \text{normalize} \quad W_1, \tag{168}$$

$$(3) \quad W_{\rm new} = W_{\rm old} + \varepsilon W_1, \tag{169}$$

$$(4) \quad \text{normalize} \quad W_{\rm new}. \tag{170}$$

In our calculations we set $\varepsilon = 0.1$ (any smaller value of ε may be used without significant influence to these results).

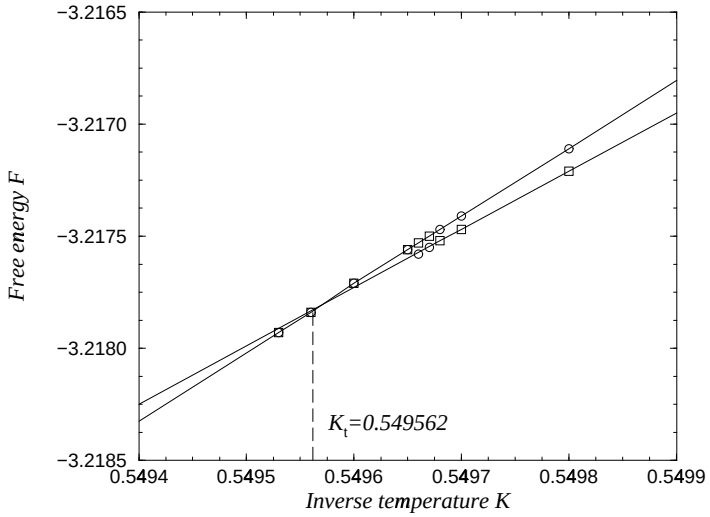

Fig. 31. The crossover of the free energy as the function of the inverse temperature K for the three-dimensional $q = 3$ state Potts model.

As CTMRG and consequently TPVA are sensitive to the choice of boundary conditions, it is necessary to perform calculations both for the open boundary conditions (OBC) and fixed boundary conditions (FBC), i. e., we calculate the free energy per site. We determine the transition point $K_{\rm t}$ as the point where the curves of free energies (as functions of inverse temperature K) for the OBC and FBC intersect each other because the free energy curve must remain continuous. For the q=3 state Potts model, the free energy crossover is depicted in Fig. 31.

The plot of the internal energy $E^{\rm int}$ is depicted in inset of Fig. 32 if the fixed and free boundary conditions are imposed. The calculated transition point $K_{\rm t} = 0.549562$ is almost the same as that for $m \leq 15$ in Ref. [36] We have measured the latent heat [110] which is proportional to the internal energy gap as

$$l = (E_+^{\rm int} - E_-^{\rm int}). \tag{171}$$

[21] The original $W_{\rm old}$ is changed to $W_{\rm new}$ according to Eqs. (167 to 170) and then the $W_{\rm new}$ is replaced back to $W_{\rm old}$.

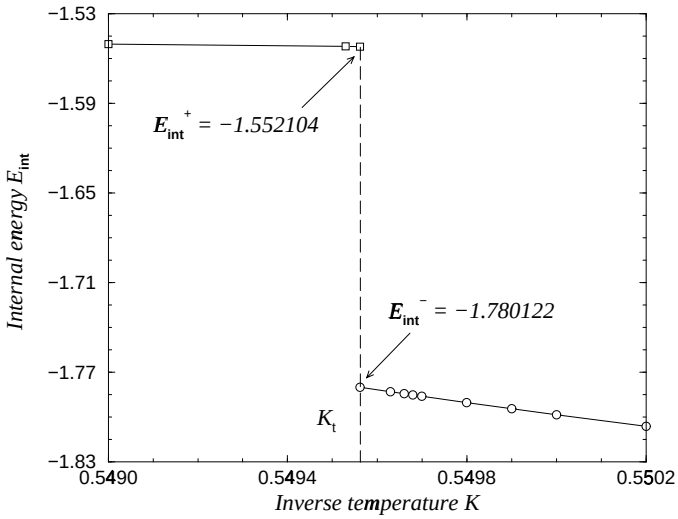

Fig. 32. The internal energy per unit cell as the function of the inverse temperature K for the 3D q=3 state Potts model. The internal energy per unit cell equals one third of the internal energy per site defined in Eq. (166).

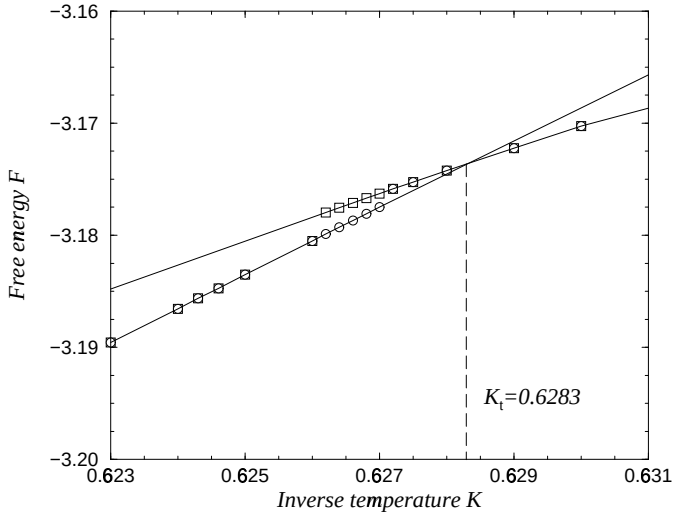

Fig. 33. The crossover of the free energy as the function of the inverse temperature K for the three-dimensional $q = 3$ state Potts model. The transition point $K_t = 0.6283$.

Our calculation of the internal energy $E_{\rm int}$ jump yields $l = 0.2280$ which is 41% larger than the result from Monte Carlo simulations $l_{\rm MC} = 0.1616$ [110].

The result of the numerical calculations of the transition point K_t for the q=4 state Potts model (for $m = 20$) is shown in Fig. 33.

We have found that the fixed boundary conditions stabilize the ordered phase of the model while the open boundary conditions stabilize the disordered phase. At the close vicinity of the transition points, the free energies differed for the OBC and FBC. The transition point K_t is defined as the free energy crossover in the sense of the Landau theory. Therefore, it was necessary to extrapolate the free energy data for both OBC and FBC. The correct latent heat l has been obtained from internal energies $E^{\rm int}$ extrapolated to the calculated transition point K_t. The calculation of latent heat for the case q=4 is in progress. The three-dimensional q=3 state Potts model exhibits a weak first-order phase transition which can be seen in Fig. 31 as a smooth crossing of the free energy curves. On the other hand the 3D q=4 state Potts model displays the regular first-order phase transition and therefore we expect to obtain the latent heat l much more larger than that for the case of q=3. Studying these models in detail, we found that the TPVA algorithm was stable when the parameter $\varepsilon \leq 0.1$ was introduced.

6 Summary and discussion

Numerical studies of classical lattice models play an important role, especially, in the cases when the models are not exactly solvable. In this review article, it has been shown that numerical renormalization group approaches, in particular, DMRG and its modifications, were suitable candidates to treat various 2D and 3D classical lattice models. The DMRG has become a powerful tool exceeding the classical Monte Carlo simulations in speed and size of the systems that can treat [111]. DMRG also yields more accurate results for one-dimensional quantum models than Monte Carlo. Moreover, DMRG is free of sign problems appearing in quantum Monte Carlo simulations for fermionic systems and can also be employed to study incommensurate modulated structures because Monte Carlo suffers from large fluctuations which come from the frustration. DMRG calculations yield the critical points of any studied models faster than those of the Monte Carlo simulation if compared with computational CPU times.

Within the infinite system method (ISM), the DMRG method displays the mean-field-like behavior. The ISM has been applied to study the incommensurate floating spin structures in the ATNNI and ANNNI models and we were able to detect the complete phase diagrams where the other methods [80, 99] failed.

The finite system method (FSM) improves approximated ground state properties of large transfer matrices with higher accuracy, however, the larger lattice size is taken the lower accuracy can be reached. Such approximated transfer matrices can enter the finite-size scaling (FSS) approach to obtain information on critical points as well as all critical exponents. However, FSS yields better results for larger matrices. Therefore, there must exist an optimum transfer matrix (strip) size $L^{\rm opt}$ at which the connection of the DMRG and FSS gives the best results. We have shown how to obtain $L^{\rm opt}$. We have also been the first ones who proposed the DMRG algorithm with periodic boundary conditions for the two-dimensional classical models. Combining the theory of finding out the optimal strip size $L^{\rm opt}$, DMRG with the periodic boundary conditions, and FSS analysis together we were able to solve several models with very high precision. In particular, we applied the approach to the two-dimensional ferromagnetic and antiferromagnetic Ising model on the square and triangular lattices as well as to the 2D q-state Potts model for q=2,

3 and 4. We detected the critical temperatures T_c as well as all corresponding critical exponents. We have applied this new technique to the more complicated ATNNI model and investigated the commensurate-disordered (C-D) phase transition in detail. We had to include additional considerations how to treat nonsymmetric transfer matrices as well as how to extract magnetic critical exponent from two sublattices of the ATNNI model exhibiting different spin magnetizations within the commensurate phase. Thus we obtained full information on the C-D phase transition line. Since the ATNNI model is not exactly solvable, we calculated several critical points (T_c, H_c) on the transition line at which we determined all critical exponents. We concluded that the C-D phase transition belonged to the Ising universality class and thus confirmed the prediction published in [108, 109].

Three-dimensional classical models have been studied using recently developed TPVA algorithm. [36, 37] We calculated the three-dimensional classical q-state Potts model for q=3 and q=4 and observed properties of the free energy and the internal energy in the close vicinity of the transition point K_t in these models. The latent heats have been obtained because they reflect the discontinuity in the internal energy at the transition point K_t. The predictions that these models exhibit the first-order phase transitions was confirmed.

There are many models not yet solved neither analytically nor numerically. The techniques discussed in this review are now open for further applications to various kinds of two- and three-dimensional models. Since TPVA was applied only to symmetric models like 3D Ising and q-state Potts models are, nowadays the main interests are focused on generalizaton of TPVA for nonsymmetric problems. For example, the three-dimensional frustrated Ising defined on the other than cubic lattice has not been studied yet. It requires to consider ferromagnetic nearest-neighbor interactions and antiferromagnetic next-nearest-neighbor interactions. This model exhibits a complex phase diagram including commensurate, long-range commensurate, incommensurate, and disordered phases.

Another problem which has not been solved yet concerns with infinite two-dimensional quantum lattice models. For example, the two-dimensional quantum Heisenberg model on the triangular lattice with non-hermitian Hamiltonian, still remains as the unsolved problem. The solution could be hidden in TPVA using the Suzuki-Trotter mapping. To propose a brand-new and efficient algorithm based on DMRG ideas for higher dimensions, it is still the challenging problem.

Acknowledgments I am very grateful to A. Šurda for his supervisor's guiding my Ph.D. studies and especially to T. Nishino for his permanent help and teaching as well as for having an opportunity to collaborate. This way I also thank to the Kansai group, experts on DMRG. I would like to express my thanks to P. Markoš and L. Šamaj for valuable discussions. This work has been supported by Slovak Grant Agency, Grant No. 2/7174/20.

References

[1] R. J. Baxter: *Exactly Solved Models in Statistical Mechanics*, Academic Press, London 1982

[2] H. A. Kramers, G. H. Wannier: *Phys. Rev.* **60** (1941) 262

[3] R. J. Baxter: *J. Math. Phys.* **9** (1968) 650
[4] R. J. Baxter: *J. Stat. Phys.* **19** (1978) 461
[5] R. J. Baxter, I. G. Enting: *J. Stat. Phys.* **21** (1979) 103
[6] R. J. Baxter, I. G. Enting, S. K. Tsang: *J. Stat. Phys.* **22** (1980) 465
[7] L. P. Kadanoff: *Physics* **2** (1965) 263
[8] K. G. Wilson: *Rev. Mod. Phys.* **47** (1975) 773
[9] K. G. Wilson, J. Kogut: *Phys. Rep. C* **12** (1974) 75
[10] *Density Matrix Renormalization – A New Numerical Method in Physics, Lecture notes in Physics* (Eds. I. Peschel, X. Wang, M. Kaulke, K. Hallberg). Springer Verlag Vol. **528** 1999
[11] S. R. White: *Phys. Rev. Lett.* **69** (1992) 2863
[12] S. R. White: *Phys. Rev. B* **48** (1993) 10345
[13] S. R. White, D. A. Huse: *Phys. Rev. B* **48** (1993) 3844
[14] E. S. Sørensen, I. Affleck: *Phys. Rev. Lett.* **71** (1993) 1633
[15] E. S. Sørensen, I. Affleck: *Phys. Rev. B* **49** (1994) 15771
[16] E. Jeckelmann, D. J. Scalapino, S. R. White: *Phys. Rev. B* **58** (1998) 9492
[17] N. Shibata, A. Tsvelik, K. Ueda: *Phys. Rev. B* **56** (1997) 330
[18] D. J. Scalapino, S. R. White: *Phys. Rev. B* **58** (1998) 8222
[19] C. C. Yu, S. R. White: *Phys. Rev. Lett.* **71** (1993) 3866
[20] R. M. Noack, S. R. White, D. J. Scalapino: *Phys. Rev. Lett.* **73** (1994) 882
[21] N. Shibata, T. Nishino, K. Ueda, C. Ishii: *Phys. Rev. B* **53** (1996) 8828 .
[22] I. Peschel, M. C. Chung: (cond-mat/9906224)
[23] M. C. Chung, I. Peschel: (cond-mat/0004222)
[24] X. Wang, T. Xiang: *Phys. Rev. B* **56** (1997) 2221
[25] K. Hida: *J. Phys. Soc. Jpn.* **65** (1996) 895
[26] K. Hida: *J. Phys. Soc. Jpn.* **66** (1997) 330
[27] H. Otsuka: *Phys. Rev.* **53** (1996) 14004
[28] T. Xiang: *Phys. Rev.* **53** (1996) R10445
[29] R. P. Feynmann, A. R. Hibbs: *Quantum mechanics and Path Integrals*, McGraw-Hill 1965
[30] H. F. Trotter: *Proc. Am. Math. Soc.* **10** (1959) 545
[31] M. Suzuki: *Prog. Theor. Phys.* **56** (1976) 1454
[32] T. Nishino: *J. Phys. Soc. Jpn.* **64** (1995) 3599
[33] T. Nishino, K. Okunishi, M. Kikuchi: *Phys. Lett. A* **213** (1996) 69
[34] T. Nishino, K. Okunishi: *J. Phys. Soc. Jpn.* **65** (1996) 891
[35] T. Nishino, K. Okunishi: *J. Phys. Soc. Jpn.* **66** (1997) 3040
[36] T. Nishino, K. Okunishi, Y. Hieida, N. Maeshima, Y. Akutsu: *Nucl. Phys. B* **575** (2000) 504
[37] T. Nishino, K. Okunishi, Y. Hieida, N. Maeshima, Y. Akutsu, A. Gendiar: *Prog. Theor. Phys.* **105** (2001) (in press)
[38] E. Ising: *Z. Phyzik* **31** (1925) 253
[39] W. L. Bragg, E. J. Williams: *Proc. Roy. Soc. A* **145** (1934) 699
[40] H. A. Bethe: *Proc. Roy. Soc. A* **150** (1935) 552

[41] E. A. Guggenheim: *Proc. Roy. Soc. A* **145** (1935) 304
[42] R. Kikuchi: *Phys. Rev.* **81** (1951) 988
[43] J. M. J. van Leeuwen, J. Groeneveld, J. Boer: *Physica* **25** (1959) 792
[44] J. K. Percus: *Phys. Rev. Lett.* **8** (1962) 462
[45] J. K. Percus, G. J. Yevick: *Phys. Rev.* **110** (1958) 1
[46] M. F. Sykes, J. W. Essam, D. S. Gaunt: *J. Math. Phys.* **6** (1965) 283
[47] M. F. Sykes, D. S. Gaunt, J. W. Essam, C. J. Elliott: *J. Phys. A: Math., Nucl. Gen.* **6** (1973) 1507
[48] K. G. Wilson: *Phys. Rev. B* **4** (1971) 3174
[49] M. E. Fisher: *Rev. Mod. Phys.* **46** (1974) 597
[50] K. G. Wilson, J. Kogut: *Phys. Reports C* **12** (1974) 75
[51] I. Karasová, A. Šurda: *J. Stat. Phys.* **70** (1993) 675
[52] A. Gendiar, T. Nishino: *submitted to Phys. Rev. B* (cond-mat/0102425)
[53] M. A. Martín-Delgado, J. Rodriguez-Laguna, G. Sierra: (cond-mat/0009474)
[54] N. Maeshima, Y. Hieida, Y. Akutsu, T. Nishino, K. Okunishi: (cond-mat/0101360)
[55] H. Takasaki, T. Nishino, Y. Hieida: (cond-mat/0012490)
[56] H. E. Stanley: In*Phase transition and critical phenomena* (Eds. C.Domb, M. S. Green). Vol. 3, Academic Press, London 1974, pp. 485-567
[57] J. Kanamori: *Prog. Theor. Phys.* **20** (1958) 890
[58] D. E. Wrege, S. Spooner, H. A. Gersch: *American Institute of Physics Conference Proceedings* **5** (1972) 1334
[59] S. K. Ma: *Modern theory of critical phenomena* W. A. Benjamin, Reading 1976
[60] L. D. Landau, E. M. Lifshitz: *Statistical physics* Vol. 5, Nauka, Moscow 1964
[61] S. Aubry: *Ferroelec.* **24** (1980) 53
[62] P. Bak, V. L. Pokrovsky: *Phys. Rev. Lett.* **47** (1981) 958
[63] P. Bak: *Rep. Prog. Phys.* **45** (1982) 587
[64] F. Wegner: *Z. Phys.* **206** (1979) 465
[65] B. Jancovici: *Phys. Rev. Lett.* **19** (1967) 20
[66] V. L. Pokrovsky, A. L. Talapov: *Zh. Eksp. Teor. Fiz.* **78** (1980) 269
[67] M. Jaubert, A. Glachant, M. Bienfait, G. Boato: *Phys. Rev. Lett.* **46** (1981) 1676
[68] F. C. Frank, J. H. Van der Merwe: *Proc. R. Soc.* **198** (1949) 205, 216
[69] A. Gendiar, A. Šurda: *Phys. Rev. B* **64** (2001) 014401
[70] A. Gendiar, A. Šurda: *J. Phys. A: Math. Gen.* **33** (2000) 8365
[71] S. Liang, H. Pang: *Phys. Rev. B* **49** (1994) 9214
[72] T. Nishino, K. Okunishi: *J. Phys. Soc. Jpn.* **68** (1999) 3066
[73] A. M. Ferrenberg, D. P. Landau: *Phys. Rev. B* **44** (1991) 5081
[74] A. L. Talapov, H. W. J. Blöte: *J. Phys. A, Math. Gen.* **29** (1996) 5727
[75] S. Östlund, S. Rommer: *Phys. Rev. Lett.* **75** (1005) 3537
[76] S. Rommer, S. Östlund: *Phys. Rev. B* **55** (1997) 2164
[77] K. Okunishi, T. Nishino: *Prog. Theor. Phys.* **103** (2000) 541
[78] P. Pajerský, A. Šurda: *J. Phys. A: Math. Gen.* **30** (1997) 4187
[79] A. Šurda: *Acta Phys. Slov.* **49** (1999) 325

[80] E. Domany, B. Schaub: *Phys. Rev. B* **29** (1983) 4095
[81] J. Villain, P. Bak: *J. Phys.* **42** (1981) 657
[82] V. L. Pokrovsky, A. L. Talapov: *Phys. Rev. Lett.* **42** (1979) 65
[83] H. J. Schultz: *Phys. Rev. B* **22** (1980) 5274
[84] M. N. Barber, P. M. Duxbury: *J. Phys. A* **14** (1981) L251
[85] M. E. Fischer, W. Selke: *Phys. Rev. Lett.* **44** (1980) 1502
[86] F. D. M. Haldane, P. Bak, T. Bohr: *Phys. Rev. B* **28** (1983) 2743
[87] Y. Hieida: *J. Phys. Soc. Jpn.* **67** (1998) 369
[88] Y. Hieida, K. Okunishi, Y.Akutsu: *New J. Phys.* **1** (1999) 7.1
[89] T. Nishino, N. Shibata: *J. Phys. Soc. Jpn.* **68** (1999) 3501
[90] N. Shibata: *J. Phys. Soc. Jpn.* **66** (1997) 2221
[91] X. Wang, T. Xiang: *Phys. Rev. B* **56** (1997) 5061
[92] R. J. Burssil, T. Xiang, G. A. Gehring: *J. Phys. Cond. Mat.* **8** (1996) L583
[93] K. Maisinger, U. Schollwöck: *Phys. Rev. Lett.* **81** (1998) 445
[94] E. Carlon, M. Henkel, U. Schollwöck: *Eur. Phys. J. B* **12** (1999) 99
[95] P. Nightingale: *J. Appl. Phys.* **53** (1982) 7927
[96] W. Selke: *Phys. Rep.* **170** (1988) 213
[97] W. Selke: *in Phase Transition and Critical Phenomena*, vol. **15**, New York, Academic 1992
[98] M. den Nijs: *in Phase Transition and Critical Phenomena* (Eds. C. Domb, J. L. Lebowitz). Academic, London, 1988 Vol 12, pp. 220–333
[99] L. Tóth, A. Šurda: (unpublished)
[100] A. Gendiar, A. Šurda: *Phys. Rev. B* **62** (2000) 3960
[101] M. N. Barber: *Phase Transitions and Critical Phenomena* (Eds. C. Domb, J. L. Lebowitz). Academic Press, London, Vol. 8 1983, pp. 146–266
[102] M. Henkel, G. Schütz: *J. Phys. A* **21** (1988) 2617
[103] H. W. J. Blöte, A. Compagner, P. A. M. Cornelissen, A. Hoogland, F. Mallezie, C. Vanderzande: *Physica A* **139** (1986) 395
[104] C. Vanderzande, A. L. Stella: *J. Phys. A* **20** (1987) 3001
[105] E. Carlon, F. Iglói: (cond-mat/9710144)
[106] F. Y. Wu: *Rev. of Mod. Phys* **54** (1982) 235
[107] R. Balescu: *Equilibrium and Nonequilibrium Statistical Mechanics* Moscow, Mir 1978 (in Russian)
[108] E. Domany, M. Schick, J. S. Walker: *Phys. Rev. Lett.* **38** (1977) 1148
[109] E. Domany, M. Schick, J. S. Walker, R. B. Griffiths: *Phys. Rev. B* **18** (1983) 2209
[110] W. Janke, R. Villanova: *Nucl. Phys. B* **489** (1997) 679
[111] K. Hallberg: (cond-mat/9910082)